SYSTEM PARAMETERS AND PERFORMANCE SPECIFICATIONS FOR THE APPLICATION OF DIFFRACTION ENHANCED IMAGING AND MULTIPLE IMAGE RADIOGRAPHY TO BREAST IMAGING

Christopher Allen Parham

A dissertation submitted to the faculty of the University of North Carolina at Chapel Hill in partial fulfillment of the requirements for the degree of Doctor of Philosophy in the Department of Biomedical Engineering.

Chapel Hill
2006

Approved by
Advisor: Etta Pisano
Reader: David Lalush
Reader: Marija Ivanovic
Reader: Eugene Johnston
Reader: Leroy Dean Chapman

ABSTRACT

CHRISTOPHER ALLEN PARHAM: System Parameters And Performance Specifications For The Application Of Diffraction Enhanced Imaging And Multiple Image Radiography To Breast Imaging
(Under the direction of Etta D. Pisano, M.D.)

The Diffraction Enhanced Imaging (DEI) method is a novel x-ray imaging technique that dramatically extends the capability of conventional x-ray imaging. X-ray imaging has traditionally been dependent on x-ray absorption to generate contrast, and is the physical mechanism of contrast in planar x-ray imaging and computed tomography. DEI utilizes the Bragg peak of perfect crystal diffraction to convert angular changes into intensity changes, providing a large change in intensity for a small change in angle. The use of a silicon analyzer crystal in the path of the x-ray beam generates two additional forms of image contrast, refraction and extinction. Objects that have very little absorption contrast may have considerable refraction and extinction contrast, this improving visualization and extending the utility of x-ray imaging. An area of medicine where this technique could have a dramatic impact is in breast imaging, where the key diagnostic structures often have low absorption contrast, especially in the early stages of disease. In order to develop a DEI clinical prototype imaging system, a systematic assessment of the engineering parameters for the breast imaging application must be determined. This body of work investigates the primary imaging parameters of DEI (x-ray beam energy, crystal reflections, angular sampling) and demonstrates how the unique properties of DEI can be capitalized upon to address

the engineering limitations of flux, dramatically reducing the dose required for imaging. The results from this analysis are used to describe a plausible design for a non-synchrotron based DEI breast imaging system.

TABLE OF CONTENTS

LIST OF TABLES

LIST OF FIGURES

LIST OF ABBREVIATIONS

ALND	axillary lymph node dissection
BNL	Brookhaven National Laboratory
CNB	core needle biopsy
DEI	diffraction enhanced imaging
DEI-CT	diffraction enhanced imaging computed tomography
DNA	deoxyribonucleic acid
DW	Darwin width
FNA	fine needle aspiration
FWHM	full width at half maximum
MIR	multiple image radiography
MIR-CT	multiple image radiography computed tomography
MGD	mean glandular dose
NNT	number needed to treat
NSLS	National Synchrotron Light Source
PET	positron emission tomography
SPECT	single photon emission computed tomography

Chapter 1: Introduction

1.1 Overview

Diffraction Enhanced Imaging (DEI) is a novel x-ray imaging modality capable of generating image contrast from x-ray absorption, refraction, and ultra-small angle scatter (Chapman et al. 1997). Applications of this method to biology and materials science have generated impressive gains in both contrast and resolution, indicating the potential for use in mainstream medical imaging (Pisano et al. 2000; Chapman et al. 1998; Fiedler et al. 2004; Keryiläinen et al. 2005; Muehleman et al. 2004; Li et al. 2004). An area where DEI may be particularly effective is in breast imaging, where the diagnostic structures of interest often have low absorption contrast, making them difficult to see. Structures with low absorption contrast, such as the speculations extending from a malignant mass, have high refraction and ultra-small angle scatter contrast. The long term goal of the DEI research and development group is to design a DEI mammography system with the potential to increase the sensitivity and specificity of x-ray-based breast imaging. In order to accomplish this goal, the first step is to determine the synchrotron-based optimal performance characteristics for DEI breast imaging using.

While the optics of a DEI system are relatively simple, the energy filtering process that occurs requires a high intensity x-ray source for image acquisition. All DEI studies to date have been performed using synchrotron x-ray sources, but efforts are currently underway to translate this synchrotron based technology to a more clinically realistic system. Determining the imaging parameters for breast imaging, including such factors as x-ray beam

energy, analyzer crystal reflection, and analyzer crystal rocking curve position are essential for determining what current x-ray sources may be compatible. In addition, it is essential to determine the contribution and importance of absorption, refraction, and ultra-small angle scatter have on structural visualization in the breast.

1.2 Objectives

The goal of the research presented is to investigate the utility of Diffraction Enhanced Imaging and Multiple Image Radiography for the application of breast imaging, and in the process determine the optimal system parameters for this application both using a synchrotron and conventional x-ray source.

Aim 1: To develop imaging and quality control procedures for breast imaging at the National Synchrotron Light Source, including standardization of image normalization and processing. Science requires precision, accuracy, and reproducibility, which is difficult to accomplish with manual processing of image plates.

Aim 2: To stabilize the crystal optics used in a DEI system to minimize or eliminate system instability and analyzer drift. In order to utilize more elaborate and complicated processing algorithms such as MIR and MIR-CT, maintaining a stable system over time is a mandatory prerequisite.

Aim 3: To perform a reader study using conventional mammography phantoms that investigates the primary DEI system parameters. This study provides insight into how the incident x-ray beam energy, analyzer crystal reflection, and rocking curve position affects image feature visualization.

Aim 4: To assess the visualization of Diffraction Enhanced Imaging and Multiple Image Radiography contrast components in pathology proven breast cancer specimens at

multiple x-ray beam energies. This study builds upon the phantom based parameter study and investigates the energy dependence of absorption, refraction, and ultra-small angle scatter for breast tissue. The beam energies selected for the study area based on the characteristic x-ray energies for molybdenum and tungsten x-ray tubes.

Aim 5: To demonstrate that 60 keV x-rays can be used to generate diagnostically useful soft tissue images without relying on x-ray absorption. Producing soft tissue radiographs without absorption is a paradigm shift in x-ray imaging theory, relying on completely different contrast mechanisms.

Aim 6: To analyze the materials properties of breast cancer spiculations using Multiple Image Radiography and determine of these values are consistent across different specimens. In order to more accurately determine the optimal energy for a non-synchrotron based DEI/MIR system, determining which contrast mechanisms are necessary to produce diagnostically useful images is critical.

Aim 7: To generate the technical specifications and requirements for a non-synchrotron based laboratory DEI/MIR system.

1.3 Organization

Diffraction Enhanced Imaging is a novel imaging technology, and the physics associated with its use and development can be foreign even for those experienced in medical physics. A primary objective of this dissertation is to provide enough background for people of differing backgrounds to understand the physics and mechanics of DEI and its potential for use in breast imaging and cancer detection. Chapter 2 provides a general overview of the epidemiology of breast cancer, common types of breast cancer, and examples of how these

cancers appear on conventional mammograms. This chapter also provides a general description of how cancers are diagnosed and current methods of treatment.

The information presented in Chapter 3 provides an overview of x-ray generation, photonics, and photon interactions with matter. This chapter explains the physical mechanisms of x-ray absorption, refraction, and scatter and how they relate to DEI. The topics of energy deposition, dose measurement, and the associated health effects of radiation exposure are also discussed.

An overview of the physics, development, and use of the mainstream imaging modalities used for breast imaging is presented in Chapter 4. The modalities described are x-ray imaging, ultrasound, magnetic resonance imaging, computed tomography, single photon emission computed tomography, scintimammography, and positron emission tomography.

Chapter 5 expands on the development of mammography, with special emphasis on the development of the first dedicated mammography unit and subsequent major improvements. A description of the clinical trials performed to assess the utility of mammography and mortality reduction are presented to give the reader an idea of what challenges will have to be overcome of DEI is to become a clinically useful imaging modality.

The mechanics and physics of DEI is presented in Chapter 6, including a detailed description of the X-15A DEI beamline at the National Synchrotron Light Source (NSLS). This chapter will provide enough insight to understand the general mechanisms of DEI and how image contrast is generated. Multiple Image Radiography is a DEI based imaging processing method that provides a more complete description of an object's absorption, refraction, and ultra-small angle properties. This method, described in Chapter 7, will be used

to separate the contrast mechanisms in breast tissue and aid in determining the optimal system parameters.

Chapter 8 describes the imaging method and quality control procedures developed for breast imaging at the National Synchrotron Light Source. Implementing these procedures using MIR required an extensive overhaul of the system optics to reduce system instability, which is described in Chapter 9.

An initial assessment of the optimal imaging parameters for DEI are presented in Chapter 10, utilizing breast imaging phantoms to determine how DEI performs under various system parameters. Chapter 11 build upon the initial parameter study by using actual breast specimens and increasing the beam energy to 60 keV, an energy where there is nominal absorption contrast in soft tissue. This study also utilizes the Multiple Image Radiography technique to generate images representing an object's x-ray absorption, refraction, and ultra-small angle scatter. An analysis of contrast mechanisms in breast cancer speculations are presented in Chapter 12.

The culmination of this body of work is a description of the technical specifications of a potential non-synchrotron based DEI/MIR imaging system, presented in Chapter 13. Prior to this work, DEI for the breast imaging application was considered unrealistic due to the extreme flux and heat generation needed to image at 18 keV using a molybdenum source. The work presented in this dissertation demonstrates the novel idea that soft tissue can be imaged and visualized without x-ray absorption, thus allowing for imaging at higher energies. Imaging at higher energies, such as 60 keV, increases the photon efficiency, decreases the heat generation, reduces the absorbed dose, and is compatible with conventional tungsten x-ray sources.

Chapter 2: Overview of Breast Anatomy and Breast Cancer

2.1 Epidemiology of Breast Cancer

Breast cancer is currently the most common cancer in females, and is second only to lung cancer for cancer deaths in women. The most recent epidemiological studies indicate that an estimated 211,300 women will be diagnosed with breast cancer in 2003, and nearly 40,000 will die from this disease (Jamal et al. 2003). Approximately 1 in 10 women with a breast lump or abnormal mammogram will have a breast cancer (Kerlikowske et al. 2003).
The incidence of breast cancer is highest in North America and Northern Europe, and lowest in Asia and Africa. While the overall mortality rates from breast cancer have been relatively constant since 1950, there have been fluctuations among different subgroups. Mortality rates for women under 55 have decreased, while an increase has been observed for women over 55 (Chevarley and White 1997).

Sociodemographic risk factors associated with the development of breast cancer include gender, age, socioeconomic status, and race. There is a 100 fold difference in the incidence of breast cancer between men and women. Age has been shown to have a significant association, with the incidence of breast cancer rising sharply until the ages of 45 or 50. At this point the increase is less pronounced, and actually begins to decrease after age 80 (Pike et al. 1993). Approximately 85 percent of all breast cancers occur after age 40, and 66 percent after age 50 (Beckman 1998).

Women of higher socioeconomic status have an increased risk of developing breast cancer, with nearly a two-fold difference from the highest to lowest socioeconomic classes. The prevailing theory explaining this is a difference in educational and occupational trends that influence parity, age at first birth, and the age at menarche (Kelsey, Fischer and Holford 1981). Breast cancer is the most common cancer in women in every major ethnic group, but there are differences in incidence rates. Most ethnic differences are attributable to differences in lifestyle and socioeconomic status, some of which are also associated with treatment and survival. With a disparity in the utilization and availability of health care, an analysis based solely on race becomes confounded by other factors. Over the last two decades, the mortality rate from breast cancer has decreased by approximately 7% in younger white women. African American women have yet to realize similar mortality reductions, and older African American women have experienced an increase in mortality, despite a lower incidence of disease than their white counterparts (Mandelblatt et al. 2004). While there are numerous factors that may be contributing to excess mortality, a portion may be due to low rates of screening, failure to receive timely and complete diagnostic follow-up, or receiving suboptimal treatment (Mandelblatt et al. 2004).

2.2 Anatomy and Development of the Human Breast

The functional structures of the breast, or parenchyma, consist of an elaborate series of ducts and lobules surrounded by interlobular fibrous tissue. The parenchyma of the breast is surrounded by varying amounts of adipose tissue, both of which contribute to the density of the breast (Bartow 1999).

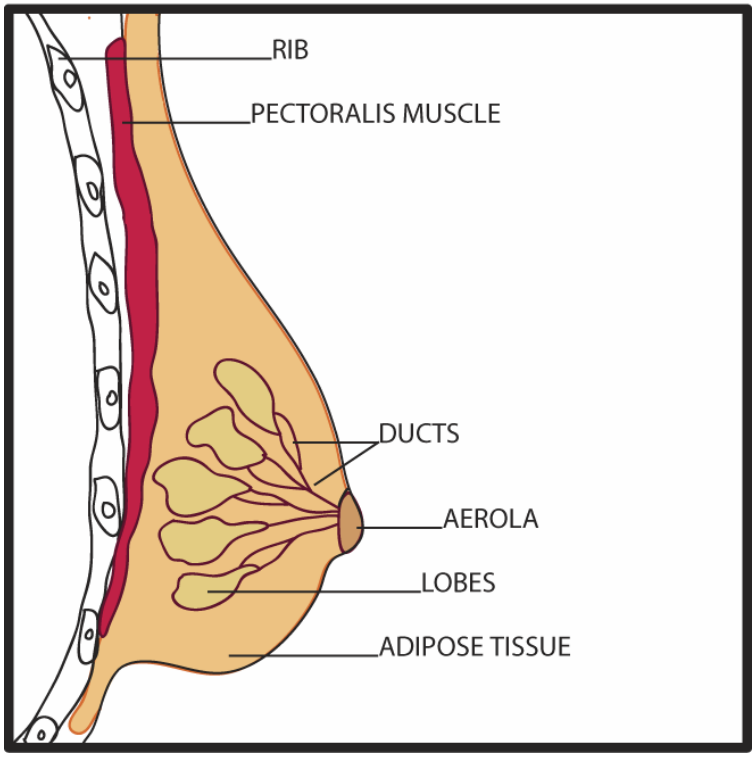

FIGURE 2.1: Breast anatomy

Male and female breast development is similar until puberty, at which time the female breast undergoes significant hormonally-induced changes. Pre-pubertal development is marked by the creation, elongation, and branching of lactiferous ducts. Increasing levels of estrogen at menarche induces the development of the lobular terminal ducts (Bartow 1999). During puberty in females, the breast begins to grow and the aerolae enlarge. The lactiferous ducts lead to the formation of buds that form 15 to 20 lobules of glandular tissue (Moore 1992).

The intermediate ductal structures, once formed, are stable and are not affected by fluctuating hormone levels. In contrast, the terminal ducts are dynamic and can undergo significant alterations in response to changing hormone levels. The most dramatic changes occur during pregnancy, but cyclical changes also occur during the menstrual cycle (Bartow 1999).

2.3 Benign Conditions

The most common benign breast conditions are fibrocystic changes, breast inflammation, and benign breast tumors. Fibrocystic changes can be classified as non-proliferative and proliferative. Non-proliferative fibrocystic changes are associated with an increase in the dense fibrous stroma and a cystic dilation of the terminal ducts. Since the terminal ducts are responsive to hormone levels, lumps associated with fibrocystic changes can fluctuate in size and tenderness during the menstrual cycle. Proliferative fibrocystic changes are proliferative epithelial changes that can not be predicted from clinical or radiographic studies. Ductal epithelial hyperplasia is the most common form and in some cases can lead to papillary structures within the lumen of the peripheral ducts, a condition also referred to as papillomatosis (Bartow 1999). Histologically, fibrocystic changes occur in three stages. The first stage is marked by a proliferation of stroma, frequently in the upper outer quadrant of the breast, which leads to induration and tenderness. Progression leads to adenosis, which can result in cyst formation. Cysts at this stage range from microscopic to approximately 1 cm in diameter. In the later stages of fibrocystic change, larger cysts are present but with a decrease in pain experienced by the patient (Beckman 1998).

The most common benign tumor of the breast originates from the terminal duct lobular unit and is called a fibroadenoma. A fibroadenoma is a round, rubbery, and well circumscribed mass that is freely moveable in the breast. Fibroadenomas typically have a glistening gray-white interior with well defined borders. This is in contrast to most malignant tumors, which are usually securely attached to the surrounding tissue and are relatively immobile. Fibroadenomas are typically solitary, but multiple fibroadenomas can develop in 15 to 20 percent of patients (Beckman 1998).

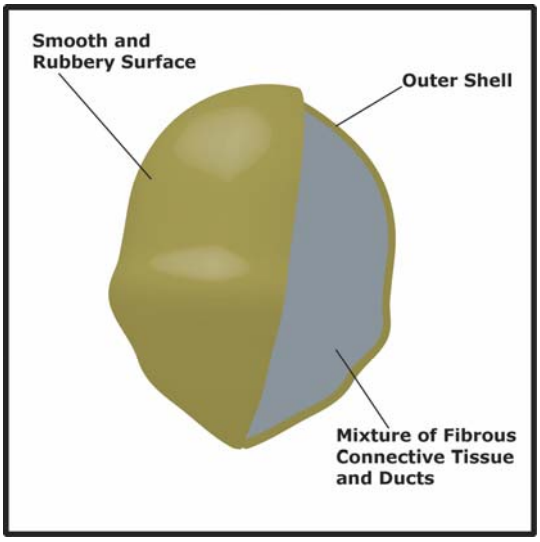

FIGURE 2.2: Graphical depiction of a breast fibroadenoma

The lack of significant attachment to the surrounding tissues allows for the lesion to be easily enucleated during surgical excision. While fibroadenomas are benign and have no malignant potential, the frequency of their occurrence combined with their radiographic appearance makes their diagnosis key in determining whether a lesion is benign or if it is potentially malignant and warrants further investigation. A clinical breast exam can be used to determine if the mass is mobile or fixed, but mammography and ultrasound are normally employed for characterization. A fibroadenoma is sharply demarcated from the surrounding tissue, which can be identified by mammography. If a radiologist can see that the entire circumference of the mass is well-circumscribed, then that information combined with a clinical breast exam can identify the lesion as benign.

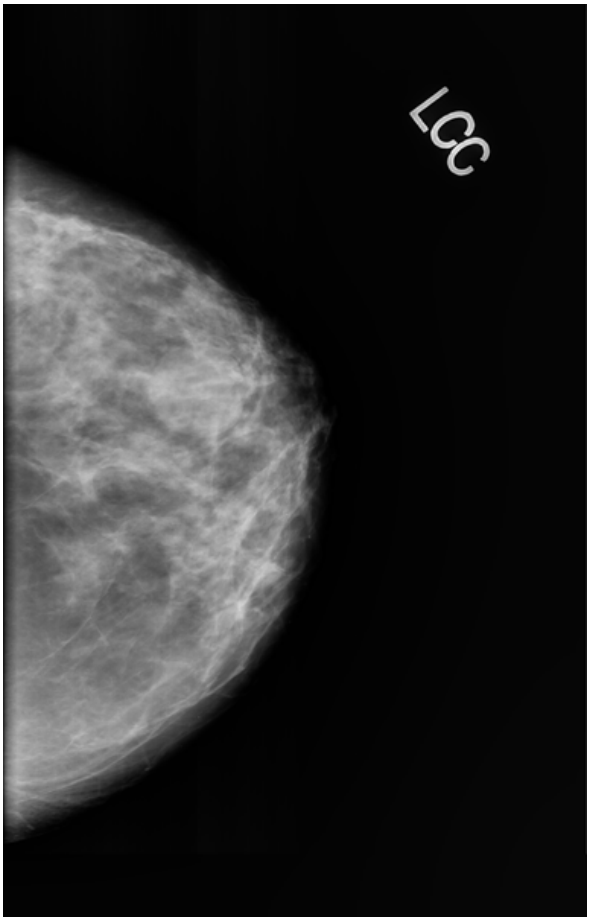

FIGURE 2.3: Full field mammogram with benign fibroadenoma

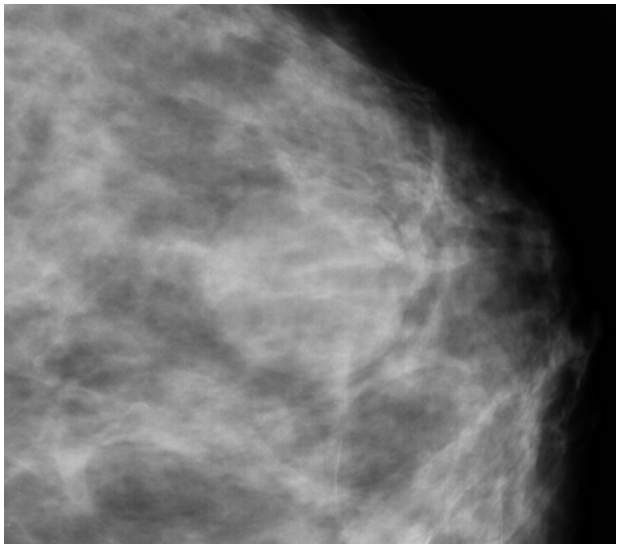

FIGURE 2.4: Close up view of a fibroadenoma. Note the well circumscribed border between the lesion and the surround breast parenchyma

Unfortunately, there is at least some ambiguity even when using a combination of mammography and ultrasound for characterization. If a portion of the lesion is obscured by structural noise and its borders are not clearly defined, further investigation, including biopsy, may be warranted.

Intraductal papilloma is another benign tumor occurring in middle-aged and older women that is often associated with a serous or bloody nipple discharge. An intraductal papilloma is a single tumor that is attached to the wall of the larger ducts by a fibrovascular stalk.

Benign tumors can also originate from the fatty tissue of the breast, but their characteristics can make them difficult to distinguish from malignancy. Lipomas are benign tumors that are composed of mature fat cells, and are the most common mesenchymal tumor. They are generally a few centimeters in size but can be diffuse and rubbery. Fat necrosis is uncommon and usually the result of trauma, presenting as a solitary, tender, ill-defined mass. The radiographic similarities of fat necrosis with malignant conditions often requires further evaluation and biopsy to establish a diagnosis (Beckman 1998).

A disease found predominantly in the fifth and sixth decades of life is mammary duct ectasia, and can also mimic a carcinoma clinically and on a mammogram. Mammary duct ectasia refers to a dilation of the large and intermediate breast ducts, a result of the shortening and dilation of the subaerola as they involute. This condition is associated with chronic intraductal and periductal inflammation, and presents with a thick gray to black nipple discharge, pain, and nipple tenderness (Beckman 1998).

2.4 Pre-Malignant and Malignant Tumors

Ductal carcinoma in situ (DCIS) is defined as a clonal proliferation of cells that appear malignant and accumulate within the lumens of the mammary duct (Burstein et al. 2004).

DCIS is a lesion which lies along a spectrum of disease that has the potential to progress from atypical hyperplasia to invasive breast cancer (Burstein et al. 2004). Changes in the surrounding breast parenchyma may be associated with DCIS, which can help in radiographic detection. High-grade ductal carcinoma has been associated with the breakdown of the myoepithelial cell layer and basement membrane surrounding the ductal lumen, proliferation of fibroblasts, lymphocyte infiltration, and angiogenesis in the surrounding stromal tissues (Burstein et al. 2004). Recent data indicates that DCIS represents a stage of disease in which the molecular changes that are found in invasive breast cancers are already present, but the lesion has not developed a fully malignant phenotype. The step leading to invasive disease is usually associated with a gain of function in the malignant cells and a concomitant loss of function and integrity in the surrounding normal tissues. Before the use of widespread screening mammography, DCIS was normally diagnosed after finding a palpable lesion or other atypical clinical finding that warranted further investigation. With the advent of widespread screening mammography, the incidence of DCIS has increased from 4800 cases in 1983 to more than 50,000 cases in 2004. Approximately 90 percent of ductal carcinomas in situ are diagnosed while they are clinically occult because of mammographic detection of microcalcifications (in 76 percent of cases), soft-tissue densities (11 percent), or both (13 percent) (Burstein et al. 2004). Clinically, the critical aspect of assessment is distinguishing DCIS from invasive cancer. Classifying DCIS is determined by the nuclear grade of the tumor cells (low, intermediate, or high), the architectural pattern of tumor growth (solid, papillary, micropapillary, or cribiform) and the presence or absence of comedonecrosis (Burstein et al. 2004).

Lobular carcinoma in-situ (LCIS) is a pre-malignant condition that has the potential to develop into breast cancer. In contrast to intraductal carcinoma, lobular carcinomas develop in the terminal duct lobular unit. The cells of LCIS are generally smaller and more monotonous than cells in intraductal cancers. The cells are typically round, with regular nuclei and minute nuclei. These cells do not form papillary or cribiform structures, instead appearing as solid clusters that fill and distend the terminal ducts. However, the distention of the ductal system is normally less than that observed with ductal carcinoma in situ. The progression of lobular carcinoma in situ does not normally undergo central necrosis as often occurs with intraductal carcinoma, but microcalcifications may be present in the ducts (Bartow 1999). A lack of significant distention in the ducts combined with a reduced prevalence of associated microcalcifications makes lobular carcinoma in situ difficult to detect radiographically, especially in its early stages. Histologically a neoplastic lesion, LCIS has long been considered a marker for increased breast carcinoma risk rather than a precursor for invasive carcinoma, because it appears to confer an equally increased risk of breast carcinoma in both the contralateral and ipsilateral breasts (Hwang et al. 2004).

Invasive ductal carcinoma is the most common type of breast cancer, comprising 70 to 80 percent of invasive lesions. The invasion of malignant cells into the stroma usually causes a fibroblastic proliferation of the surrounding tissue known as desmoplasia. It is the desmoplastic process that leads to the formation of a hard, fixed mass that is often the first clinical sign of ductal carcinoma (Bartow 1999).

Invasive lobular carcinoma is the second most common type of invasive cancer, accounting for approximately 5 to 10 percent of invasive lesions. Indications of invasive lobular carcinoma can vary from a discrete firm mass to a diffuse, indurated area (Bartow

1999). As with lobular carcinoma in situ, invasive lobular carcinoma is characterized by small, round cells that have little cytoplasm and extend into the breast stroma in a single file. The invasion of lobular carcinoma does not cause significant destruction to the surrounding normal anatomic structures or produce a significant connective tissue response (Arpino et al. 2004). The distinctive growth pattern of invasive lobular carcinoma does not normally create a mass that can be detected clinically or indirect changes that can be detected by mammography. An additional difficulty with lobular carcinomas is that they have an increased tendency to form multifocal and multicentric distributions, and bilateral occurrence (Arpino et al. 2004).

Tubular carcinoma is a rare from of mammary carcinoma, representing approximately 2% of all breast cancers. The cells of tubular carcinoma are well differentiated and are arranged in small tubules usually one cell layer thick immersed in an abundant desmoplastic stroma. Approximately 50% of tubular carcinomas are associated with microcalcifications. Radiographically, tubular carcinomas can resemble the benign conditions referred to as radial scar and sclerosing adenosis (Damiana and Eusebi 2002).

Medullary carcinoma of the breast accounts for approximately 5-10% of all breast cancers, and are described as well circumscribed tumors that have a prominent lymphocytic infiltrate and high grade cytology. The cells of these tumors form a tender firm nodule, with features that are similar to a fibroadenoma. Peritumoral fibrosis is often associated with medullary carcinomas and can give a false impression of encapsulation. There are five key histologic features that are used in the diagnosis of medullary carcinoma. A prominent lymphocytic infiltrate is present with a solid synctial growth pattern, marked by neoplastic cells that are arranged in broad, irregularly shaped sheets. The tumors have a well defined microscopic

circumscription, where normal breast tissue is never found within the tumor nodule. Cells associated with medullary carcinoma also have a high mitotic rate and large vesicular nuclei (Damiana and Eusebi 2002). The prognosis for patients with medullary carcinoma is considerably better than those with infiltrating ductal carcinoma (Bartow 1999).

Mucinous carcinomas are also well circumscribed tumors, often with multilobulated borders. These tumors are characterized as having invasive carcinoma cells immersed in large amounts of extracellular mucin. Mucin is a nitrogenous substance found in mucous that serves as a lubricant. Histologically, mucinous carcinoma is defined by the accumulation of extracellular epithelial mucins in the stroma of the breast. The five year prognosis for patients with mucinous carcinoma is good, with a disease free percentage ranging from 84-100%, a prognosis considerably better than for infiltrating ductal or lobular carcinoma (Damiana and Eusebi 2002).

2.5 Mammography Interpretation and Classification Schemes for Malignancy

Although each clinician may have a particular system for reading mammograms, most have adopted a systematic and generalized procedure for mammographic interpretation. The first step in the process is comparing radiographs of the right and left breast for symmetry, and comparing these films with previous mammograms if available. Features that may indicate an abnormality include masses, clustered microcalcifications, architectural distortions, and asymmetries. The structural information obtained from a mammogram is not sufficient to diagnose a particular type of malignancy, but it does act as an indicator of a possible underlying malignancy. Masses that may indicate malignancy are typically dense with irregular borders, and can also have spiculations extending from the central mass.

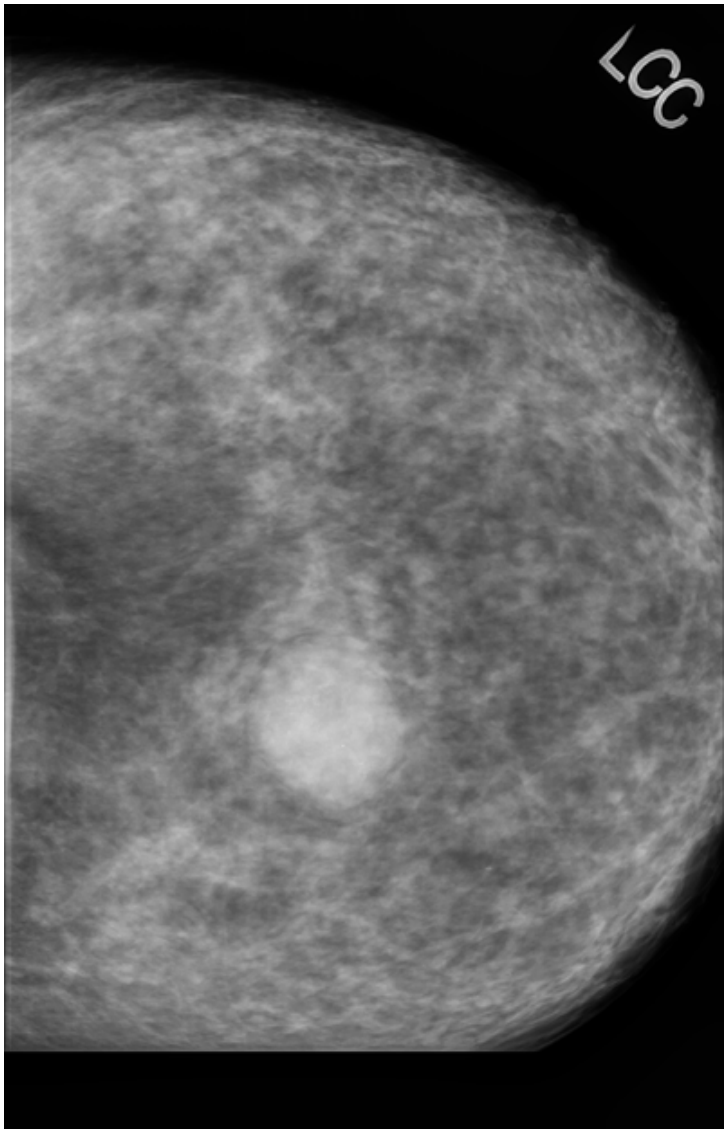

FIGURE 2.5: Digital radiograph of a malignant mass

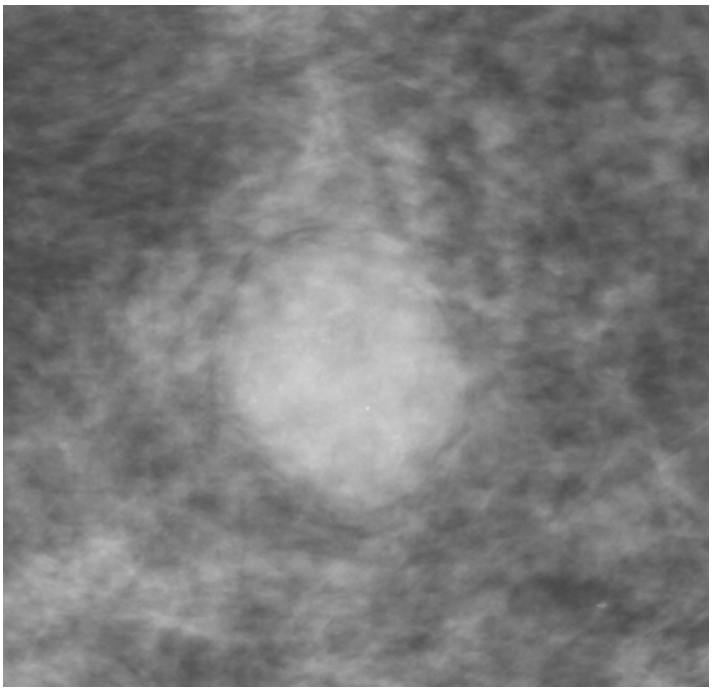

FIGURE 2.6: Magnified view of malignant mass

A new or enlarging mass is another indicator of a possible malignancy, which could lead to a biopsy for a definitive diagnosis (Donegan 2002). Some breast cancers are extremely aggressive and grow at an atypically fast rate, but most tumors follow a predicable rate of growth. The development and growth of a mass is often estimated using a doubling time of one hundred days. At this rate starting from a single malignant cell, it may take years for the lesion to be visible on mammography or become palpable.

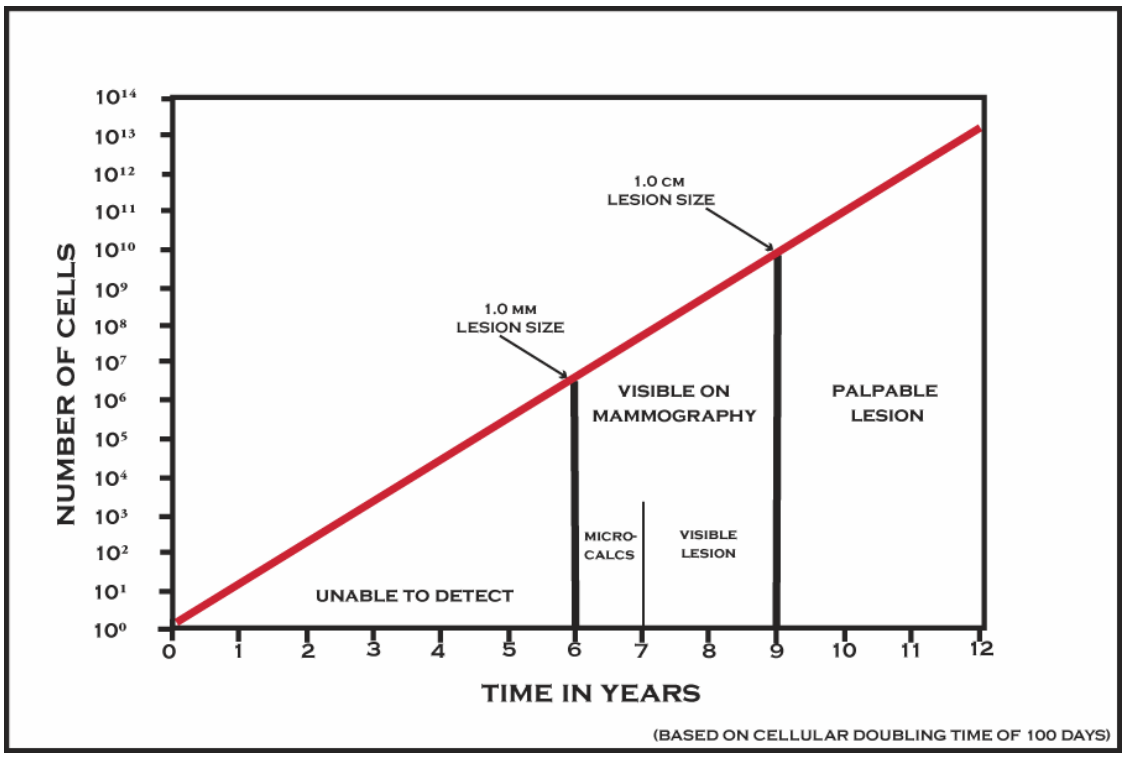

FIGURE 2.7: Model of tumor development and detectability (Beckman 1998)

Calcifications are another indictor of a possible malignancy, but their size and structural pattern are what lead the radiologist towards a benign or suspicious classification. For example, large calcifications referred to as “popcorn” calcifications are almost always benign. Calcifications that appear as tortuous parallel lines are most likely just calcified vessel walls, and benign oil cysts are described as having circular calcifications with lucent centers. Suspicious calcifications are very small, usually 0.1 to 1 mm in diameter, and are found in clusters. A cluster is typically defined as 5 or more calcifications within an area of 1.0 cm^2. The probability of an underlying cancer increases in proportion with the number of clustered calcium specks (Donegan 2002).

One of the key prognostic indicators of survival is the size and distribution of a malignancy at the time of detection. A standardized system of classification is necessary to define normal tissues and characterize lesions in the clinical setting. The most widely used

tumor staging system is based on the size of the tumor, the extent of nodal involvement, and whether the tumor has undergone metastasis. The system known as the TNM staging classification which is published by the American Joint Committee on Cancer (AJCC) underwent a significant modification in 2002. Using the TNM system allows for an easily recognized descriptor to be applied to a tumor that can be interpreted by a diverse team of health care professionals. One of the most important aspects of a tumor is size, which has been shown to have a direct correlation to patient outcome. The categories into which tumor sizes are separated are based on the survival rates associated with the general size of a tumor. Progression of a malignancy to the lymph node system is another prognostic indicator of disease status and survival, which is reflected in the various staging levels for nodal status. The most profound factor, as well as the most difficult to assess, is whether a malignancy has metastasized. If a cancer has been detected in a site distant from the primary tumor, the highest and least favorable classifications are applied.

The TNM staging system is effective for pathologic classification, but it is not an effective classification scheme for breast cancer screening. Breast imagers are charged with the task of interpreting mammograms and determining the likelihood that a cancer is present, a process which involves the experience of the radiologist and statistical probability. In order to standardize the assessment of risk so that it can be understood and quickly interpreted by a wide range of health care professionals, the American College of Radiology (ACR) developed the Breast Imaging Reporting and Data System (BI-RADS). The Breast Imaging Reporting and Data System was created with the primary objective of improving communication of mammographic results and providing outcomes monitoring to improve the quality of patient care. Benefits of using the BI-RADS system include the ability to generate

standardized reports across mammographic facilities, which can potentially reduce the report interpretation time for a primary care physician. Improvements in communication among health care professionals can encourage follow-up and compliance, and using a standardized method could help to optimize the standard of care by balancing benefits and resources. (Lacquement, Mitchell and Hollingsworth 1999).

The BI-RADS system sets up broad categories for interpretation, which is helpful for determining the proper course of diagnostic evaluation and treatment. There are 7 distinct BI-RADS categories, 0-6, which indicate whether the assessment is complete or incomplete and categories a patient's exam information. A BI-RADS Category 0 rating indicates that the mammographic assessment is incomplete, and that additional imaging and/or prior mammograms are needed for comparison. If a mammographic exam is complete and the radiologist has nothing to comment on, specifically that the breasts are symmetric with no masses, architectural distortions, or suspicious calcifications, a Category 1 assessment is used. If a benign finding is observed, such as a calcified fibroadenoma, multiple secretory calcifications, oil cysts, lipomas, galactoceles, and mixed density hamartomas, a Category 2 assessment is used. These findings have a characteristically benign radiographic appearance, and a Category 2 assessment is a normal assessment. A Category 3 assessment is used for a probably benign finding, but an initial short-interval follow-up mammograms suggested. Findings placed in this category, such as a noncalcified circumscribed solid mass, should have less than a 2% risk of malignancy, and the finding is not expected to change over the course of the follow-up interval. A follow-up interval is used by the radiologist to establish lesion stability, which reinforces a benign classification (Breast Imaging-Reporting and Data System 2006).

Lesions that do not have a classic appearance of malignancy but do have a wide range of probability of malignancy are placed in Category 4. Lesions in Category 4 indicate a suspicious abnormality, and a biopsy should be considered. Most recommendations for interventional procedures are placed in this category, which is subdivided into three subsections, 4A, 4B, and 4C. Dividing this category into three sections allows a radiologist to further define the relevant probability of malignancy, and use this information to work with the patient to make an informed decision on the best course of action (Breast Imaging-Reporting and Data System 2006).

If a lesion has a high probability of malignancy, greater than 95%, a Category 5 assessment is given indicating that appropriate action should be taken. Lesions that are deemed almost certainly malignant are in this category where a one-stage surgical treatment may be considered without a preliminary biopsy. Lesions which have been identified in an imaging study and have been proven malignant by biopsy are given a Category 6 assessment (Breast Imaging-Reporting and Data System 2006).

The BI-RADS assessments have been adopted and are now required by the United States Food and Drug Administration for reporting of mammographic findings and management recommendations. Studies evaluating the effectiveness of BI-RADS indicate that the classification system does improve the quality of risk assessment information by making the positive predictive value more specific to a patient's mammogram rather than to an overall positive predictive value (Lacquement, Mitchell and Hollingsworth 1999).

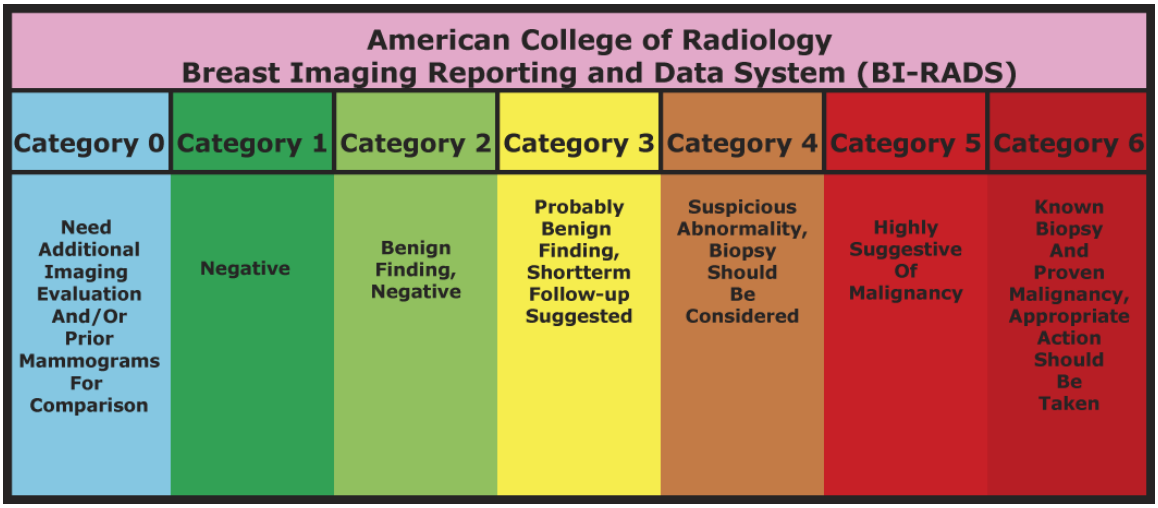

FIGURE 2.8: Breast Imaging Reporting and Data System (BI-RADS) categories

Chapter 3: Photon Interactions with Matter

3.1 The Photoelectric Effect and X-ray Absorption

The most important underlying physical interaction in conventional radiography is the photoelectric effect. In its most general sense, the photoelectric effect is the process by which electrons are emitted from a surface as a result of incident electromagnetic radiation.

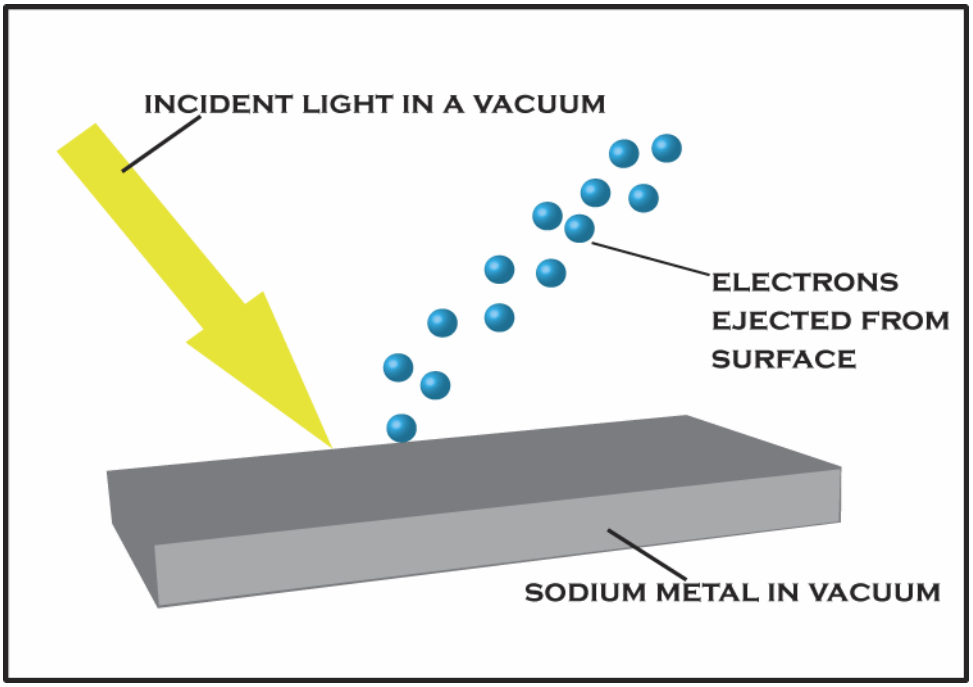

FIGURE 3.1: Elementary depiction of the photoelectric effect

First discovered in 1887 by Heinrich Rudolph Hertz, Hertz observed that ultraviolet light affects the voltage at which sparking occurs between electrodes. While the idea was established that incident light could eject electrons from a surface, scientists still did not have a physical model and theory for the process. At that point, the properties of electromagnetic radiation were based on the classical Maxwell theory of light. If light could be described as a

wave, then the number and energy of the ejected electrons would be a function of the intensity of incident wave. One of Hertz's assistants, Philipp Lenard, performed a series of experiments that demonstrated conclusively that the energy of the electrons was independent of the intensity of the incident light.

As was often the case in the early 20^{th} century, Albert Einstein was able to provide the clarity and insight to fully describe why the experimental data and established theory were inconsistent. In 1905, Einstein proposed his theory of the photoelectric effect, which introduced the revolutionary idea that light travels in packets, or quanta. Einstein proposed that the frequency of these individual quanta, or photons, determined the energy of the electrons ejected from a surface. The energy of each quanta was defined by the equation, $E=hf$, where h is Planck's constant ($h = 6.626069 \times 10^{-34}$ Joule seconds), and f is the frequency. Increasing the number of photons that are incident on a surface will increase the number of electrons that are emitted, but not the average energy. An increase in the average energy of the electrons can only be achieved by increasing the frequency of the photons. Einstein's theory of the photoelectric effect correctly described this effect in nature and, in the process, redefined the world's understanding of electromagnetic radiation. For his description of the photoelectric effect, Einstein was awarded the Nobel Prize in Physics in 1921.

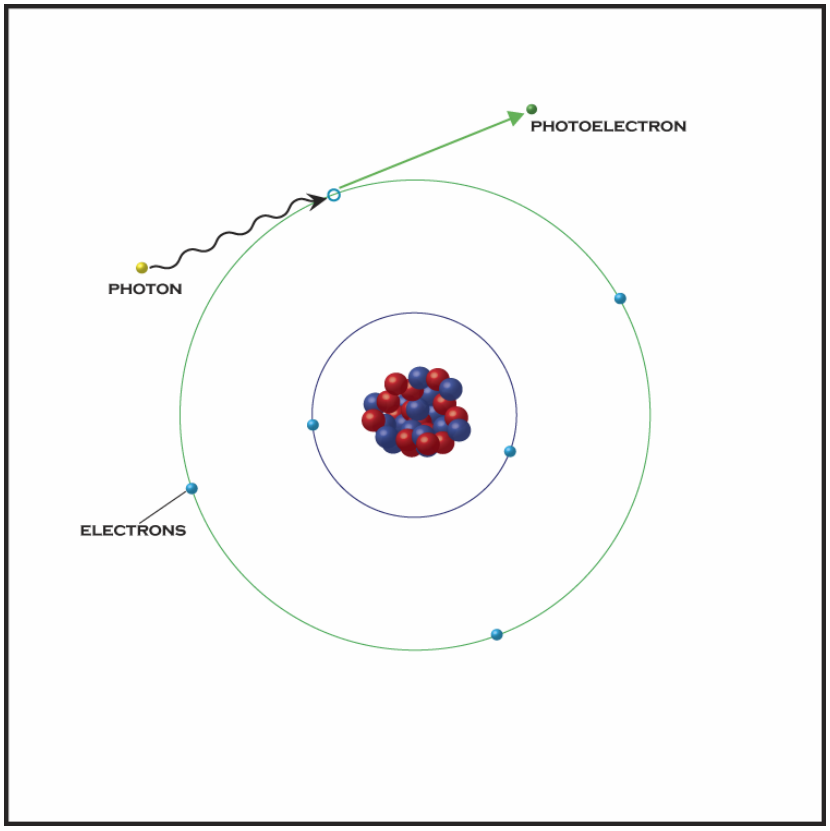

FIGURE 3.2: Example of the photoelectric effect on the atomic level

Application of this theory to x-ray imaging helps to explain how contrast is obtained in conventional radiography. X-rays passing through an object, such as breast tissue, can strike an electron and raise its energy to a level above the binding energy of that orbital. If this occurs, the electron will have sufficient energy to overcome the attractive force of the nucleus and leave the atom with a total energy equal to the energy of the incident photon minus the binding energy of the electron. In biological tissues, incident x-rays can lead to direct or indirect free radical formation, which can interact with DNA and other cellular structures leading to mutations and other deleterious effects. The positive aspect of this interaction is that the energy of the x-ray photon is transferred to the electron, which means that it will not encounter the film or detector of an imaging system. Decreasing the amount of transmitted x-rays through an object is referred to as x-ray attenuation, and the primary

component of this process in conventional imaging is through absorption via the photoelectric effect.

The probability of photoelectric absorption occurring per unit mass is proportional to Z^3/E^3, where Z is the atomic number and E is the energy of the incident photon (Bushberg et al. 2002). For medical imaging, the equation is often simplified to reflect the effect of beam energy, making the probability of photoelectric absorption proportional to $1/E^3$. Since contrast in conventional radiography is based on absorption, absorption contrast will decrease rapidly at higher energy levels. An exception to this trend occurs at the K-absorption edge of an atom, a characteristic energy specific to each element. The probability that a photoelectric interaction will occur increases significantly when the incident photon energy is just below the K-absorption energy, or K-edge (Bushberg et al. 2002).

Since photoelectric absorption is increased with higher atomic number and lower beam energy, imaging breast tissue becomes a challenging endeavor. Most of the primary elements in soft tissue are composed of hydrogen, carbon, nitrogen and oxygen, all of which have relatively low atomic numbers and absorption edges below 1 keV (Bushberg et al. 2002). Both the relatively low average atomic number and low absorption edge of the primary elements composing the parenchyma of breast tissue make determining differences between benign and malignant features challenging, especially in the early stages of disease.

3.2 Bremsstrahlung and Characteristic X-rays

A physical interaction inherent to conventional x-ray generation is that of bremsstrahlung, which is German for "breaking radiation". Electrons at non-relativistic velocities used in imaging systems are accelerated through a voltage and have a kinetic energy defined by the equation

$$KE = \frac{1}{2}mv^2.$$

Electrons emitted into a metal, such as the anode of an x-ray tube, can be deflected as they pass by the dense atomic nuclei and decelerate rapidly.

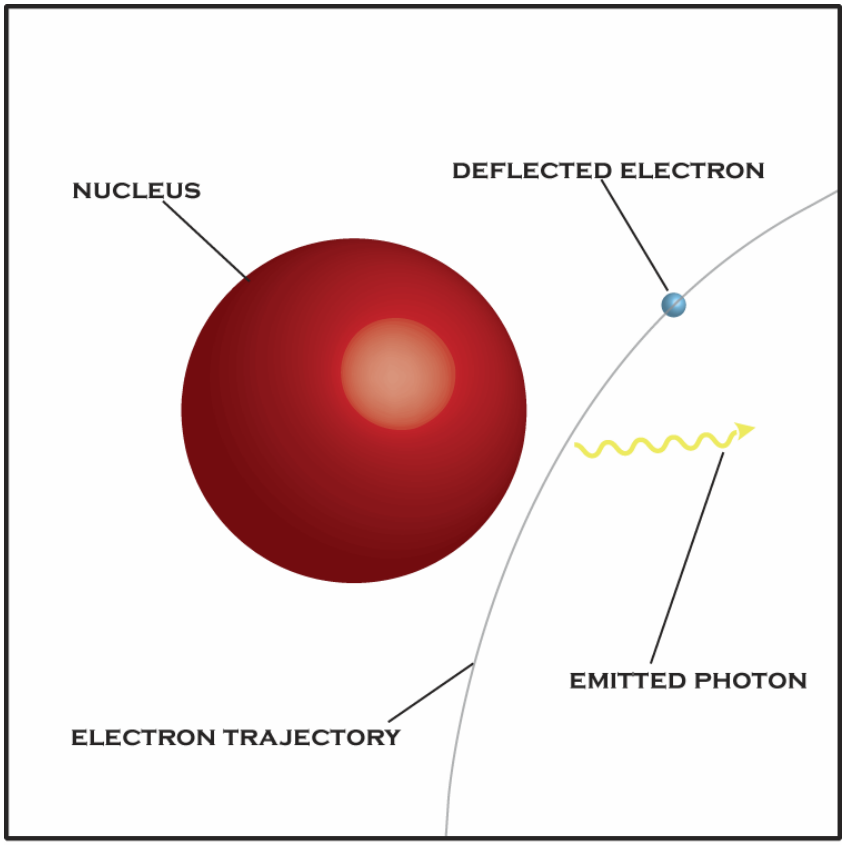

FIGURE 3.3: Generation of bremsstrahlung radiation

An electron can release energies ranging from 0 to its total KE, with the loss of energy dependent on how close the passing electron is to the nucleus. Deflections that result in a low energy release have a much higher probability than those that result in a large energy release. Electrons that are accelerated at high potentials and have a strong interaction with the nucleus that results in a significant decrease in velocity can result in the release of a photon in the x-ray band of the energy spectrum. The main source of x-rays generated from diagnostic x-ray tubes comes from bremsstrahlung radiation.

Accelerated electrons interacting with an atom can produce another type of x-ray based primarily on the object's atomic properties, known as characteristic x-rays. If an accelerated electron encounters an electron in an atomic orbital, part of its energy can be transferred and raise the impacted electron to a higher energy level. Ejection of the impacted electron can occur if the energy transferred is equal to or greater than the binding energy of that electron. If an interaction occurs that ejects one of these electrons, an electron from a higher energy level will drop to fill the gap. Since these electrons are going from a high energy level to a lower energy level, the change in energy level is accompanied with a release of energy. An electron that transitions from the second energy level to the first energy level (n=2 to n=1) are referred to as a K_α x-rays. Transitions from the third energy level to the first energy level (n=3 to n=1) are classified as K_β x-rays.

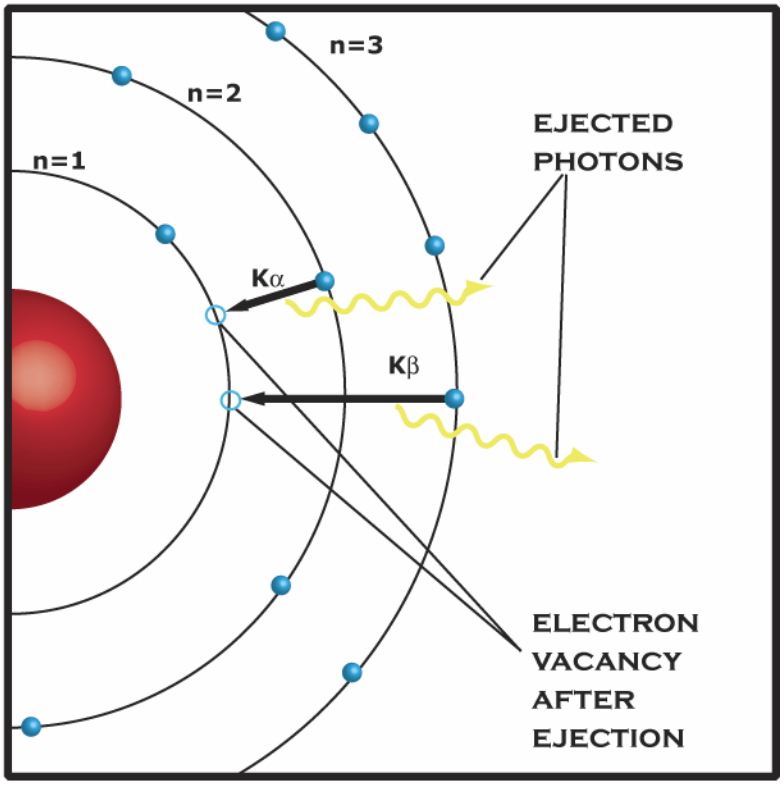

FIGURE 3.4: Generation of K_α and K_β characteristic x-rays

There are numerous transitions that can occur based on this electronic collision, but the interactions that generate characteristic x-rays are produced by transitions in the lower atomic energy levels.

The energy output spectrum of an x-ray target will depend on the properties of the metal being used. Determining the average energy needed for a particular imaging application is important in selecting a target. For applications that utilize monochromatic x-rays, the characteristic x-rays produced by a target are of particular importance.

3.3 X-ray Absorption

The photon interaction that has had the most profound impact on conventional radiography is x-ray absorption. When x-ray photons encounter matter, the interaction leads to an attenuation of the incident x-rays, with a portion of the x-rays being absorbed and a portion being transmitted. X-ray attenuation is a loss in photon intensity based on electron density and mean atomic number of an object. Scattering of x-rays can also occur as photons pass through matter and lead to a loss in intensity, but this component is difficult to measure in conventional radiography. Quantification of the amount of photons that are absorbed as they pass through an object of thickness X is determined by how many photons are transmitted (I_t) compared to the number of photons in the incident beam (I_o).

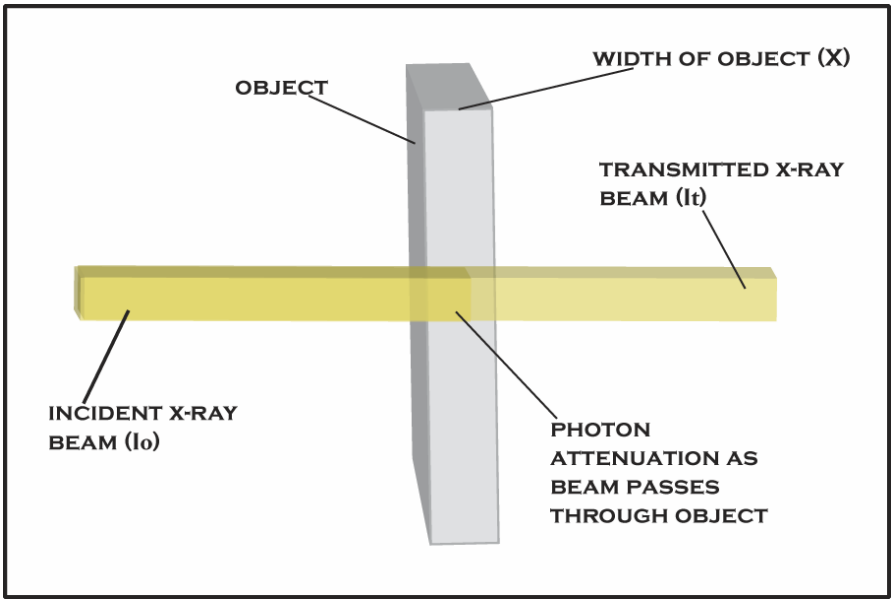

FIGURE 3.5: X-ray attenuation

The degree to which photons are attenuated as they pass through matter is a materials property that can be measured, and is termed the attenuation coefficient (μ) with units of cm^{-1}. Differences in the linear attenuation coefficients allow for x-ray image contrast, with the highest contrast being between areas of high and low attenuation.

The linear absorption coefficient is proportional to the density of the material traversed, and the tabulated value is often expressed as μ/ρ. This value is called the mass absorption coefficient and it is independent of the physical state of the material (solid, liquid, or gas).

3.4 X-ray Refraction

The refraction of light as it passes from one medium to another was first discovered by Willebrord Snell, and the law that defines this process is known at Snell's law. Mathematically, this relationship is defined as

$$n_1 \sin(\theta_1) = n_2 \sin(\theta_2)$$

where the incident medium is medium 1, and the refracted medium is medium 2.

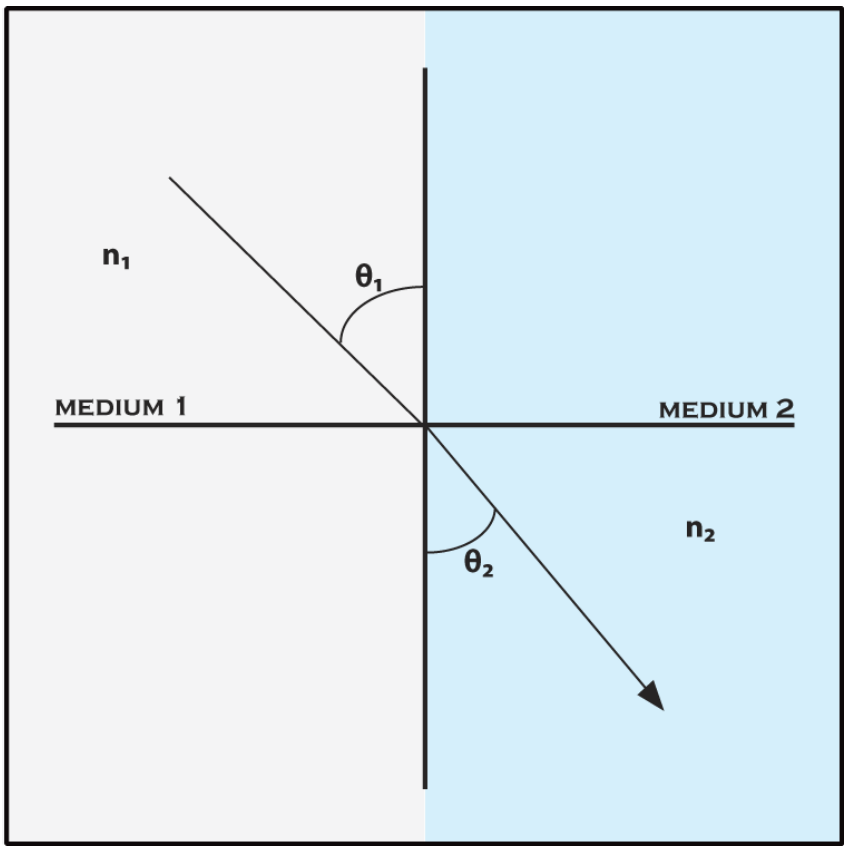

FIGURE 3.6: Refraction of visible light

Figure 3.6 illustrates the passage of an electromagnetic wave passing from one medium to another, with the deviation depending on the index difference. Using the classic example of visible light, the illustration demonstrates light moving from one index of refraction to a medium with a higher index of refraction. This example is commonly used to demonstrate refraction of visible light, but the law also applies for x-rays. However, for x-rays, the real parts of the complex refractive indices are less than unity and can be expressed as

$$n = 1 - \delta \, .$$

When using high-energy x-rays and materials with a low average atomic number, an approximation for δ is

$$\delta \cong \frac{N\lambda^2 r_e}{2\pi}$$

where N is the number of electrons per unit volume of the sample material, r_e is the classical electron radius, and λ is the x-ray wavelength. Using these equations one can show that for a linear interface between two regions with distinct refractive indices, an incident photon will be deflected at an angle Δθ approximated by

$$\Delta\theta \cong (n_1 - n_2)\tan\theta_1 .$$

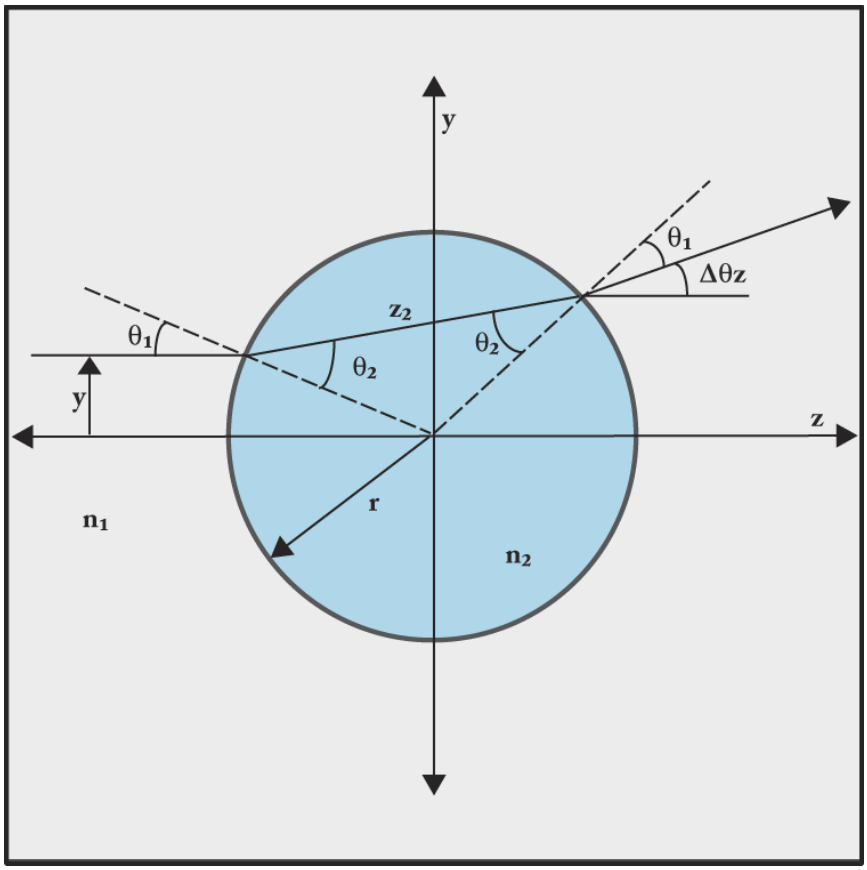

FIGURE 3.7: Refraction of x-rays through a cylindrical Lucite rod

The above diagram demonstrates the refraction of an x-ray as it passes from air through a cylindrical Lucite rod (Kiss, Sayers and Zhong 2003).

3.5 Coherent Scattering

Photons can primarily undergo three events when they encounter an object: they can pass through without any interaction, they can be absorbed through the photoelectric effect, or

they can undergo a scattering event. In its most general definition, scattering is an angular deviation in the path of a photon secondary to an interaction with another object. The characteristics of the photon, the medium it is traveling in, and the properties of the object it encounters has a profound impact on the outcome of the interaction. For this discussion, a description of the basics of x-ray scattering is sufficient to describe the primary interactions necessary for describing a DEI system.

Interactions that occur without a loss or transfer of energy are elastic, and x-ray interactions that occur without an associated loss of energy in the incident photon are referred to as elastic scatter, or coherent scatter. In a coherent scattering event, the energy of the primary x-ray photon is first completely absorbed and then re-emitted by the electrons of a single atom. There is no net energy loss in the interaction, but the direction of the photon re-emission is completely arbitrary.

For medical imaging, coherent scatter interactions are far less significant than photoelectric interactions or scattering events that occur with a loss of energy, known as incoherent scattering. Further discussions of DEI will demonstrate the importance of coherent scattering in this imaging modality.

3.6 Incoherent Scattering

In the energy ranges used in diagnostic imaging, the scattering interaction that is dominant and often problematic is incoherent scattering. This effect was first described by Arthur Holly Compton in 1922. Compton was performing studies on x-ray scattering, and during his investigations he noticed an increase in wavelength of x-rays due to scattering of the incident radiation by free electrons. The implication of this observation is that the scattered quanta have less energy than the quanta in the original beam, a process that is now known as the

Compton effect. Arthur Compton was awarded the 1927 Nobel Prize in Physics for his work leading to the understanding of this effect.

A Compton scattering interaction can be described as a collision between an x-ray photon and an electron in the outer energy level of an atom. The energy binding the outer electrons is minimal, and all of the energy lost in the interaction between the photon and the electron is transferred as kinetic energy to the electron. This transfer of energy results in a photon with decreased energy, or increased wavelength, and the ejection of the impacted electron from the atom.

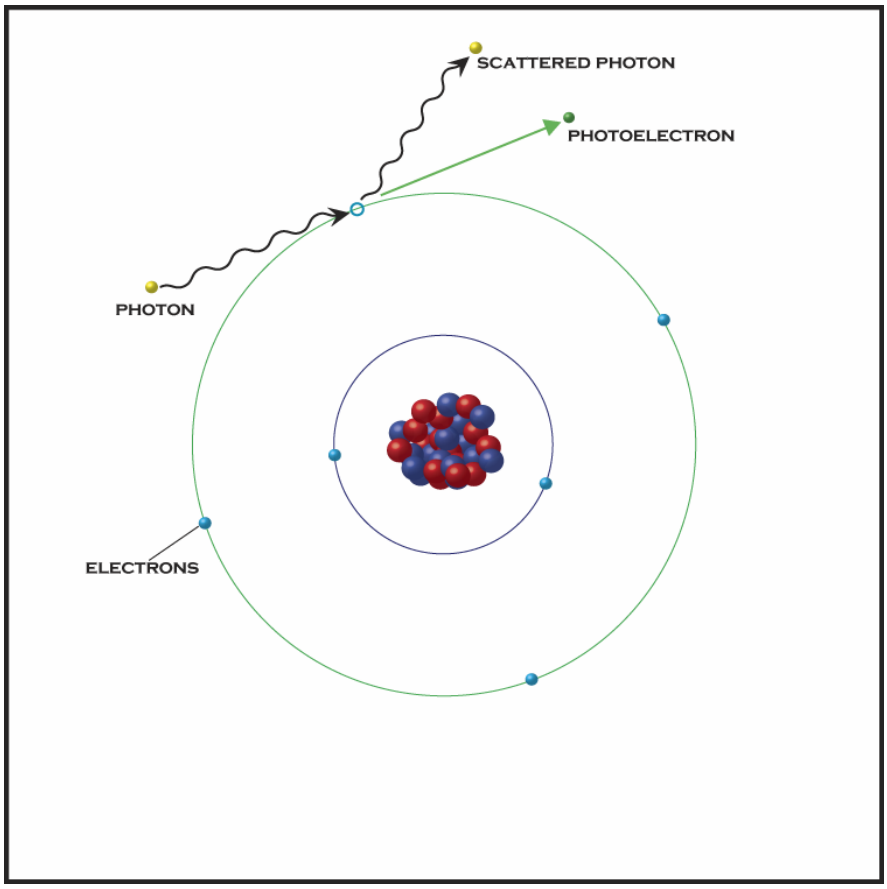

FIGURE 3.8: Compton scatter in an atom

Both energy and momentum are conserved in the collision, so the energy and angular deviation of the scattered photon will depend on the amount of energy transferred to the electron. The Compton scattering equation used to describe the change in wavelength is

$$\lambda - \lambda' = \frac{h}{mc}(1 - \cos\theta) = \frac{2h}{mc}\sin^2(\frac{1}{2}\theta)$$

where λ is the incident photon wavelength and λ' is the scattered photon wavelength.

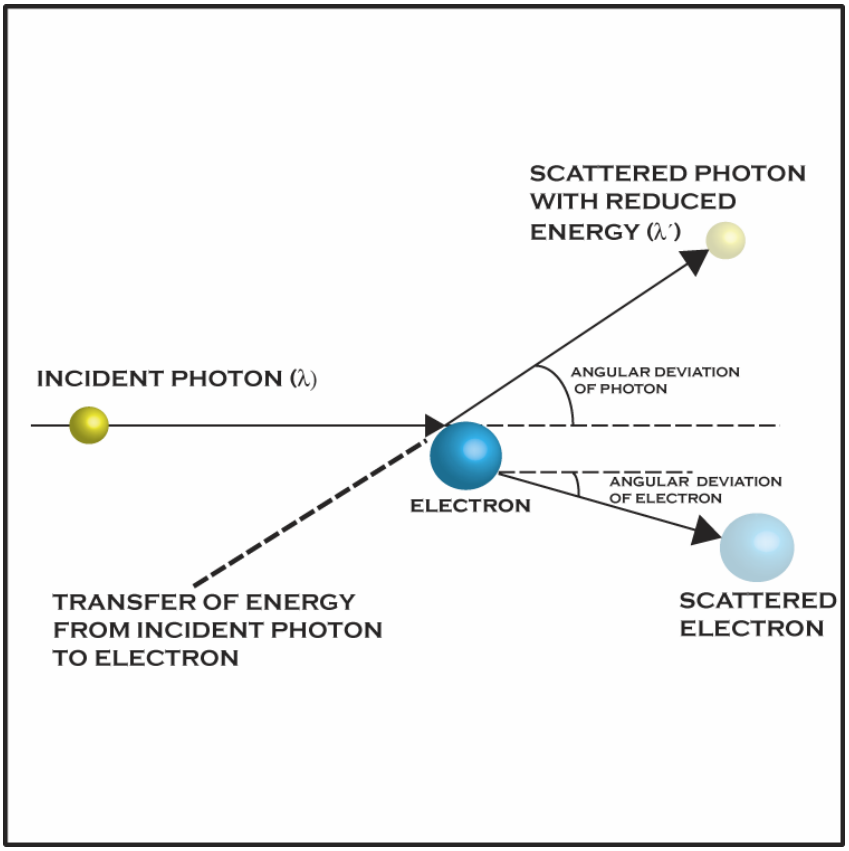

FIGURE 3.9: Compton scatter from a free electron

High energy x-ray photons typically transfer a small amount of energy, making the scattering angle small relative to the initial trajectory of the photon. Conversely, scattering of lower energy x-ray photons is more isotropic in nature. The problem in conventional radiography is that while the lower energy x-rays used in diagnostic imaging are scattered isotropically, those photons that are detected are forward directed. These scattered photons can have a

similar energy and direction when compared with the desired photons used to generate an image. The similarity in energy and direction makes their removal by anti-scatter grids and energy filters difficult. For this reason, Compton scattering can reduce resolution and contrast by blurring the resulting image. Ingenious methods have been used to reduce the impact of Compton scattering on radiography, but no methods in conventional x-ray imaging have been successful in completely eliminating this effect (Hendee and Ritenour 2002).

3.7 Energy Deposition, Dose, and Health Effects

The development and use of imaging systems that use ionizing radiation are both enabled and grounded by the electromagnetic radiation used to visualize the internal structure of an object or patient. Ionizing radiation is defined as radiation which has enough energy to cause atoms to lose electrons and become ions. X-ray imaging is the most commonly used ionizing imaging modality, but many other anatomical and functional imaging modalities utilize ionizing radiation to obtain diagnostic information. An unavoidable consequence of using ionizing radiation is the dose associated with its use, and an understanding of how dose is measured and the associated health effects are essential. As with other systems of measurement, the quantification of radiation exposure has evolved and changed producing numerous units and methods.

Dose is defined as the amount of radiation exposed to or absorbed by a subject or object. The *Roentgen*, named after the discoverer of x-rays Wilhelm Conrad Roentgen, is a unit of exposure use to measure the ionization produced in air by x-ray or gamma radiation. Determining the exposure in terms of Roentgens involves determining the sum of the electrical charges on all ions of one sign produced in air when all electrons liberated by photons in a volume element of air are completely stopped in air, divided by the mass of the

air in the volume element. One Roentgen (R) is defined as 2.58×10^{-4} Coulombs of charge produced by x-ray or gamma rays per kilogram of air. The Roentgen is also defined as the amount of x- and/or gamma radiation that produces a charge of 1 esu (2.08×10^{9} ion-pairs) in 1 cc of dry air at standard temperature and pressure. Use of the Roentgen is limited to measuring x and gamma radiation, and more importantly it is not a measure of absorbed dose. Its use is not common in medical imaging devices, but its use does persist because the measurement of air ionization is still widely used in other areas.

A more useful measurement of radiation for biological imaging applications takes into account the dose of radiation absorbed by a subject or object, which is expressed in *rad*. A rad is equal to 100 ergs ($1 \text{ erg} = 10^{-7}$ J) of energy absorbed by 1 gram of tissue. The internationally adopted unit of absorbed radiation is the *gray*, named for the English medical physicist L.H. Gray, and is equal to 100 rads. A rad or gray is not a measure of total energy, it is a measure of how much dose is absorbed per gram of tissue. In order to determine how much total energy was delivered, one must know the amount of tissue exposed. Both the rad and gray provide a measure of absorbed dose, but it is still just a measure of the amount of energy left behind in a tissue.

For medical imaging, a measure that takes into account the biological effect of the absorbed radiation is useful. The biological impact of absorbed ionizing radiation is in part determined by the type and energy of radiation absorbed. A measure of the biological effect can be calculated by multiplying the absorbed dose (either rad or gray) by a quality factor which is determined by the particular type of incident radiation. A quality factor of 1 is assigned to photons and electrons, neutrons range from 5-20 depending on the energy of the neutrons, and alpha particles (He^{2+}) are assigned a quality factor of 20.

EXAMPLES OF RADIATION QUALITY FACTORS	
TYPE OF RADIATION	QUALITY FACTOR (QF)
X-RAY	1
GAMMA	1
BETA PARTICLES	1
ALPHA PARTICLES	20

FIGURE 3.10: Radiation quality factors

For example, 1 gray of alpha particles will have a deleterious effect on biological tissue that is judged to be 20 times greater than 1 gray of x-rays. Multiplication of the absorbed dose and the appropriate quality factor produce a measure known as the equivalent dose. The unit of equivalent dose is rem (roentgen equivalent man) and the equation is expressed as

Equivalent Dose = Absorbed Dose x Quality Factor.

The modern unit sievert is typically used instead of rem, and is equal to 100 rem. For example, an equivalent dose of 300 rem is equal to 3 sievert (Hall 1978).

In addition to determining the effect particular types of radiation, the type of tissue being exposed also has an impact on the overall effect. Certain types of tissue are more sensitive to radiation than others, with some of the most sensitive being rapidly dividing cells such as hemopoietic stem cells, intestinal epithelium, and spermatogenic cells (Hall 1978).

RELATIVE SENSITIVITY	CELL/TISSUE TYPE
HIGH	HEMOPOIETIC STEM CELLS, SPERMATOGENIC CELLS, AND INTESTINAL EPITHELIA
MODERATELY HIGH	GASTROINTESTINAL AND EPIDERMAL EPITHELIA
MEDIUM	ENDOTHELIUM, CARTILAGE, AND BONE
MODERATELY LOW	HEPATIC, PANCREATIC AND ADRENAL EPITHELIUM, RENAL, MATURE CARTILAGE, AND BONE
LOW	MUSCLE, NEURONS, AND ERYTHROCYTES

FIGURE 3.11: Relative sensitivity of biological tissues to radiation

A term known as the effective dose is calculated by adding the product of the equivalent doses of the types of tissues irradiated and their weighting factor expressed as

$$\text{Effective Dose} = \sum_{i=1}^{n} (\text{Equivalent Dose x Tissue Weighting Factor}).$$

Biological systems rely on a hyper-complex system of molecules and structures to carry out the functions necessary for life. Ionizing radiation can disrupt cellular operations which can lead to a loss of function or death of the cell. Molecules in the body are united by chemical bonds and interact in a well defined sequence, often assisted by enzymes and other biological machinery. Energy released from ionization can break chemical bonds, potentially changing the shape and function of these molecules. The impact on the cell is dependent on which parts of the cell are disrupted and how many events take place in a given amount of time.

One of the most sensitive and critical components of the cell is its DNA (deoxyribonucleic acid), which is involved in cellular replication, transcription, and subsequent translation. If an ionization event takes place in the DNA leading to the ejection of an electron, an electrical charge can form in the DNA. Interactions that take place in this manner are called a *direct action*, in that the ionization event occurs directly in the DNA or from a neighboring molecule.

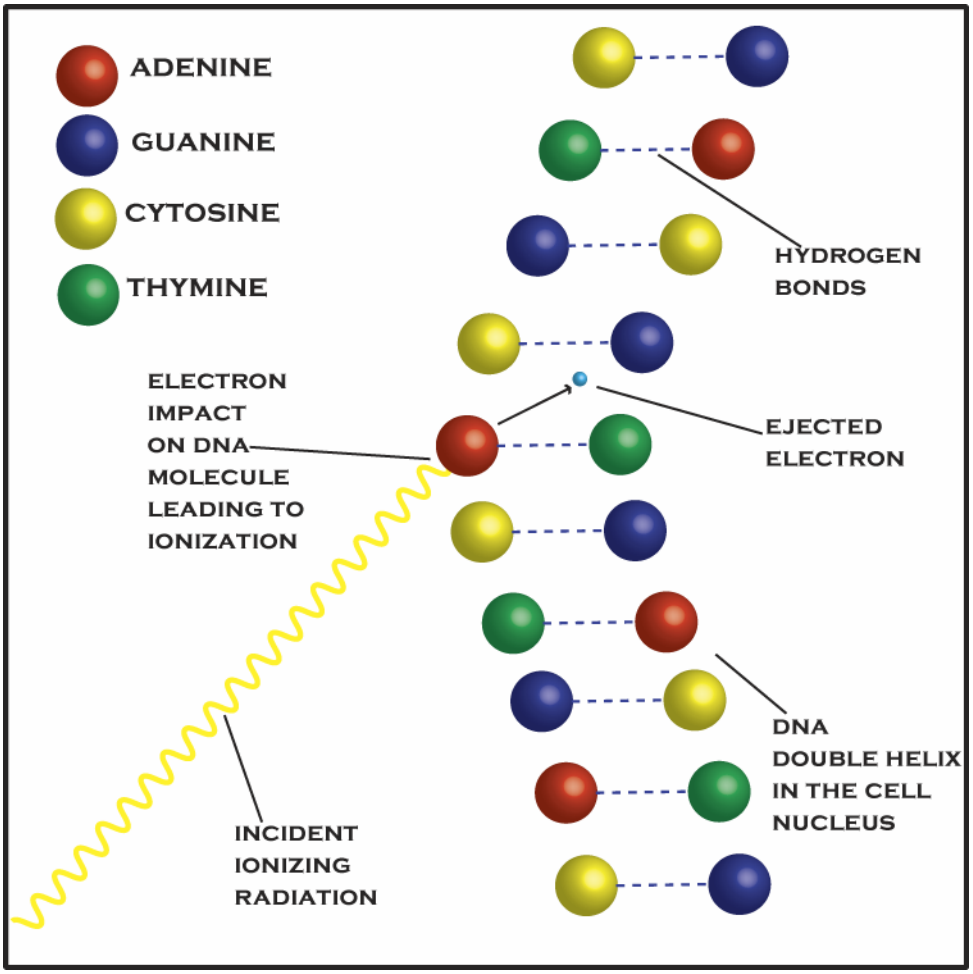

FIGURE 3.12: Generation of a free radical through direct action

Approximately 2/3 of free radical generation from x-rays is classified as an *indirect action*, occurring when an ejected electron strikes a water molecule. This ionizes the water molecule and can lead through a series of steps to the creation of a free radical (R·).

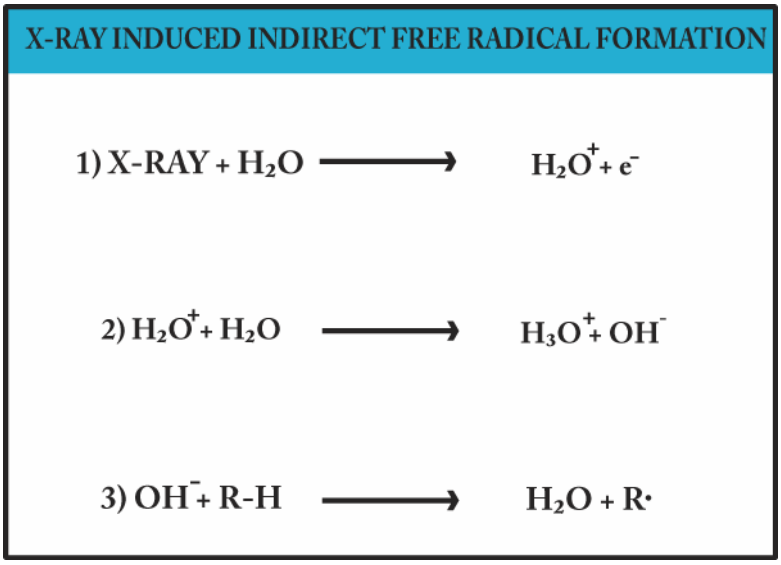

FIGURE 3.13: X-ray induced indirect free radical formation

Once a free radical is generated, it can react very strongly with other molecules to restore a stable electron configuration. If a free radical interacts with a DNA molecule, it can create an error that does nothing, causes a temporary dysfunction, or destabilizes the cell, leading to eventual cellular death (Grosch and Hopwood 1979).

Excessive radiation exposure can lead to cell death, which can be manifested in two basic forms. Ionization can disrupt cellular functions to the point where the cell can no longer sustain itself, leading to cell death. Mitotic inhibition can also occur, allowing the cell to function, but no longer replicate. Effects that have an impact on the cellular level can be scaled to the organ, system, or organism level. A dose of 100 gray to the entire body can lead to death within 24 to 48 hours. A whole body dose of 2.5 to 5 gray can produce death within several weeks. Localized radiation exposure to organs and other body parts can lead to focal cellular death and dysfunction, with the impact of damage determined in part by the sensitivity of the tissue type.

Cellular death is only one consequence of exposure to ionizing radiation, alteration of DNA can lead to errors in the DNA blueprint. The development of cancer is a possible outcome of DNA damage to somatic cells. Errors in the DNA can lead to defects in cellular regulation, which can lead to uncontrolled proliferation and the development of cancer. Induction of errors in the DNA of germ cells can lead to heritable defects that may not manifest themselves for generations (Whalen and Balter 1984).

Chapter 4: Overview of Current Mainstream Imaging Modalities Used for Breast Imaging

4.1 X-ray Imaging

X-ray imaging as is known today was born with the fortuitous and seminal observation by the German physicist Wilhelm Conrad Röntgen on the evening of November 8, 1895. Roentgen had been working on the phenomena associated with the passage of electric current through a vessel filled with gas at low pressure. These experiments had already been performed and studied by several other prominent physicists leading to the description of cathode rays. Röntgen had created a sealed tube and sealed it in a thick, black carton placed in a dark room. During this experiment, Röntgen noticed that a paper plate covered on one side with barium platinocyanide placed in the path of the rays fluoresced, even at a distance of two meters from the discharge tube. Realizing that there was an interaction occurring between the sealed tube and the plate, he placed objects of different thicknesses in the path of the rays and recorded the result. He noticed that the exposure of the plate was variable, and related to the thickness of the object. Being the daring and fearless scientist, he quickly made the transition to human testing and placed his wife's hand in the path of the beam and recorded the result. What was generated was the first radiograph, an image of the bony structure of his wife's hand along with an image of the ring she was wearing, and the penumbra of the soft tissue of her hand. Röntgen's later experiments showed that the new rays were created by the impact of cathode rays on an object. Since the exact

mechanism of their creation was unknown, Röntgen called them "X-rays". The name stuck, and his discovery led to a revolution in medicine and materials science. Röntgen was awarded the first Nobel Prize in Physics in 1901.

A major step towards efficient and practical radiographic imaging came from the American engineer and physical chemist William D. Coolidge with the invention of what is now referred to the Coolidge x-ray tube. In 1905, Coolidge was an engineer working for the General Electric Research Laboratory and was charged with replacing the carbon filaments in electric light bulbs of the day with a more durable element, tungsten. Coolidge was successful in this endeavor, and realized that he could apply his discoveries with the tungsten light bulb to another product manufactured by General Electric, x-ray tubes. X-ray generators of the day used residual gas molecules as an electron source, but Coolidge proposed using a heated tungsten as the electron source, which led to the use of significantly higher operating voltages. Coolidge created a "hot cathode" tube, which was able to produce higher energy x-rays and was far more stable than previous x-ray systems. While there have been advancements and refinements made to the first Coolidge cathode, the fundamental design of current x-ray tubes is essentially the same.

X-ray sources for the current generation of radiographic imaging systems use a design based on Coolidge's "hot cathode" tube. An electron beam is generated at the cathode, which as in Coolidge's day, is usually made of tungsten with a current applied at the cathode. A high voltage is applied across the cathode and anode, which creates a high potential difference across the vacuum of the x-ray tube. Even at high voltages, this is not enough to cause the release of electrons from the anode. In conventional x-ray systems, electrons are thermonically ejected by heating the anode. The high heat capacity and high melting point of

tungsten makes it an ideal choice for use as a cathode. An electrostatic focusing cup surrounds the point of ejection, which helps to focus the electron stream towards the anode.

Electrons being emitted from the cathode are focused across the vacuum of the x-ray tube to the anode, with the velocity across the gap determined by the voltage applied across the circuit. The energy spectrum and general output characteristics of an x-ray tube are primarily determined by the anode material and configuration. Selecting the proper anode material is based heavily on the application, specifically on what modality and what structure is to be imaged.

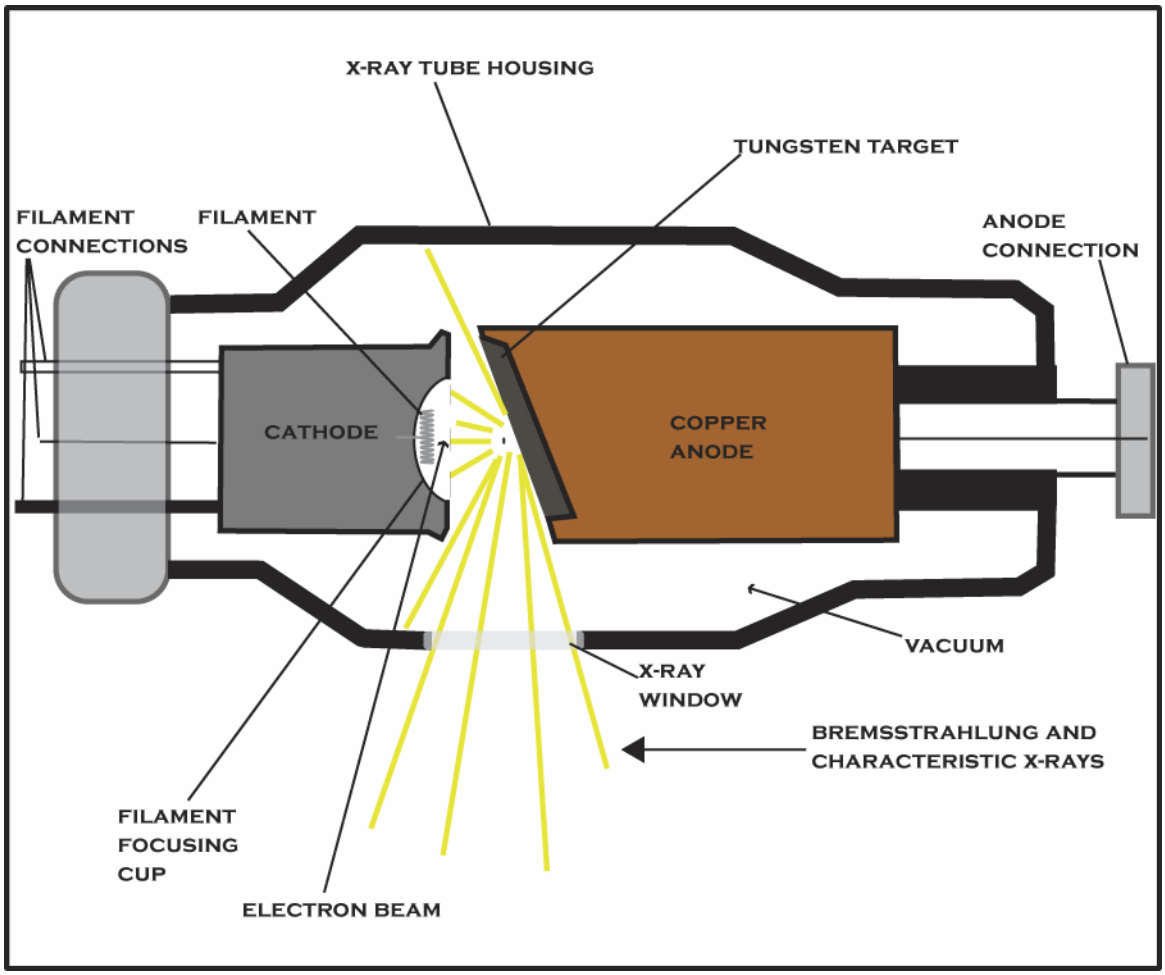

FIGURE 4.1: Example x-ray tube with a stationary anode

For mammography, the most common anode material is molybdenum, but rhodium is also used (Bushberg et al. 2002). Molybdenum's K_α of 18 keV provides the appropriate spectrum for imaging soft tissue. For mammography systems, the anode is often stationary and mounted in a copper block to reduce heat. A major engineering problem is the generation of heat in the anode by the focused electron beam. X-ray tubes that have a stationary anode are more prone to heating because the primary means of heat removal is the surrounding copper anode, even with its high thermal conductance. Advancements in x-ray tube development have led to the use of a rotating anode, which rotates so that the electron beam from the cathode does not impact the same area on the anode.

The primary acquisition detection method for radiography, until the relatively recent advent of digital detectors, is x-ray film. The film used for x-ray imaging is designed as either a single-emulsion film, with the emulsion on one side, or as a double-emulsion film, which has an emulsion layer on both sides of the film. With both designs, the emulsion is applied to a transparent base layer which is approximately 0.2 mm thick. The photon stopping power of a single-emulsion film is less than a double-emulsion film, but it does have the advantage of being able to resolve fine details, making it the preferred choice for applications such as laser printing and mammography. Emulsions are composed of silver halide granules, typically silver bromide, that are evenly distributed in a gelatin matrix. A protective layer, known as a T coat, is applied to the emulsion to protect it from external abrasion and scratches.

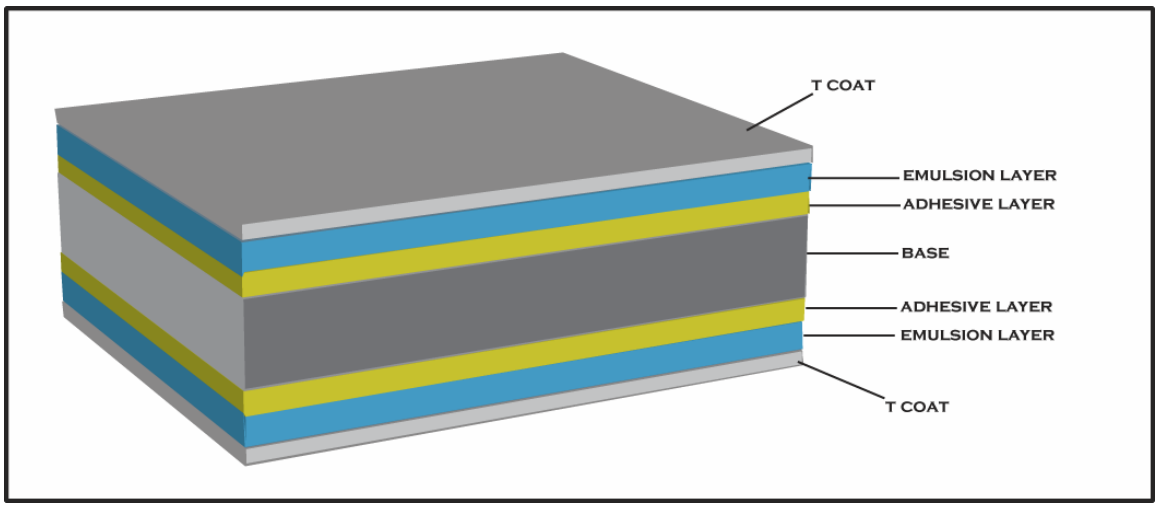

FIGURE 4.2: Cross section of a double-emulsion film.

When incident radiation, in this case an x-ray, strikes one of the silver halide granules, an electron is released. These electrons become trapped in regions of the crystal lattice of the silver bromide granules known as sensitivity centers. The presence of electrons in the lattice can react with the Ag^{+} ions of the disassociated silver halide, leading to a reduction event and the deposition of metallic silver primarily across the silver bromide granules. A developing solution is added that facilitates additional silver deposition at the sensitivity centers. Sodium thiosulfate or ammonium thiosulfate is used to remove the granules, thus ending the development process. The amount of blackening in a region of the film is dependent on the amount of free silver deposited in the region, which is directly related to the amount of x-rays incident in that region (Hendee and Ritenour 2002).

The ability of film to stop photons is limited, where only 2% to 6% of the total energy in the incident beam is absorbed by the film emulsion. In order for an image to be developed with film alone, large numbers of photons have to pass through the film, increasing the radiation dose absorbed the object or patient. Intensifying screens were developed to increase the efficiency of radiography, significantly increasing photon detection efficiency. The

stopping power of intensifying screens is much greater than film, allowing for image creation with a lower overall photon count. Photons that strike the active layer of the intensifying layer are absorbed, causing visible light to be emitted. The wavelength of light emitted is determined by the composition of the active layer, and should correspond closely with the spectral sensitivity of the film used. Benefits of using intensifying screens include: reduced exposure time and decreased motion unsharpness in the image, reduced tube voltage and improved contrast in the image, reduced heat production in the x-ray tube, reduced tube current allowing for smaller focal spots, and reduced patient radiation exposure (Hendee and Ritenour 2002). The primary disadvantage of using intensifying screens is the divergence of light from the point of emission on the screen to the film, which can lead to blurring of the final image. However, the benefits of intensifying screens generally outweigh the small loss in resolution, with film alone being used only in situations where extremely fine detail is required.

4.2 Ultrasound Imaging

Ultrasound imaging has found a niche in a myriad of medical disciplines and has dramatically extended the ability to diagnose and evaluate internal structures that is both non-ionizing and safe. Ultrasound is defined as a mechanical disturbance that moves as a pressure wave through a medium, and the interaction of this pressure wave with the internal structures of an object can generate an image based on how much of the wave is reflected. Given the importance of ultrasound in breast imaging, an understanding of the physics and applications of the modality is essential.

French physicists Pierre and Jacques Curie discovered the piezoelectric effect in 1880, which is the generation of a voltage between opposite sides of a piezoelectric crystal as a

result of pressure or twisting. The reverse is also true, where the application of a voltage at the opposite sides of a piezoelectric crystal produces a deformation in the crystal. This seminal discovery provided the theory necessary to enable others to build upon and eventually find practical applications. With the general theory established, finding materials that had the appropriate piezoelectric properties under normal environmental conditions was a challenge. The French physicist Paul Langevin was successful in using this theory to develop piezoelectric materials as senders and receivers of high-frequency mechanical disturbances, leading to the use of ultrasound for the detection of submarines during World War I. Development continued on what eventually became known as SONAR (sound navigation and ranging) during World War II. The first industrial uses of ultrasound were proposed by Soviet Physicist Sokolov in 1928, through his suggestion that ultrasound could be used to detect hidden flaws in material. The first medical uses of ultrasound in the 1930s were limited to therapeutic applications for cancer treatments and physical therapy for various ailments, but a synergistic collaboration between physicians and engineers in the 1940s would introduce the diagnostic applications of ultrasound (Hendee and Ritenour 2002).

The basic theory of ultrasound imaging relates to the passage of a pressure wave through a medium, which in this case is a patient. An ultrasound transducer is used to generate the pressure wave, which is created by applying a voltage to a piezoelectric crystal and rapidly changing the polarity. The application of a voltage to a piezoelectric crystal will cause a deformation in the crystal leading to contraction or expansion, depending on the polarity (Hendee and Ritenour 2002). A typical ultrasound transducer has an array of elements that generate an ultrasound wave and a detector to receive reflected waves used to generate an

image. The strength of the reflection is determined in part by the angle at which the ultrasound wave strikes a reflecting interface, known as the angle of incidence. Maximum reflection of the beam producing the strongest echo occurs at 90 degrees, when the reflector is perpendicular to the ultrasound beam. The strength of the reflection, or echo, decreases as the angle of incidence decreases. At high angles of incidence, the ultrasound wave is deflected away from the crystal and no echo is recorded. The shape of the transducer and the geometry of the transducer elements is application dependent and each has benefits depending on the application. Two common transducer designs are a curved array, where the transducer elements are arranged along a curved surface, and a linear array in which the elements are fired in a certain way to generate a radial distribution of ultrasound beams. For the breast imaging application, linear transducers are typically used with an output frequency of 7.5 to 10 MHz (or higher) (Zwiebel and Sohaey 1998).

The emission sequence of the transducer elements can be used to steer and focus the beam, which are characteristics of a phased array transducer. A phased array transducer has a series of independent ultrasound emitters, which can be fired in a specific sequence to manipulate the resulting wavefront. If the array elements are fired simultaneously, the wavefront will move linearly away from the crystal. If each adjacent crystal element is fired in a staggered fashion one after the next, then each wavelet is out of phase with the adjacent wavelet. This causes the wavefront to deviate, and changing the element firing delay can cause a minor or major angular deviation in the wavefront as desired for the intended application. The same general method can be used to focus the ultrasound beam, by firing the outside transducer elements before the middle and center elements. This feature is operator controlled and permits the focal zone to be placed in specific areas of interest (Zwiebel and Sohaey 1998).

Ultrasound can also be used to measure the change in frequency that occurs when an ultrasound wave is reflected from moving objects, known as the Doppler effect. The general equation for the Doppler shift in frequency $\Delta\nu$ is

$$\Delta\nu = 2\nu_o\left(\frac{\nu}{c}\right)\cos\theta$$

where ν_o is the frequency of the ultrasound from the source, ν is the velocity of the object being measured, c is the velocity of ultrasound in the medium, and θ is the angle between the ultrasound beam and the direction of motion of the object. If object or objects in the path of the beam are moving away from the transducer, then the reflected waves will have a longer wavelength and lower frequency than the incident waves. Conversely, if reflecting object or objects are moving towards the transducer, then the reflected wave will have a shorter wavelength and a higher frequency than the incident waves. One can use this information to determine velocity, which is useful in a variety of medical applications, from determining vascular flow to measuring blood flow and distribution in the heart (Hendee and Ritenour 2002).

Tissues in the body are composed mostly of water, and molecules in a fluid medium are in continuous random motion. If no external force is applied to the medium, then the distribution of the molecules will be uniform. The pressure wave from an ultrasound transducer will apply a force to the medium, resulting in an area of increased pressure at that location. This area of increased pressure is known as a zone of compression, and the pressure wave continues to move forward through the medium. The oscillation of the piezoelectric crystal in the transducer can also create an area of reduced pressure, known as a zone of rarefraction. Rapid oscillations in the transducer create alternating zones of compression and

rarefraction, which creates a longitudinal wave. A zone of compression and the adjacent zone of rarefraction are considered to be one cycle of an ultrasound wave. The distance covered by the cycle is known as the wavelength, and the number of cycles per unit time is defined as the frequency of the wave measured in hertz, kilohertz, or megahertz (Hendee and Ritenour 2002).

As ultrasound waves pass through a medium, energy can be removed from the beam through the processes of absorption, reflection, scattering, refraction, diffraction, interference, and divergence. Attenuation is a general term referring to any interaction that removes energy from the ultrasound beam. Absorption of ultrasound waves occurs when a portion of the energy is converted to other forms of energy, which could be heating of the medium or an increase in overall molecular entropy. Reflection is defined as an orderly deflection of all or part of the beam, and less orderly changes in direction are referred to as scatter (Hendee and Ritenour 2002).

How a sound beam behaves when it interacts with a structure depends on the size of the obstacle in comparison with the wavelength of the sound. If the object encountered is large when compared to the wavelength of the sound and relatively smooth, the beam will retain its integrity when it changes direction. In this case, part of the ultrasound beam may be reflected while the remainder is transmitted as a beam of reduced intensity. If the object in the path of the beam is approximately the same size or smaller than the wavelength of the ultrasound, the object will scatter energy in various directions. This is referred to as specular scatter, and this type of interaction allows for the visualization of the boundaries between organs. Ultrasound energy may return to the receiver after nonspecular scatter, but this usually requires several

scatter events. Nonspecular scatter facilitates visualization of tissue parenchyma (Hendee and Ritenour 2002).

The use of ultrasound for the detection of breast lesions was first reported in 1951 by Wild and Neil (Wild and Neil 1951). They reported the use of ultrasound in differentiating between breast cysts and sold masses, which continues to be one of the most important uses of ultrasound in breast imaging. Attempts were made in the early 1980s to use ultrasound to increase the cancer detection rate in radiographically dense breasts, but it became apparent that both the false-positive and false-negative rates for ultrasound diagnosis were too high to be of general benefit. Studies have shown that up to 45% of breast masses cannot be identified with ultrasound, and microcalcifications found at the earliest stages of disease can not be seen with ultrasound. The use of ultrasound for screening was subsequently abandoned, and its use is currently restricted to the assessment of mass lesions detected with mammography or physical examination (Zwiebel and Sohaey 1998).

The structural features of breast tissue have characteristic signatures on ultrasound, which is used for image interpretation and diagnosis. Certain features, such as Cooper ligaments, are strongly echogenic and are easily seen on ultrasound. Cooper ligaments can mimic the appearance of breast cancer because they are highly attenuating and may cast acoustic shadows. Adipose tissue in the breast is hypoechoic, and glandular tissue in the breast is medium in echogenicity. Differences in these normal structural features as well as lesions generate ultrasound contrast (Zwiebel and Sohaey 1998).

Breast cysts, which occur most frequently between the ages of 35 and 50 years, are the most common palpable breast masses. Current ultrasound systems can detect cysts as small as 2 mm. Classic ultrasound features of cysts that confirm benignity are the following: (1) an

imperceptible wall, (2) a smooth inner surface, (3) anechoic contents, and (4) a strong backwall (far wall) echo or enhanced through-transmission of ultrasound (Zwiebel and Sohaey 1998). Diagnostically, the most common use of ultrasound is to differentiate between cysts and solid lesions detected mammographically. In this case, ultrasound is used to prove that a lesion thought to be a cyst is indeed a cyst. If a lesion is thought to be a cancer mammographically, biopsy is an obligatory step making further ultrasound analysis unnecessary. Studies have shown that ultrasound is 96% to 100% accurate for differentiating between solid masses in the breast (Zwiebel and Sohaey 1998).

If a palpable mass if found in a woman less than 30 years of age, the mass is very likely to be benign based on the incidence of breast cancer in this demographic. Concerns in regards to radiation exposure in this age group make mammography an undesirable first option. Ultrasound can be used to determine if a lesion is a benign cyst or if it is solid, which would warrant further investigation. If a lesion is found to be solid, a single-view mammogram can be obtained to determine if suspicious microcalcifications are present. Both the mammogram and ultrasound information are used to determine whether the patient should undergo a biopsy for a more definitive evaluation. Ultrasound is useful in patients with suspected breast inflammation in determining whether a frank abscess is present which requires drainage. For invasive procedures, ultrasound is used to guide aspiration or core biopsy of mammographically identified lesions as well as masses that are palpable but can not be visualized using mammography (Zwiebel and Sohaey 1998).

The ubiquitous presence of ultrasound in breast imaging clearly demonstrates the effectiveness and importance of this imaging modality. Unique features and characteristics based on the physics of the physical properties of ultrasound extend a radiologists diagnostic

ability when compared to mammography alone. However, ultrasound is but one tool used to supplement or extend the diagnostic capabilities of mammography.

4.3 Magnetic Resonance Imaging (MRI)

Magnetic Resonance Imaging (MRI) has evolved spectacularly over the past two decades and has become a ubiquitous modality in the field of radiology. Current MRI systems and their development can be traced back to a similar technology, nuclear magnetic resonance (NMR). The first successful NMR experiment was conducted in 1946 by American scientists Felix Bloch and Edward Purcell. Felix Bloch of Stanford University and Edward Purcell of Harvard University independently discovered that when certain nuclei were placed in a magnetic field they absorbed energy in the radiofrequency range of the electromagnetic spectrum, and re-emitted this energy when the nuclei returned to their original state. Sir Joseph Larmor had previously demonstrated that the angular frequencies of precession are proportional to the strength of the magnetic field, known as the Larmor relationship. The seminal observations made by Bloch and Purcell led to the development of NMR spectroscopy, for which they were awarded the Nobel Prize for Physics in 1952. The next major step towards the development of MRI came with a March 1973 Nature paper by Paul Lauterbur, a Chemistry Professor at the State University of New York at Stony Brook, entitled "Image formation by induced local interaction; examples employing magnetic resonance." In this paper, Lauterbur described a new and novel imaging technique, which he called zeugmatography, which involved the joining together of a weak gradient magnetic field with a stronger main magnetic field. In Lauterbur's experiments, the combination of these allowed for the spatial localization of two test tubes in water. Although NMR spectroscopy and MRI share common base principles, the addition of a gradient added a

second dimension of spatial orientation that later became the foundation of MRI. Another essential step in obtaining MR images was discovered by Dr. Peter Mansfield, who demonstrated that the use of gradients in the magnetic field produced signals that could rapidly and effectively be analyzed and transformed into an image (Hendee and Ritenour 2002). Dr. Paul Lauterbur shared the 2003 Nobel Prize in Physiology and Medicine with Sir Peter Mansfield "for their discoveries concerning magnetic resonance imaging".

The basic theory of MRI deals with the behavior of nuclear magnetic moments by using the hydrogen nucleus as a model. The hydrogen nucleus consists of a single proton, which behaves as a small magnet with a magnetic moment that has both magnitude and direction. Hydrogen containing materials, such as the human body, have a proton distribution such that the magnetic moments of the individual nuclei are oriented in random directions.

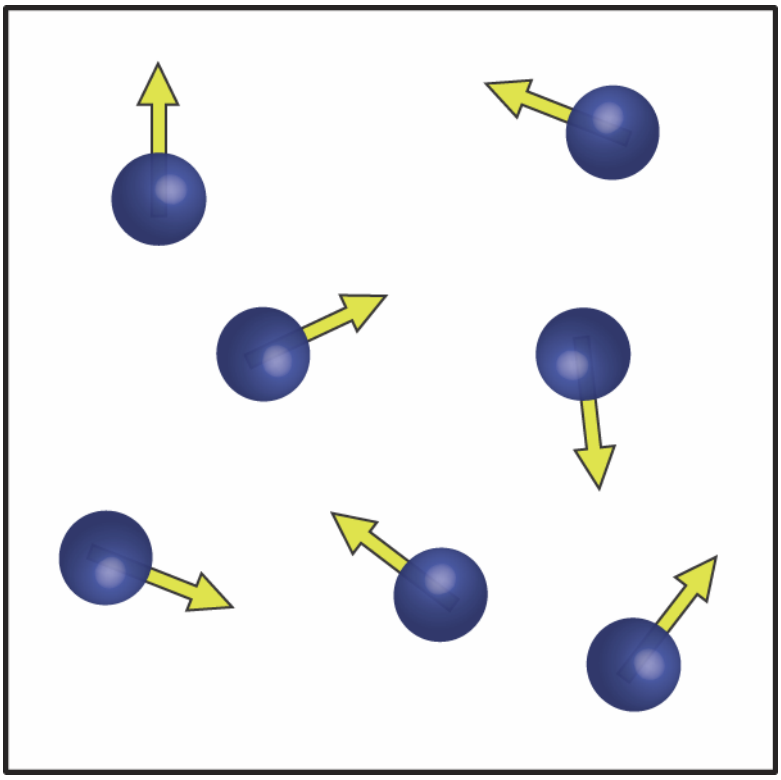

FIGURE 4.3: Protons with randomly distributed magnetic moments

The application of a strong magnetic field to an object or patient causes the magnetic moments of the nuclei to align in the direction of the magnetic field, either in a parallel or anti-parallel state.

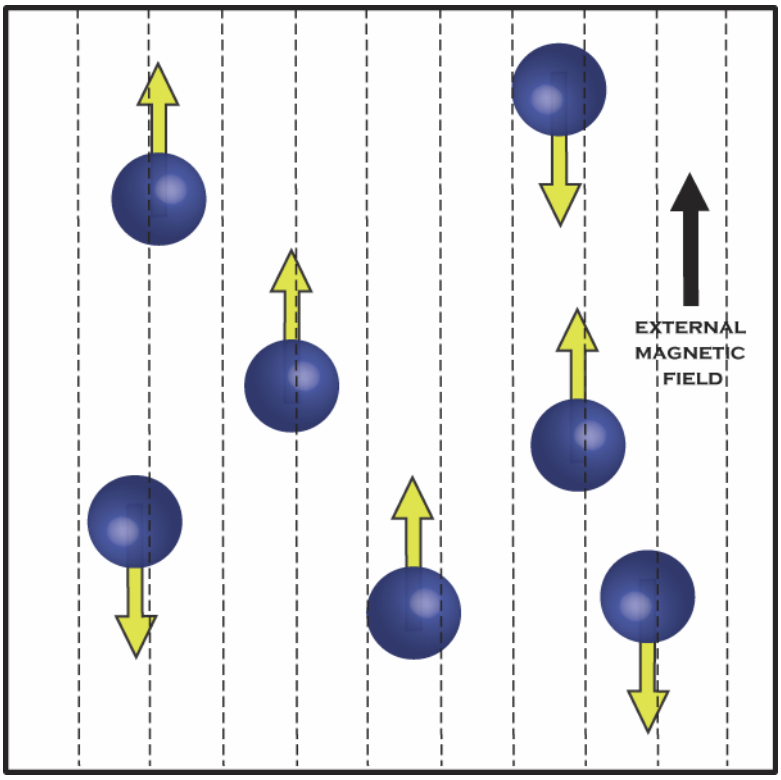

FIGURE 4.4: Protons with an external magnetic field applied, having both parallel and anti-parallel alignments

To put the applied field in perspective, the magnetic field of the Earth is approximately 0.5 gauss, whereas the field applied by a typical MR system is in excess of 20,000 gauss (Hendee and Ritenour 2002).

Another fundamental principle of MRI is the precession of the magnetic moment in the field. Precession is a type of motion that is distinct from rotation, defined as the spinning of an object about its axis. The Larmor equation may be used to predict the precession of a proton in a magnetic field and is defined as

$$f = \gamma \mathrm{B}$$

where f is the frequency of precession of a proton in units of megahertz, γ is the gyromagnetic ratio in megahertz per tesla, and B is the strength of the magnetic field in Tesla. For MRI systems with field strengths ranging from 0.1 to 3.0 tesla, the corresponding precessional frequencies range from 4.3 to 129 MHz for hydrogen nuclei (Hendee and Ritenour 2002).

If the protons in a sample are analyzed in a macroscopic scale, a bulk magnetization model can be applied for explanation. For a collection of spins, the individual magnetic moments can be considered to be additive in that they point in the same direction, or cancel each other out by pointing in random directions. Before the application of an external radio frequency, the transverse components tend to cancel each other out because the protons are rotating out of phase. The net magnetization vector lies along the direction of the applied magnetic field B_o, and is called the equilibrium magnetization M_o. Before the application of a radio frequency pulse, the Z component of magnetization, M_z, is equal to the equilibrium magnetization, M_o.

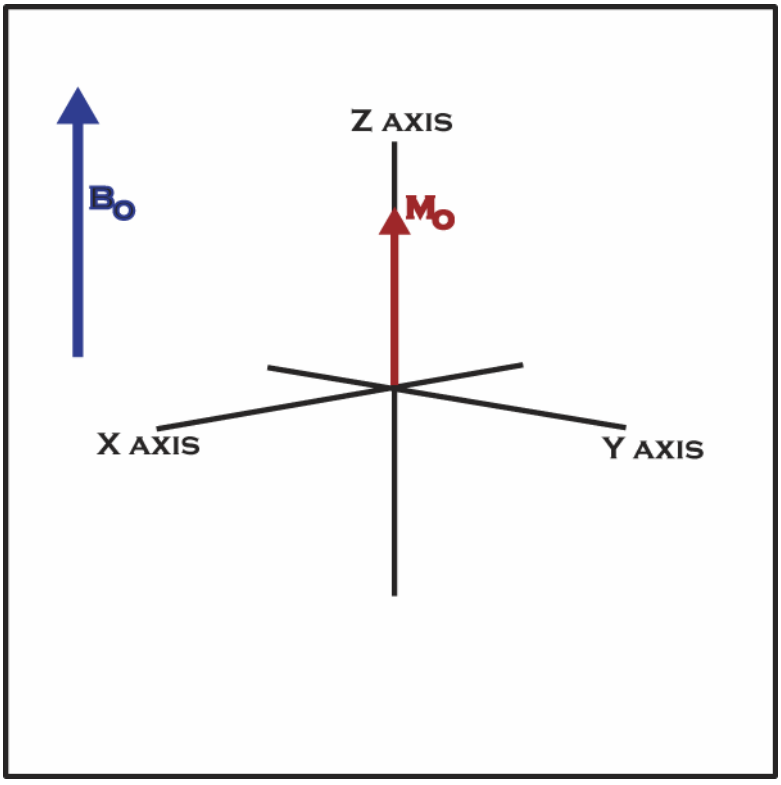

FIGURE 4.5: Net magnetization of protons in external magnetic field

The random nature of the magnetic moments makes the bulk magnetization zero in the transverse plane, M_{XY}. Applying an RF pulse with the appropriate resonance frequency for protons brings the protons into phase, creating the transverse component of the magnetic field (Hendee and Ritenour 2002).

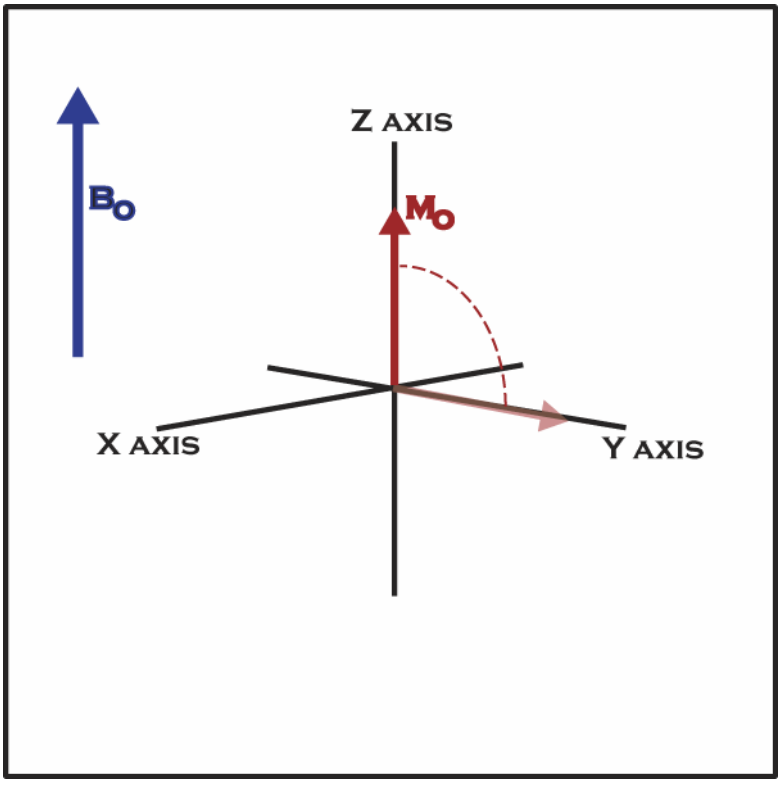

FIGURE 4.6: Change in net magnetization after introduction of the RF pulse

The resonance that occurs between the protons and the RF pulse provides the energy necessary to flip a limited number of the parallel magnetic moments into the transverse plane. Since this is a higher energy state, the alignment will immediately begin to decay back to the lower energy state as soon as the external RF pulse is removed. The rate at which the magnetic moments return to the parallel state is dependent on several factors, all of which lead to a net release of energy to the surroundings and a return to the original alignment with the static magnetic field. The time constant describing how M_Z returns to its equilibrium value is called the longitudinal or spin-lattice relaxation time, but most often referred to as T1. T1 is used to define the amount of time required for M_Z to return to 63% of its initial value.

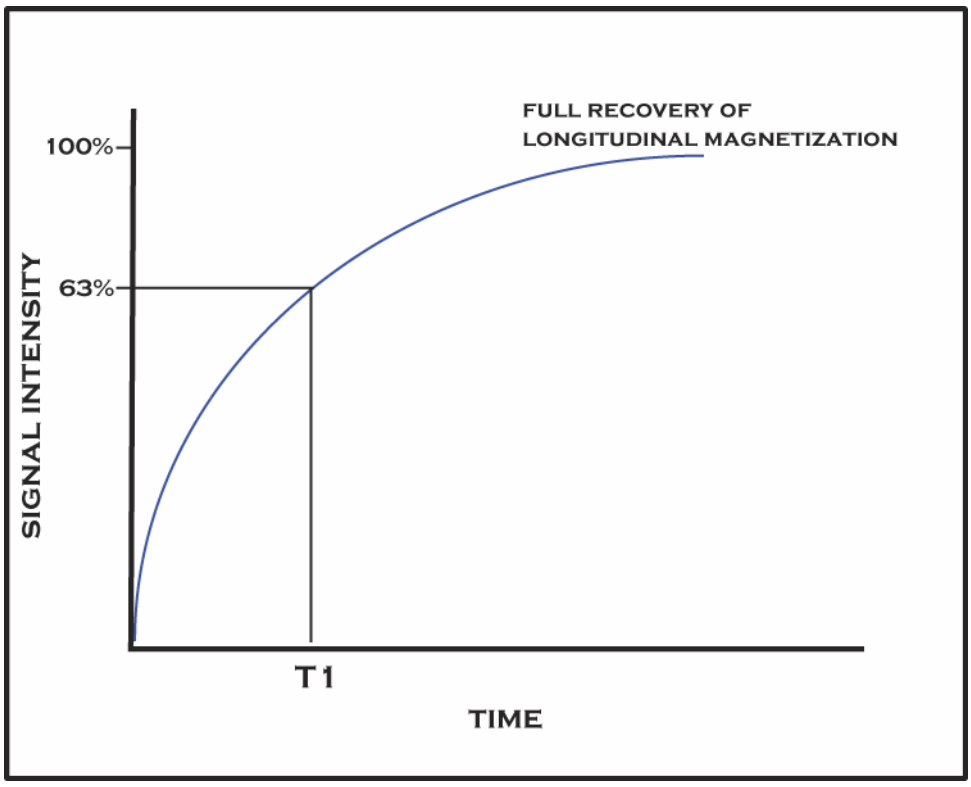

FIGURE 4.7: T1 Longitudinal relaxation curve

The equation governing the behavior of this process is

$$M_z = M_o \left(1 - e^{-t/T1}\right)$$

where t is the time in seconds after the radio frequency pulse is removed.

For biological specimens, the local environment of the protons has a significant impact on how quickly energy is released; for example, consider protons in cerebrospinal fluid and protons in fat. Energy was added to the system for the protons to be rotated into the transverse plane, and the rate at which that energy is dissipated will determine how quickly they return to their initial configuration rotating about the Z axis. Protons in a liquid, such as CSF, will interact less than those which are in a solid, such as fat. The more the molecules bump into one another, the faster they will lose energy. This in turn will make the recovery time for CSF much longer than fat, giving CSF a higher T1 value than fat. Because of these

differences, an image can be created known as a T1-weighted image. The key is to acquire the image at a time where the differences are significant, which is in part determined by the imaging application. If an image is acquired too late in the sequence, the values will have approached equilibrium and there will be little to no contrast.

Biological tissues contain a wide range of substances and materials that make an exact T1 measurement difficult, but different tissue structures have aggregate differences in T1 values that are used to generate image contrast. For a wide range of tissues, the T1 for hydrogen can be approximated by the equation

$$T1 = \alpha f^{\beta}$$

where f is the resonance frequency in hertz, and the parameters α and β vary with the tissue type over a range of $\alpha = 0.5$ to 10 and $\beta = 0.2$ to 0.4 (Hendee and Ritenour 2002).

Protons which have been flipped into the transverse plane by the introduction of a radio frequency pulse will rotate in phase, but they will gradually begin to dephase because each of the rotating protons in the transverse plane will experience a slightly different magnetic field and rotate it its own Larmor frequency. The more time that goes by, the greater the phase difference, resulting in a reduction in the transverse magnetization vector. Additionally, interactions of the protons in their local environment will influence the rate of dephasing. The time constant that describes the return to equilibrium of the transverse magnetization, M_{XY}, is called the spin-spin relaxation time, or T2. T2 is also defined as the time required for the magnetization in the transverse plane to decrease to 37% of its value after the radio frequency pulse is removed.

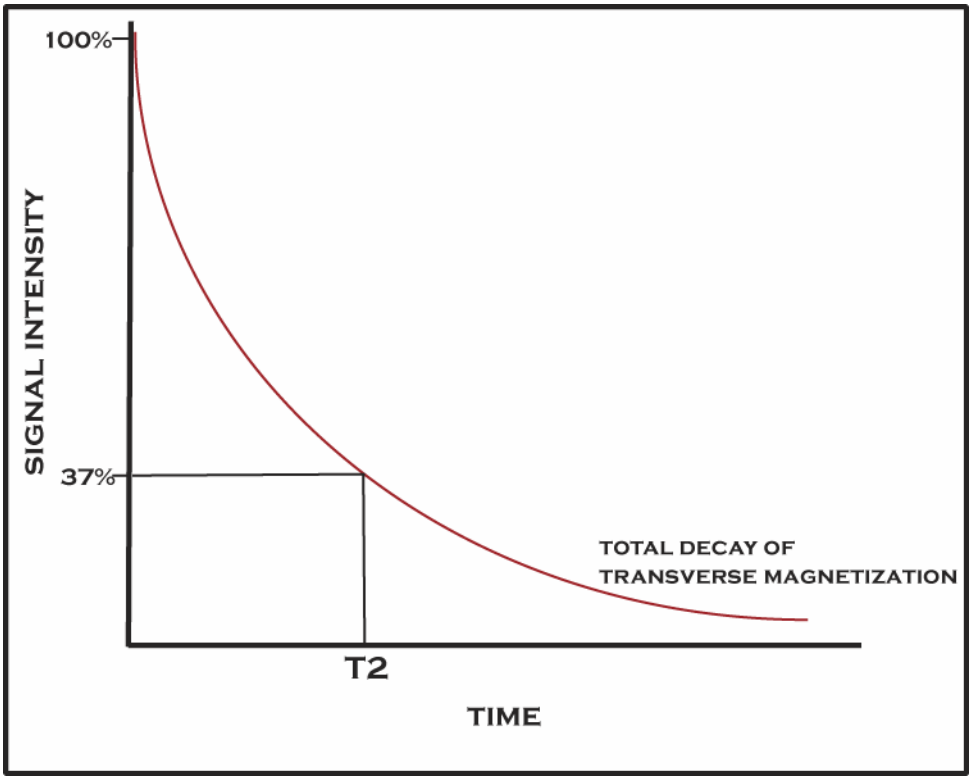

FIGURE 4.8: T2 transverse magnetization decay curve

This process is defined by the equation

$$M_{XY} = M_{XY_O} e^{-t/T2}$$

where t is the time in seconds after the radio frequency pulse is removed. In biological tissues, the local environment of the protons can be used to generate contrast. The value of T2 will vary depending on material composition, in that different tissues can cause the protons to dephase at a faster rate. For example, consider again protons in cereberospinal fluid (CSF) and fat. The molecular density of CSF, a liquid, is lower than that in fat, a solid. Higher molecular densities will increase the probability of interaction between adjacent protons, increasing the rate of dephasing. Since T2 is defined as the time required for the magnetization of the transverse plane to be reduced to 37% of its initial value, fat will have a lower T2 value than CSF. Differences between these substances, as well as other materials in

the body, are used to generate a T2 weighted image. As with T1 weighted images, it is essential to acquire the images at a time where the differences in T2 values are greatest.

Since both processes are independent and act to reduce the overall signal, the equations defining them can be combined to give the overall signal reduction due to both factors defined as

$$S = S_0 e^{-t/T1} e^{-t/T2}.$$

While both processes lead to the decay of signal, the effect of T2 dominates, especially at lengthy time intervals. For example, if the decay of T1 is long when compared to the reduction in T2, as is the case with many tissues of interest in MRI, then T1 effects will be eclipsed by the effects of T2 relaxation. The differences of T1 and T2 in different tissues and fluids can be enhanced by using special RF pulsing techniques. Contrast in MRI is in part determined by the differences in the relaxation parameters T1 and T2, and the nuclear spin density (Hendee and Ritenour 2002). There are numerous other methods used to generate contrast in MRI, and considerable efforts are being made to further improve and add new pulse sequences and methods.

Contrast agents are used to enhance visualization of tissue, especially in the case of visualizing breast tumors. For MRI, one of the most commonly used contrast agents is gadolinium combined with the chelating agent diethylenetriamine (Gd-DTPA). The electron configuration of gadolinium is what makes it an excellent contrast agent for MRI, since is has seven unpaired electrons. Ferromagnetic compounds, such as Fe_2O_3 and Fe_3O_4 are also used as contrast agents because of their ability to selectively decrease T2 and cause a decrease in the MR signal. This effect is known as negative contrast, and can also be achieved through the introduction of perfluorochemicals, which are molecules in which most or all of the

hydrogen component has been replaced by fluorine. In proton specific imaging, perfluorochemicals will not exhibit an MR signal because they do not contain hydrogen, thus producing negative contrast (Hendee and Ritenour 2002).

The design of MR systems varies depending on the intended application, with the field strength for imaging systems varying from millitesla up to 10 tesla for some research systems. Most systems for clinical imaging range from 0.1 to 3.0 tesla, but "it is not clear whether there is an optimum field strength for certain imaging situations" (Hendee and Ritenour 2002). There are numerous problems that arise with increasing field strength, including maintaining magnetic field homogeneity, increased RF heating, and chemical shift artifacts (Hendee and Ritenour 2002).

4.4 Computed Tomography (CT)

Conventional planar x-ray imaging is a highly useful imaging method, but there are several limitations of this modality that fueled the development of tomographic imaging and eventually the revolutionary addition of computed tomography. Conventional planar x-ray imaging is limited in that subtle differences of less than approximately 5 percent in x-ray attenuation are not visible. It is important to remember that conventional x-ray imaging is a projection of three-dimensional anatomic information onto a two dimensional image receptor. An x-ray traveling along a linear path in an object can encounter a variety of objects with differing attenuation coefficients as it traverses the object and encounters the detector. Mathematically, the attenuation of the x-ray is a line integral integrated over a defined linear path. This is problematic when attempting to visualize complicated three-dimensional structures, where the region of interest is obscured by other objects in the path of the x-ray. Another limiting factor is that conventional image receptors, such as film, intensifying

screens, and fluoroscopic screens are unable to resolve small differences (less than 2%) in the intensity of incident radiation. Conventional large-area x-ray sources are also a limiting factor, in that the wide diverging x-ray beam can undergo numerous scattering events from the point of emission to the detector, leading to increasing blurring and decreased overall image quality. Considerable efforts in the first half of the twentieth century were made to overcome these limitations in conventional x-ray imaging, leading to the meteoric rise of computed tomography (Hendee and Ritenour 2002).

The conceptual origins of computed tomography can be traced to the Austrian mathematician Radon, who demonstrated the mathematics of image reconstruction from projections in 1917. Radon demonstrated that an object can be reconstructed from an infinite set of projections, a theory he developed not for imaging but as a method for mapping gravitational fields. It did not take long for several pioneering radiologists to capitalize on Radon's method and apply it to x-ray imaging. They theorized that if an x-ray tube and film are translated in opposite directions about a fulcrum, then the longitudinal projection of only that focal plane will remain in focus. This eventually led to noncomputed tomography, a technique that remained predominant for nearly 40 years. The information obtained from noncomputed tomography rekindled investigations into image reconstruction from projections, which had remained relatively untouched since Radon's initial publication.

William Olendorf, an American neurologist, is credited as being one of the first to recognize the potential of image reconstruction from projections for medical imaging in 1961. He constructed a prototype tomographic scanner equipped with an ^{131}I source and opposed scintillation detector, with the object to be imaged rotating between them. Emission tomographic scanning was pioneered in 1963 by David Kuhl and Roy Edwards, first adapted

to nuclear medicine applications such as brain imaging. Advancements in tomographic imaging continued, but a fortuitous advance was made by Allan M. Cormack while working on corrections for dose inhomogeneities in radiation therapy patients. Cormack had rediscovered and extended Radon's mathematical solution of image reconstruction from projections, and constructed a prototype tomographic scanner using a ^{60}C source and opposed detector with the object rotating between them. He used this experimental setup to test his theories and eventually incorporated computer processing of the transmitted data. Godfrey H. Hounsfield, working at Electro-Musical Instruments (EMI), Ltd., independently concluded that a two-dimensional map of attenuation coefficients in the body could be reconstructed with an accuracy of better than 1 percent from a finite number of transmission projection measurements (Sanger and Kramer 1995). Hounsfield also constructed a prototype tomographic scanner using an ^{241}Am source and opposed scintillation detector, later replacing the ^{241}Am source with a higher intensity x-ray source to increase x-ray flux and decrease image acquisition time. Hounsfield's employer, EMI, Ltd., developed Hounsfield's ideas into the first clinical transmission CT, developed specifically for brain imaging. This device was installed at the Atkinson Morley Hospital in Wimbledon, England in 1971, and the utility of this device became readily apparent and was an immediate success. Eight years later, Houndsfield and Cormack were awarded the 1979 Nobel Prize in Physiology and Medicine for the pioneering work in reconstruction tomography (Sanger and Kramer 1995).

Reconstruction algorithms for CT image reconstruction have developed into four types: simple backprojection, filtered backprojection, Fourier transform, and series expansion. The method of simple backprojection divides the x-ray transmission path through an object into equally spaced elements, with the assumption that each element contributes equally to the

total attenuation along the x-ray path. Summing of the attenuation values for each element over all x-ray paths that intersect the element at different angular orientations can be used to generate a final summed attenuation coefficient for each element. This process can be used for all of the other elements in an anatomic section, forming a composite image of attenuation coefficients. While a viable reconstruction method, the simple backprojection method is limited in that it produces blurred images of sharp features in an object (Hendee and Ritenour 2002).

The most popular reconstruction method for CT is the filtered backprojection algorithm, which is also called the convolution method. The filtered backprojection method uses a one-dimensional integral equation for the reconstruction of a two-dimensional image. Blurring associated with the simple backprojection method is reduced by the use of a deblurring function (filter) that is convolved with the x-ray transmission data to remove most of the blurring before the image data is backprojected. In addition to reducing image blurring, the filtered backprojection method allows for image reconstruction while x-ray transmission data is still being acquired (Hendee and Ritenour 2002). This can dramatically decrease image acquisition time, which is especially important in the newest generations of high speed CT scanners.

The Fourier transform method separates the x-ray attenuation pattern at each angular orientation into frequency components of various amplitudes. These frequency components can be combined to form a spatially correct image in the frequency space, which can then be reconstructed using an inverse Fourier transform process. This method is commonly used in magnetic resonance imaging, but it is not a common reconstruction method for CT systems (Hendee and Ritenour 2002).

Series expansion, also known as iterative reconstruction, x-ray attenuation data at one angular orientation are divided into equally spaced elements along several rays. The data at one angular orientation is compared to similar data at different angular orientations, and the differences in x-ray attenuation at the two orientations are added equally to the appropriate elements. This process can be repeated for all angular orientations, using a decreased fraction of the attenuation difference added each time to facilitate convergence of the reconstruction data. A significant limiting factor of series expansion techniques is the fact that all of the x-ray attenuation data must be available before the reconstruction process can begin, thus increasing the total time for image reconstruction. This inherent limitation has prevented the utilization of series expansion techniques in commercial CT scanners (Hendee and Ritenour 2002).

CT systems have advanced significantly since the first EMI system, evolving through multiple generations. However, there are basic features common to the majority of CT systems currently on the market. In regards to the x-ray source, both stationary- and rotating-anode x-ray tubes have been utilized in CT systems. Stationary-anode x-ray sources generally have a focal spot on the order of 2 x 16 mm, but these systems have a limited output requiring increased scan times. Scan times for stationary-anode x-ray sources are typically about 5 ms for each measurement of x-ray transmission, a scan time long enough to limit the application of this type of x-ray source. Rotating-anode x-ray tubes can have rotational velocities 10,000 rpm and greater, allowing for higher flux and scanning times as low as 2 to 3 milliseconds. An increased photon output with an increased ability to distribute heat generated by the electron beam on the anode makes rotating-anode x-ray sources the preferred source for CT scanners (Hendee and Ritenour 2002).

Collimation of the x-ray beam is a critical design component, confining the x-ray beam to a thickness of a few millimeters, which defines the slice thickness. Using a collimator also has the added benefit of reducing scattered photons, reducing the fraction of scattered radiation transmitted to less than 1 percent of the primary beam intensity. CT units employ two types of collimators, a source collimator in the beam path before it encounters the patient to shape the x-ray beam and reduce patient dose, and a postpatient collimator used to control the slice thickness (Hendee and Ritenour 2002).

X-ray detectors used for CT scanning typically fall into two general categories, gas filled and solid-state. Gas-filled gas ionization detectors use pressurized xenon gas at pressures up to 25 atm to improve detection efficiency. Solid-state detectors include those made of NaI (Tl), CaF, and CsI scintillation crystals and ceramic materials composed of bismuth germinate (BGO) and cadmium tungstate [$CdWO_4$]. High-pressure xenon detectors have a detection efficiency of approximately 50 percent, compared with an 80 percent detection efficiency for solid-state detectors. The demanding nature of CT reconstruction algorithms puts considerable demands on the stability of the detector, with instability producing ring-shaped artifacts in the image (Hendee and Ritenour 2002).

Presentation of the data that has been acquired and reconstructed via an appropriate reconstruction algorithm requires the use of a display system. Measurement and calculation of the attenuation coefficients in an object or patient is a direct measurement, but a standardized presentation system was developed to allow comparison between different CT systems. The final numbers computed by a reconstruction algorithm are not the exact attenuation values, rather they are integers termed CT numbers, or Hounsfield units, that are related to the attenuation coefficients. CT units generally range from -1000 for air to +1000

for bone, with a calibration value of 0 for water. Making the value for water 0 allows for easy calibration of different CT systems, and any drift over time can be corrected. The mathematical relationship used to determine the CT number is

$$CT\ Number = 1000\left(\frac{\mu - \mu_w}{\mu_w}\right)$$

where μ is the calculated attenuation coefficient and μ_w is the measured attenuation value for water.

4.5 Single Photon Emission Computed Tomography (SPECT) And Scintimammography

All of the imaging modalities previously described are used to generate anatomic images or a patient or object, but they do not provide any functional information that can be used to characterize a potential lesion. Single Photon Emission Computed Tomography (SPECT) and scintimammography are different in that the source of the electromagnetic radiation used for image creation comes from a radiolabeled tracer injected into the patient, not from an external transmission source. By using a selective radiolabeled compound, planar and CT images can be created based on the distribution of the radiolabel, which is heavily influenced by the underlying physiological and potentially pathological processes. Creation and selection of a radiolabeled compound is application dependent, designed to concentrate in certain areas in the body based on metabolism and physiology. Common examples of radiolabeled tracers used for SPECT imaging are thallium-201 (^{201}Tl), technetium-99m(^{99m}Tc), and iodine-123 (^{123}I) (Galt and Faber 2004).

The primary image properties used to characterize SPECT imaging are the same as for the other imaging modalities, resolution, contrast, and noise. Resolution in SPECT is a measure of how close two point sources of activity can be visualized and distinguished in the resulting

image. Blurring and divergence in the emitted photon is unavoidable, making two point sources blur together if they are too close together. Resolution for scintigraphic images is obtained by using a point source and analyzing the resulting curve, which would appear as a sharp single spike if there were no blurring. Actual measurements have a profile that is modeled based on a Gaussian curve, with the resolution of the system determined by the full-width half-maximum (FWHM) of the curve (Galt and Faber 2004).

Contrast for scintigraphic images, which includes SPECT, is often defined as the measure of counts in the target compared with the intensity in a background region. A simple mathematical relationship for calculating contrast in SPECT imaging is

$$Contrast = (C_0 - C_b)/C_b$$

where C_0 is the number of counts in the organ or target and C_b is the background photon count. Transmission-based modalities can generate a high intensity of incident photons, the major limiting factor being the patient absorbed dose. While dose is still a concern in SPECT, the specific targeting of the radionuclide and the counts detected are of paramount importance for image formation. Objects that emit a high number of photons in relation to the background will have good contrast, while objects that emit a low number of counts or have little difference from the background will have low contrast (Galt and Faber 2004).

Developers of emission based modalities are constantly trying to reduce noise, which can be highly problematic if the count statistics are too low. For scintigraphic images, random counting statistics is the primary generator of noise. The value for each pixel in a planar scintigram is assigned a number that is generated based on the number of photons detected in a small area of the crystal. Random scatter can appear as speckle in nuclear medicine images, which is especially noticeable in background regions. Noise effects in tomographic images is

difficult to quantify because each voxel is created from projections of that point from many different angles. Research and clinical use have shown that SPECT images are superior to planar scintigraphic images in contrast but resolution is reduced during the process of reconstruction. Contrast gains are due to the fact that each image represents a slice through the patient created from multiple projections, allowing for much of the background to be reduced or eliminated. Systems used for SPECT have a primary difficulty in creating a camera capable of multi-angle image acquisition that is also as close as possible to the target organ or region. Since resolution in SPECT decreases with distance, the size and distance of the gamma camera from a patient becomes a major limiting factor.

Given the physics of emission-based imaging, physicists, engineers, and physicians have endeavored to create systems capable of achieving the desired diagnostic task. Significant efforts have been made in regards to the scintillation camera, which are typically composed of a collimator, a sodium iodide (NaI) crystal, a photomultiplier tube, pulse height analyzers, and spatial positioning circuitry. One of the most widely used scintillation camera designs was developed by Hal Anger at the University of California at Berkeley in the late 1950s and early 1960s. This camera design, also known as the Anger camera, is based on the interaction with a gamma photon with a NaI crystal and subsequently using electronics to measure the position and intensity of the interaction to generate an image. Gamma rays emitted from a radioactive tracer pass through a collimator and strike the crystal creating a short burst of visible light, known as a scintiallation event. The light emitted is converted into electrical signals via the photomultiplier tubes, with the brightness of the scintillation being proportional to the energy of the photons which is measured by the pulse height analyzer. Determination of the position of the scintillation event occurring on the crystal has evolved

and improved over the years, moving from analog summation and correction circuitry to computer-based digital systems with positioning, summation and correction software. The evolution from analog positioning circuitry to computer based digital systems offers may advantages, but both serve the essential function of accurately determining the position of the photon interaction on the crystal as accurately as possible (Galt and Faber 2004).

Collimators are commonly used in radiography, but collimator design in SPECT is of critical importance and has a profound effect on image quality and application. SPECT collimators are composed of an array of long, narrow parallel holes that are used to significantly reduce or exclude all photons except those which are traveling parallel to the direction of the hole. The characteristics of the detector, specifically resolution and sensitivity, of a parallel hole collimator are determined by the shape, length, and size of the holes. For example, lengthening the collimator septa and decreasing the size of the hole will increase the probability that photons being detected are those traveling parallel to the hole. The inherent penalty to increasing the specificity of the collimator is a reduction in photon count, which can reduce the sensitivity of the system and potentially make noise an overriding problem. In general, the sensitivity and resolution of a collimator are inversely related where a very high sensitivity collimator has low resolution, and a very high resolution collimator has low sensitivity (Galt and Faber 2004).

There are three general types of collimators for SPECT imaging, low-energy all-purpose (LEAP), general purpose (GAP), and high resolution (HRES) collimators. LEAP and GAP collimators have relatively short, wide holes that allow for more photons emitted from the source object to pass through to the detector. HRES collimators have long, narrow holes, which allows for high resolution and a reduced background. Use of these systems has shown

that images with better resolution do not need as many counts to achieve the same image quality, making HRES collimators generally preferred to LEAP collimators. The energy of photons used in nuclear medicine (70-300 keV) requires the use of dense metals to be able to attenuate high energy photons that are not traveling parallel to the hole. Metals suitable for the task are limited, making lead, sliver, gold, and tungsten the most appropriate choices. Most collimators are made of lead, but certain applications call for highly expensive tungsten collimators (Galt and Faber 2004).

Applications of SPECT for breast imaging and breast cancer center around determining appropriate therapy through accurate staging of initial disease and re-staging after therapy. At present, no anatomic imaging modality can accurately assess for lymph node metastases. Uncertainty present in the anatomic imaging modalities necessitates axillary lymph node dissections for prognosis and for determining the need for adjuvant chemotherapy and radiation therapy. SPECT imaging is being investigated as a means to add functional information to that obtained by the anatomic imaging modalities and potentially reduce the need for axillary lymph nose dissections (Galt and Faber 2004).

The most common radiopharmaceutical used in scintimammography is Technetium (Tc)-99m hexakis-isobutylnitrile (MIBI), but Tl 201 chloride and Tc-99m ethylene-bis [bis(2-ethoxyethyl)] phosphine (tetrofosmin) are also used in SPECT imaging of the breast.

4.6 Positron Emission Tomography (PET)

Another functional imaging modality of increasing diagnostic importance is Positron Emission Tomography (PET), which is a powerful method for imaging simple chemical or physiological processes in the body. PET is used in conjunction with anatomic imaging modalities to add a characterization of simple molecular processes that are taking place in

normal or diseased tissues in the body. Metabolic and biologic events associated with disease always precede any anatomic indicators of an illness. PET adds critical physiologic data that can be used to detect diseases, such as cancer, and add significant information to information obtained from x-ray, CT, or MRI.

PET imaging utilizes positron-emitting forms of simple elements (^{11}C, ^{13}N, ^{15}O, and ^{18}F), that can be generated and combined with biologically useful molecules. These molecules can be used to study the most basic and fundamental biological interactions, including those interactions involved in cancer. Applications in oncology, cardiology, and brain imaging have expanded the use of this unique and powerful modality and increasing its availability. To date, over 3000 distinct chemical compounds have been radiolabeled with PET tracers specifically designed for imaging molecular processes (Christian 2004).

Paul Adrien Maurice Dirac theorized the existence of the positron (positively charged electron) in 1927, which he described as an antiparticle of the negatron (negatively charged electron). The existence of the position was later demonstrated experimentally by Carl D. Anderson in 1932, for which he and Victor Hess were awarded the 1936 Nobel Prize for Physics. Proton-rich nuclei decay by either electron capture or through positron emission, with the radionuclides used for PET imaging primarily undergoing the positron emission decay pathway (Christian 2004).

Positrons emitted from the nucleus normally travel a short distance, generally a distance of several millimeters. As the positron travels this short distance, adjacent atoms are ionized causing the positron to lose energy and slow down. The positron can then pair with an electron, with the two spiraling toward each other for a tiny fraction of a second and forming a two-particle atom known as a positronium. The interaction of the two quickly leads to the

annihilation of the antiparticle positron/electron pair. This annihilation event is associated with the complete conversion of the mass of each particle into energy according to Einstein's equation

$$E = mc^2.$$

The mass of the positron and electron are exactly the same, leading to the release of 511 keV from each particle in the form of gamma rays. A pair of 511 keV gamma rays are released, with the two gamma rays being emitted almost exactly 180 degrees apart.

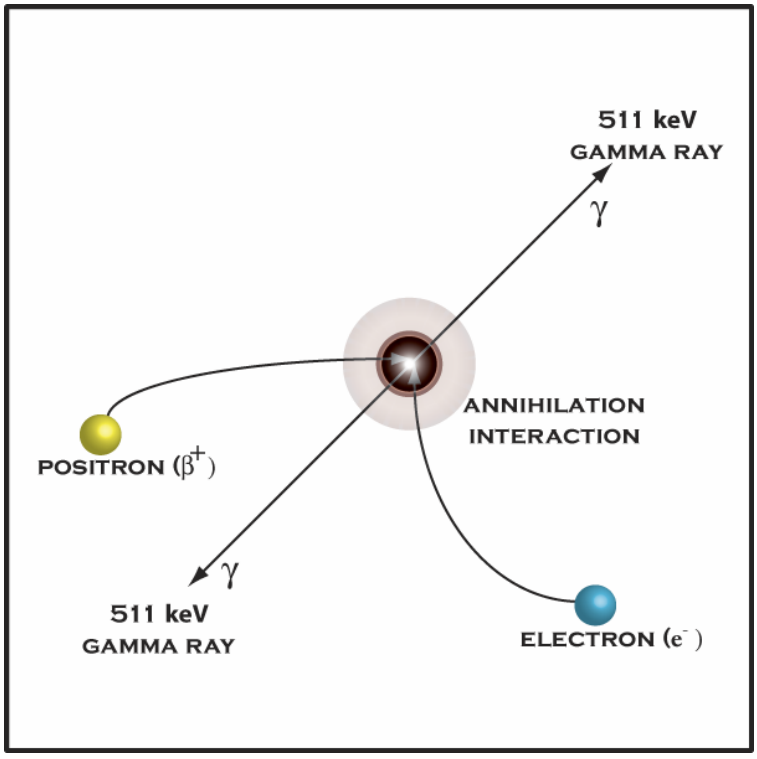

FIGURE 4.9: Annihilation interaction from positron-electron collision

Events such as the motion of the particles at the time of annihilation can cause minor variations in the angle of emission, on the order of +/- 0.5 degrees. The predictable emission of gamma rays with a known energy provides the elements needed for image creation (Christian 2004).

PET imaging is based on the detection of the 511 keV gamma rays, which in theory these gamma rays are detected almost simultaneously using scintillation detectors positioned on opposite sides of the patient. The line calculated between the two detection events is known as the line of response (LOR), and is used to calculate the point of emission. Since the gamma rays released from annihilation event reach the detector in a very short period of time, one can be reasonably sure that two gamma rays arriving at approximately the same time on opposite sides of the detector are from the same annihilation event. This process in known as coincidence detection, and a coincidence window is used to measure the arrival time interval of the electrical pulses generated by the incident gamma photons on the detector.

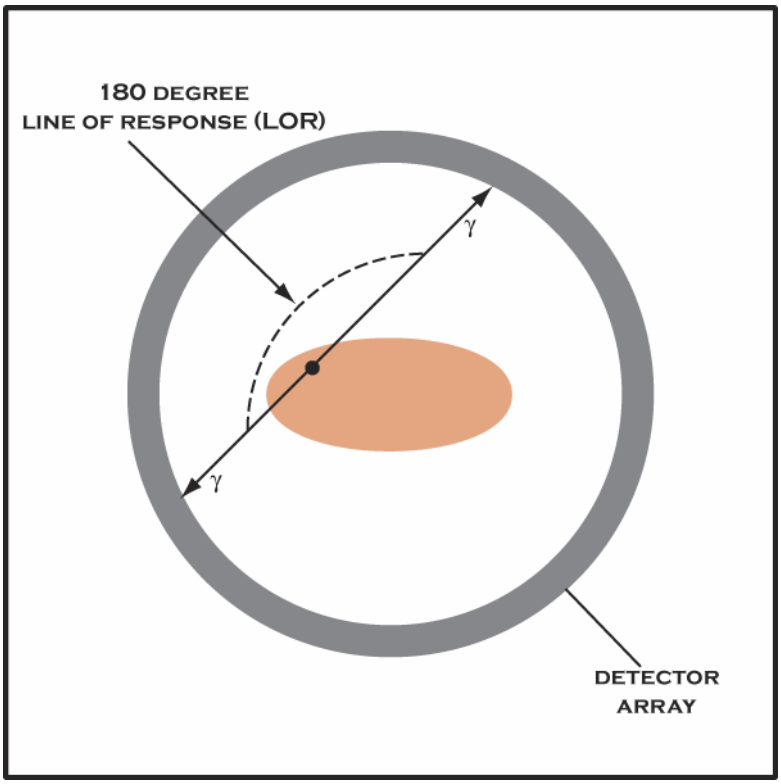

FIGURE 4.10: Coincidence detection in PET imaging

Electromagnetic radiation travels at 30 cm/nanosecond, making a coincidence window between 6 and 12 nanoseconds sufficient for detection. A true coincidence annihilation event is defined as a pair of annihilation gamma rays striking two elements of the detector at the same time. This is the ideal situation, but the physics of PET imaging is more complicated and there are other factors that can complicate the process. If two atoms decay at approximately the same time, photons from two different annihilation events may be detected within the same timing window. This is known as a random event, and it generates a false line of response. It is impossible to avoid having multiple atoms decaying at the same time, but methods have been developed to correct for these false events. Without correction these random events can lead to significant reductions in contrast of true hot lesions, which may cause some tumors to be missed. Another contributor to image quality degradation in PET imaging comes from the scatter of gamma rays between their emission point and the detector. Gamma rays that undergo a Compton scattering event will lose energy, and detectors can be created with an energy resolution capable of rejecting photons that fall outside of the appropriate energy window. Methods using appropriate emission and transmission slices for the size and activity distribution within the patient are used to make complex scatter corrections (Christian 2004).

The spatial resolution of a PET scanner is primarily determined by the size of the crystals in the detector and their separation, with typical values ranging between 3 to 5 mm. Detectors used in PET systems have a large number of crystals and hundreds of independently operating photomultiplier tubes, making the count rate capability significantly higher than those associated with scintillation cameras.

Radiotracers used for PET have to be created using small linear accelerators or cyclotrons, which contributes significantly to the cost associated with PET. Since positrons are generated by proton-rich nuclei, manufacturing positron-emitting radiopharmaceuiticals is accomplished by adding protons to the nucleus. This is performed in linear accelerators or cyclotrons by providing a source of positively charged protons or deuterons with energies sufficient to create these nuclei. Unfortunately the half-lives of these radiopharmacuiticals are small, examples being 75 sec for ^{82}Rb, 2.1 min for ^{15}O, 9 min for ^{13}N, 20 min for ^{11}C, and 110 min for ^{18}F. With such short half-lives, these nuclei must be created at or near the site used for imaging. The relatively long half life of ^{18}F makes it the most logical candidate for imaging, and this compound is readily incorporated into the glucose molecule, forming ^{18}F-flurodeoxyglucose. Currently, ^{18}F-flurodeoxyglucose is the only ^{18}F label compound that is approved by the FDA for general distribution and is the radiopharmacutical commonly used in oncology studies (Christian 2004).

Chapter 5: Screen-Film and Digital Mammography

5.1 Historical Overview of Mammography Systems

The introduction of x-ray imaging for the purpose of breast imaging occurred in 1913 by the German surgeon Albert Salomon. Dr. Salomon used mastectomy specimens to demonstrate the utility of radiography in revealing the spread of tumor to the axillary lymph nodes and also first demonstrated the radiographic differences between the margins of infiltrating versus circumscribed carcinoma. Dr. Stafford L.Warren, a radiologist at Rochester Memorial Hospital, Rochester, New York, first reported the use of a stereoscopic technique for in vivo mammography in 1930. Warren used fine-grain Kodak film (Eastman Kodak, Rochester, NY), dual fine-grain intensifying screens, a moving grid to diminish the effect of scattered radiation in the image. Images were acquired at 60 kV(p), 70-mA, with a 25-inch target-film distance, and an exposure time of 2.5 seconds (Gold 1992).

Breast radiography was independently reported in 1931 by Walter Vogel in Leipzig and Paul Seabold in the United States, which included the differentiation of benign disease from carcinoma. As the potential application of radiography spread through the medical community, further investigations were made into the radiographic appearance of normal and malignant disease. Jacob Gershon-Cohen and Albert Strickler reported the range of normal radiographic appearances as a function of age and menstrual status in 1938, and Cohen went on to correlate the breast lesions he saw with the gross and microscopic findings. The

renowned pathologist Helen Ingleby used whole-breast histologic sections to perform extensive correlations between the radiographic appearance and histology (Gold 1992).

The association between microcalcifications and breast cancer was first demonstrated in 1949 by Raoul Leborgne, who analyzed a series of breast tissues and reported visible microcalcifications present in 30% of the tissues with breast cancer. Leborgne made other key contributions to breast imaging, including an emphasis on careful technique and positioning and was the first to recognize the importance of breast compression for improving image quality and visualization of internal structures (Gold 1992).

Investigators had demonstrated the potential utility of radiography for breast imaging, but technological development and reproducibility were lacking, generating moderate interest from the medical community. In 1960, Robert L. Egan described a high milliamperage-low kilovoltage mammographic technique using high resolution industrial film. The technique and positioning Egan used were easily reproduced, obtaining excellent results imaging the breasts of his first 1000 patients. Scientific evidence demonstrating the usefulness of mammography led to the sponsoring of a conference in 1963 by the Cancer Control Program of the US Public Health Service at the MD Anderson Hospital in Houston, Texas. The results of a nationwide study of mammography were presented showing that proper imaging techniques had been learned by other radiologists, producing mammograms of acceptable quality. In addition, there was sufficient evidence to show that mammography was effective in differentiating between benign and malignant lesions, and most importantly, that mammography could be used to screen for cancer in asymptomatic women (Gold 1992). With the evidence of effectiveness in place and a consensus among policymakers of the utility of mammography, the American College of Radiology undertook the responsibility of

training radiologists and technologists the skills necessary to acquire and interpret mammograms and set up a Committee on Mammography (Gold 1992).

The evolution of the hardware used for mammography was slow, beginning with what was essentially a tripod supporting a modified x-ray camera. A major step forward came in 1966 through the work of Charles Gros in cooperation with the French company CGR (Compagnie Gènèrale de Radiologie), developing the first dedicated mammography x-ray unit. This unit was called the Senographe, French for "picture of the breast", and used a molybdenum target with a 0.7 mm focal spot. From a technical perspective, the Senographe significantly increased contrast between parenchyma, fat and calcifications. A compression device was incorporated into the system, which decreased scattered radiation and increased structural visualization by decreasing the overlap of structures in the path of the x-ray (Gold 1992).

In 1972, the DuPont Company introduced a revolutionary image receptor for mammography, which employed a high-resolution intensifying screen and a single-emulsion x-ray film held within a vacuum cassette. This led to shorter exposure times, reduced motion unsharpness due to patient motion, and facilitated rapid automatic processing of the images. Development continued over the 1970's and 1980's, with efforts directed towards improvements in image quality and reduced dose to patients including breast compression, x-ray spectrum, screen-film systems, radiographic grids, magnification, automatic exposure control, film processing, and quality control (Hendee 1995). Digital mammography systems were developed and introduced in the late 1990s with the intended objective of eliminating some of the inherent limitations of screen-film systems and facilitating a wide range of novel storage, display, and analysis methods.

5.2 Clinical Trials and Evidence for Use

Few areas in medicine are as politically and socially charged as the use and effectiveness of mammography. "Since the late 1980s, there has been broad agreement, with few dissenters, that mammographic screening significantly and substantially reduced mortality from breast cancer" (Tabar et al. 2003). Large-scale screening trials have been used to determine the effectiveness of screening mammography, but these trials are expensive and take many years to decades to reach a conclusion. A large number of patients in the study arm have to be screened, but if randomization has been carried out before consent, attendance for screening may be too low in practice (de Koning 2003). Another problem with these trials is defining mammography, since the technology involved in x-ray breast imaging is evolving rapidly. The long time-frame of clinical trials in general has a disadvantage in that newer techniques may have evolve over the course of a study, urging investigators to change the screening protocol and therefore possibly weakening the final results of the trial (de Koning 2003). In addition to the financial cost associated with mammography to both patients and the health care system in general, the emotional burden associated with false positives, unnecessary biopsies, and radiation exposure are also of great importance. To date, the best means for determining policy and recommendations regarding the utilization of mammography is based on large-scale, randomized clinical trials.

The first large-scale clinical trial to demonstrate the efficacy of mammography was a trial sponsored by the Health Insurance Plan (HIP) in New York, followed by the Two-County study in Sweden (Freedman, Petitti and Robins 2004). Since these trials set the tone for mammography use in much of the world, an understanding of the methodology used is essential. The HIP was a group medical plan in the 1960s which had nearly 700,000

members collectively among 31 medical groups. For the study, 62,000 women age 40-64 from the HIP were enrolled, assigned to either treatment or control by systematic list sampling. In this study, treatment was defined as an invitation to four rounds of annual screening, a clinical exam and mammography (two views, cephalocaudal and lateral) (Freedman, Petitti and Robins 2004). The overall goal of the study was to measure the effect of the invitation to screening, not the effect of screening itself. The study has been criticized due the fact that there were only four rounds of screening, and that some women in the treatment group declined to be screened. For those who were screened, 67% were screened at least once, and 40% of the patients in the treatment group were screened four times (Freedman, Petitti and Robins 2004). The results of the study showed that the relative risk, defined as the probability of the event in the treatment group divided by the probability of the event in the control group, was 0.83. In regards to absolute risk reduction in breast cancer mortality, the results of the HIP study was 1.4193 per 1,000, suggesting that the intervention is beneficial. The NNT (Number Needed to Treat) in a 10 year period to prevent one additional bad outcome was 916 (Green and Taplin 2003).

The Swedish Two-County trial was performed in two Swedish counties, Kopparberg and Östergötland. All women age 40 and over in the two counties were eligible for the study. Each county was divided into blocks, and each block was further subdivided into clusters, with the clusters being small geographical areas with an administrative identity. The reason for this division was to make the clusters similar within the blocks in regards to demographics and socioeconomics. There were seven blocks in the county of Kopparberg, each of which were subdivided into three clusters. For each block, two clusters were randomly chosen to be the active study population or intervention group, with the other being

the passive study population or control. Östergötland had 12 blocks, and the blocks in this county were divided into two clusters. For each block, one cluster was randomly chosen to be the active study population, and the other was the passive study population. Randomization for the study began on a block by block basis in 1977 for Kopparberg, and in 1978 for Östergötland. Once the randomization process was complete, the active study population in a block was invited to screening. There were two to four rounds of screening, with more for younger women and fewer for older women. From 1984-1986, the passive study population was invited for screening, after which the study was closed. After the trial was closed, women were invited to screening as part of their routine health care (Freedman, Petitti and Robins 2004). Results of the study showed a breast cancer mortality relative risk of 0.68, an absolute risk reduction in breast cancer mortality of 1.8095 per 1,000, and a number needed to treat of 553 (Green and Taplin 2003).

Controversy over the effectiveness of mammography arises from other large-scale randomized clinical trials which show no reduction in mortality, with some concluding that patients are actually being harmed from the radiation dose associated with mammography and unnecessary surgical procedures that are generated based on data obtained from mammograms. A prominent study showing no effect is the Canadian National Breast Screening Study. This study covered two age groups, ages 40-49 and ages 50-59. Women were recruited to the study from 1980 to 1985, and were followed until 1988, with an average follow-up time of 8.5 years. In both age categories, patients enrolled in the study were volunteers presenting at a screening center and signed the consent form. The study participants were divided into two groups, with participants in both groups instructed in how to perform a breast self exam. Patients randomized into the treatment arm were invited to

four screening exams, and 62% of them were invited to a fifth screen. In the treatment arm, exams in both age groups consisted of mammography and physical exam. For the patients in the control arm, the protocol was different for each of the two age groups. In the age 40-49 age group, the control group received a physical exam at the first screen, after which receiving "usual care". For the 50-59 age group, patients were offered four to five rounds of screening by physical exam. Patient enrollment in the 40-49 age group was 50,430, and 39,405 women were randomized to the 50-59 age group (Freedman, Petitti and Robins 2004). In the 40-49 age group, results of the study produced a breast cancer mortality relative risk of 0.98, with no reduction in absolute risk. Results in the 50-59 age group produced a breast cancer mortality relative risk of 1.14, indicating a negative benefit, and no reduction in absolute risk (Green and Taplin 2003).

Most of the large-scale randomized clinical trials have shown that mammography is beneficial, with most trials showing a reduction in breast cancer mortality of 20-30%. The technology used for x-ray imaging of the breast continues to advance, based heavily on the beneficial outcomes from clinical trials. The vast majority of evidence indicates a substantial reduction in mortality from breast cancer from mammographic screening. Determining if this reduction justifies the associated financial and human costs will depend on the prevailing rates of breast cancer, the availability of facilities and expertise, the costs of these, and numerous other considerations (Tabar et al. 2003).

5.3 Screen-Film System Design Characteristics

There are more than 30 companies that provide dedicated mammography x-ray units, but there are certain characteristics inherent to all of these systems. Characteristics of

mammography systems include appropriate beam quality, grid capability, breast compression device, and automatic exposure control.

The majority of dedicated mammography systems use a molybdenum target with a beryllilum window and molybdenum filters. Use of low energy photons, such as those emitted by the K_α and K_β emission lines (17.9 and 19.6 keV respectively) from molybdenum, provide high subject contrast for breasts of average thickness (Haus 1990). To maximize image contrast, conventional mammography is performed at approximately 26 kilovolts peak (kVp). The use of x-rays in this energy range results in a relatively high mean glandular dose to the patient, typically 1 to 2 milligrays per image (Feig and Yaffe 1996). A molybdenum filter with a typical thickness of 0.03 mm is used in dedicated mammography system because the k-shell absorption of molybdenum strongly reduces photon energies greater than 20 keV from the transmitted x-ray beam.

5.4 Computer Aided Diagnosis Applications for Mammography

Mammographic screening programs have been proven to be an effective method for the early detection of breast cancer, but many cancers are still being missed or misinterpreted. Studies have shown improvements in breast cancer detection rates using double reading by two radiologists, especially with arbitration, but this increases the cost of screening programs. The development of computer algorithms to aid in the detection of malignant features in mammograms has received considerable attention. Computer-aided diagnosis (CAD) is often defined as being a diagnosis made by a radiologist who takes into consideration the results of an automated computer analysis of radiographic images (Doi et al. 1992). CAD is being developed to improve diagnostic accuracy by reducing false-

negatives and improving image interpretation by using the computer output as a second resource for evaluation.

Previous studies have shown that the average breast screening radiologist can miss between 4 and 38% of cancers, indicating that CAD has a potential niche in helping to increase detection rates. Mammograms are among the most difficult of radiological images to interpret, and there are a variety of reasons explaining how cancers are missed. The most obvious reason why a cancer is missed is due the fact that the reader's search pattern may not have included the part of the image with the lesion, or the reader may have scanned the area but failed to detect the cancer. Another common error is a situation where the reader detects an abnormality, but misclassifies or misinterprets the lesion, classifying it as being normal (Astley and Gilbert 2004). The accuracy of mammography interpretation is highly dependent on the observational and interpretative skills of the radiologist, and there can be a wide variation in performance ability between observers. However, no matter how well trained and committed the observer is, there are situations where an observer does not perceive an abnormality that the same observer would have detected at another reading session (Castellino 2002). This type of perception error is referred to as an observational error, and it can be caused by something as simple and common as fatigue.

Most CAD systems are focused on the detection of either microcalcification clusters or masses, with many different algorithms under development for each. The detection of masses is difficult because masses have varying sizes, shapes, and densities, have poor image contrast, and can be highly connected to the surrounding parenchymal tissue. This is especially true in the case of spiculated lesions, which are surrounded by a nonuniform tissue background with similar characteristics (Qian et al. 1999). Detection methods for identifying

microcalcifications have been more successful mainly due the fact that there are few other mammographic features with a similar shape, size, distribution, and brightness of microcalcifications. The sensitivity of current detection methods for identifying clusters of malignant microcalcifications is greater than 98%, whereas the corresponding performance statistics for detecting masses are considerably lower (Astley and Gilbert 2004).

With the sensitivity of some detection algorithms approaching human readers for certain abnormalities, the specificity of these detection methods is still relatively low. Increasing demands on breast imaging radiologists have made double reading difficult to implement, and the demands on radiologists will only increase as utilization increases. A possible solution to this problem is the use of computers to detect abnormalities in mammograms, but many problems remain in the implementation of this idea. If CAD algorithms were used to "pre-screen" mammograms, radiologists could focus their attention on mammograms that have lesions deemed suspicious by the computer. In order for this to be an effective strategy, CAD systems would have to be able to detect all signs of abnormality with very high sensitivity, and the specificity would have to be sufficient to classify a reasonable proportion of the films as normal (Astley and Gilbert 2004). While this sounds promising, mammograms deemed normal by the current CAD systems would be obviously normal to the trained radiologist and not represent a major savings in time and effort.

Several studies have been conducted using CAD in conjunction with screening mammography. Burhenne et al reported the reported the results of a 13-center study that collected 1083 consecutive screening mammograms on which biopsy-proven cancer was first detected. A CAD device (R2 Technology, version 2.2) was used to make the location and classification of cancers present in the images. Results indicate that the CAD was far more

accurate in detecting cancers having features with microcalcifications (98.3%) than with lesions present as masses (85.7%). The overall cancer detection rate was 90.4%, and CAD analysis of 100 normal cases produced 0.5 false-positive marks per image (Burhenne, Wood and D'Orsi 2000). Use of a different CAD system (CADx Medical Systems, Quebec, Canada) on 273 mammographically screen-detected cancers was reported by Brem et al. The CADx system correctly marked 95% (118/124) of the cancers containing microcalcifications, and 84% (125/149) of the cancers presenting as a mass. An overall detection rate of 89% (243/273) was reported, and an analysis of 155 normal cases produced 1.3 false positive marks per image (Brem, Schoonjans and Hoffmeister 2000; Castellino 2002).

Other clinical studies report similar results, indicating that CAD systems have made significant improvements and are approaching the level of sophistication and reliability necessary for incorporation into clinical practice. Many of the studies used to support CAD systems is still based on retrospective data, and it yet to be determined whether the increasing sensitivity of CAD algorithms will be masked by the relatively large number of prompts erroneously marking normal regions. In order for this technology to make a significant impact, radiologists must become comfortable with using these systems, and most importantly, trust the information they provide. The introduction of commercially available CAD systems and recent Food and Drug Administration approval for several of these systems will certainly intensify development in the coming years.

Chapter 6: Fundamental Physics of Diffraction Enhanced Imaging

6.1 Synchrotron X-ray Generation

Synchrotron radiation is generated through the movement of charged particles in a circular orbit, causing a release of photons. Generation of x-rays begins with the injection of electrons from an electron gun into a linear accelerator, where the electrons are accelerated to approximately 99.99986 percent of the speed of light. Electrons are then fed into a booster ring, where the electrons are forced to travel in a circular orbit through the use of strong magnetic fields. The booster ring is used to feed electrons into a large main storage ring, which is maintained under vacuum to reduce drag. Beamlines are placed tangentially to the storage ring and guide the x-rays to an experimental hutch, where they can be used as needed for experiments.

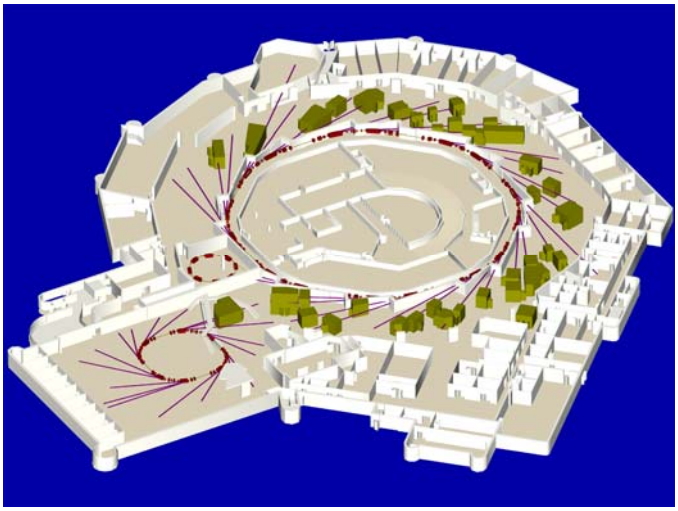

FIGURE 6.1: National Synchrotron Light Source Experimental Floor
Image provided courtesy of NSLS, Brookhaven National Laboratory

6.2 Bragg's Law of Diffraction

Derived by Sir W.H. Bragg and his son Sir W.L. Bragg in 1913, Bragg's law of diffraction explains why the cleavage faces of crystals appear to reflect x-rays at certain angles of incidence. Bragg's law is defined as

$$n\lambda = 2d\sin(\theta)$$

where λ is the wavelength of the incident x-ray beam, θ is the angle of incidence, d is the distance between the atomic layers in the crystal, and n is an integer.

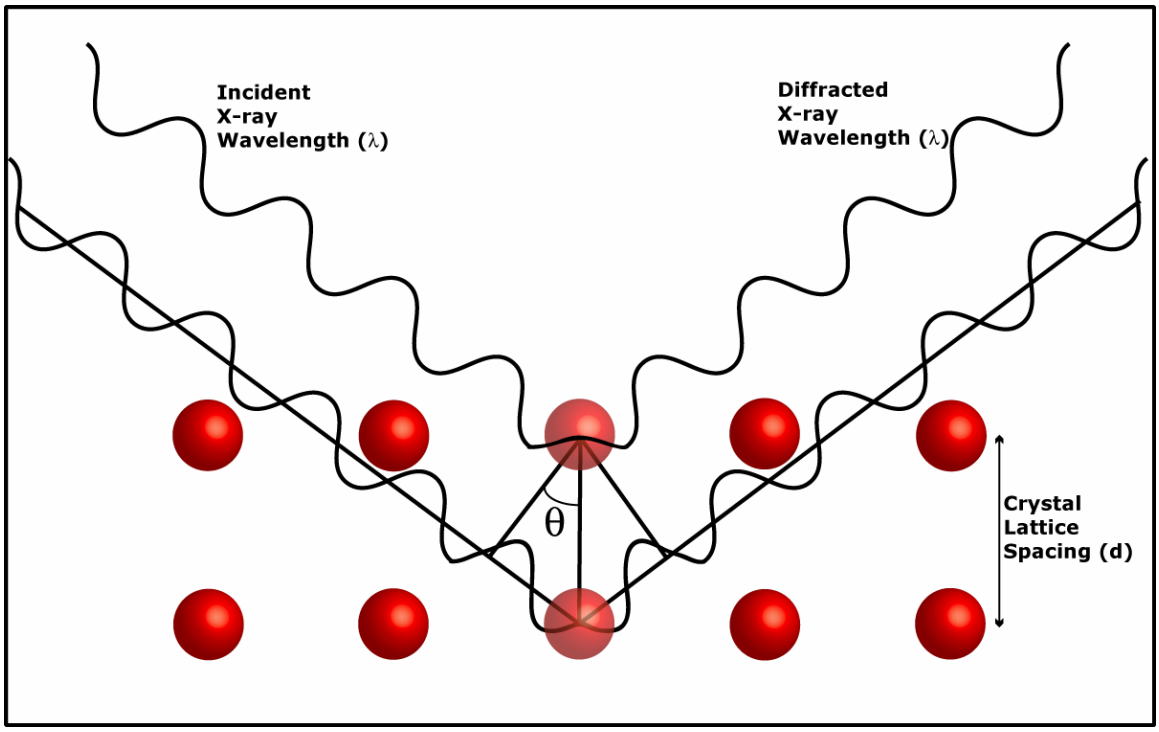

FIGURE 6.2: Illustration demonstrating Bragg's law of x-ray diffraction

6.3 Properties of Diffraction Enhanced Imaging

A monoenergetic radiograph contains several components that can affect image contrast and resolution: a coherently scattered component I_c, an incoherently scattered component I_I, and a transmitted component. X-rays passing through an object or medium where there are variations in density can be refracted, resulting in an angular deviation. Specifically,

deviations in the x-ray range result from variations in ρt along the path of the beam, where ρ is the density and t is the thickness. A fraction of the incident photons may also be diffracted by structures within an object, which are generally on the order of milliradians and referred to as small angle scattering. The sum total of these interactions contributed to the recorded intensity in a radiograph I_N, which can be represented as

$$I_N=I_R+I_D+I_C+I_I$$

System spatial resolution and contrast will be degraded by the contributions of both coherent and incoherent scatter (Chapman et al. 1997). Anti-scatter grids are often used in medical imaging to reduce the contribution of scatter, but there performance is limited and use of a grid often requires a higher dose to compensate for the loss in intensity.

The Diffraction Enhanced Imaging (DEI) method first introduced by Chapman et al. utilizes a silicon analyzer crystal in the path of the post-object x-ray beam to virtually eliminate the effects of both coherent and incoherent scatter. The narrow angular acceptance window of the silicon analyzer crystal is referred to as its rocking curve, and is on the order of microradians for the x-ray energies used in DEI. The analyzer acts as an exquisitely sensitive angular filter, which can be used to measure both refraction and extinction contrast. Extinction contrast is defined as the loss of intensity from the incident beam due to scattering, which can produce substantial improvements in both contrast and resolution.

A thorough understanding of the analyzer crystal rocking curve is essential to underlying contrast mechanisms present in DEI. An example rocking curve is presented in Figure 6.3, illustrating the dramatic change in beam intensity as a function of angle.

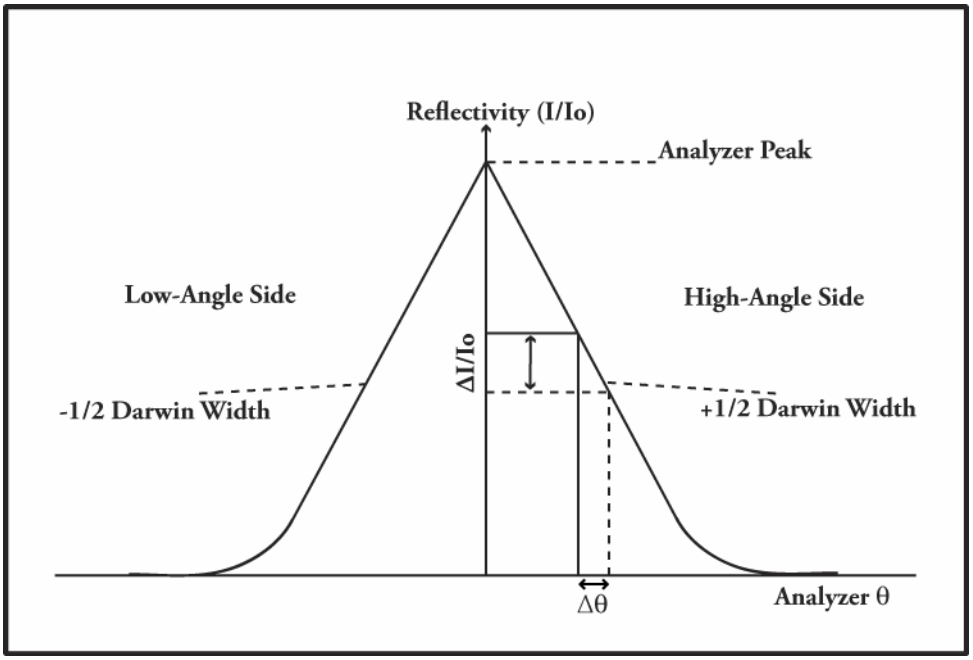

FIGURE 6.3: Illustration of analyzer crystal rocking curve

The Darwin Width (DW) is used to describe reflectivity curves, and is approximately the Full Width at Half Maximum (FWHM) of the reflectivity curve. Points at -1/2 DW and + 1/2 DW have the steepest slope of the rocking curve, producing the greatest change in photon intensity per microradian for a particular analyzer reflection and beam energy. Contrast at the peak of the analyzer crystal rocking curve is dominated by x-ray absorption and extinction, resulting in near scatter-free radiographs. Refraction contrast is highest where the slope of the rocking curve is greatest, at the -1/2 and +1/2 DW positions. A method first proposed by Chapman et al. uses these points to extract the contrast components of refraction and apparent absorption from these image pairs.

The following paragraph describes of the Chapman method for extracting the contrast components of refraction and apparent absorption from an image pair. When the analyzer crystal is set to an angle representing +/- 1/2 DW for a given reflection and beam energy, the

slope of the rocking curve is relatively consistent and can be represented as a two-term Taylor series approximation

$$R(\theta_0 + \Delta\theta_Z) = R(\theta_0) + \frac{dR}{d\theta}(\theta_0)\Delta\theta_Z .$$

If the analyzer crystal is set to the low-angle side of the rocking curve (-1/2 DW), the resulting image intensity can be represented as

$$I_L = I_R\left((R(\theta_L) + \frac{dR}{d\theta}\Big|_{\theta=\theta_L} \Delta\theta_z) \right).$$

The recorded intensity for images acquired with the analyzer crystal set to the high-angle position (+1/2 DW) can be represented as

$$I_H = I_R\left(R(\theta_H) + \frac{dR}{d\theta}(\theta_H)\Delta\theta_z \right).$$

These equations can be solved for the changes in intensity due to apparent absorption (I_R) and the refraction in angle observed in the z direction ($\Delta\theta_Z$) represented as

$$\Delta\theta_z = \frac{I_H R(\theta_L) - I_L R(\theta_H)}{I_L\left(\frac{dR}{d\theta}\right)(\theta_H) - I_H\left(\frac{dR}{d\theta}\right)(\theta_L)}$$

$$I_R = \frac{I_L\left(\frac{dR}{d\theta}\right)(\theta_H) - I_H\left(\frac{dR}{d\theta}\right)(\theta_L)}{R(\theta_L)\left(\frac{dR}{d\theta}\right)(\theta_H) - R(\theta_H)\left(\frac{dR}{d\theta}\right)(\theta_L)}.$$

These equations can be applied to the high and low angle images on a pixel-by-pixel basis to separate the two contrast elements into what is known as a DEI apparent absorption and refraction image.(Chapman et al. 1997)

6.4 Experimental Setup at National Synchrotron Light Source

The current DEI system used for the experiments described in this document was established in January 1998 at the National Synchrotron Light Source X-15A beamline. Numerous upgrades have been made to the beamline since it was commissioned, including the addition of two digital detectors and modifications designed to increase system stability.

The x-ray ring at the NSLS is a 2.8 GeV synchrotron, capable of producing high flux x-rays from 10 to 60 keV. X-rays emitted from the synchrotron are highly collimated with a vertical divergence of approximately 0.2 milli-radians. A beamline pipe 16.3 meters in length connects the experimental hutch to the synchrotron x-ray ring. The high intensity polychromatic x-ray beam enters the experimental hutch and is rendered monochromatic through the use of a double crystal monochromator. The monochromator has two crystals (each 150 mm wide x 90 mm wide x 10 mm high) that are both water-cooled to reduce thermal loading.

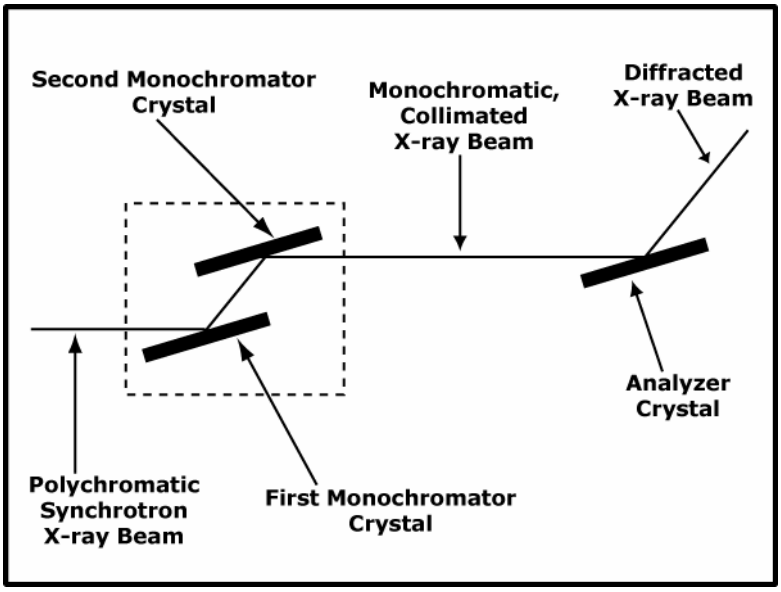

FIGURE 6.4: Passage of x-ray beam through the monochromator and analyzer crystal

Monochromatic x-rays then proceed through an ion chamber and high speed shutter to a sample stage, creating a line source x-ray beam with maximum dimensions of 120 mm in width and 3 mm in height. With the beam position fixed, the sample is moved through the x-ray beam using a translation stage driven by a stepper motor (Newport Electronics, Santa Anna, CA).

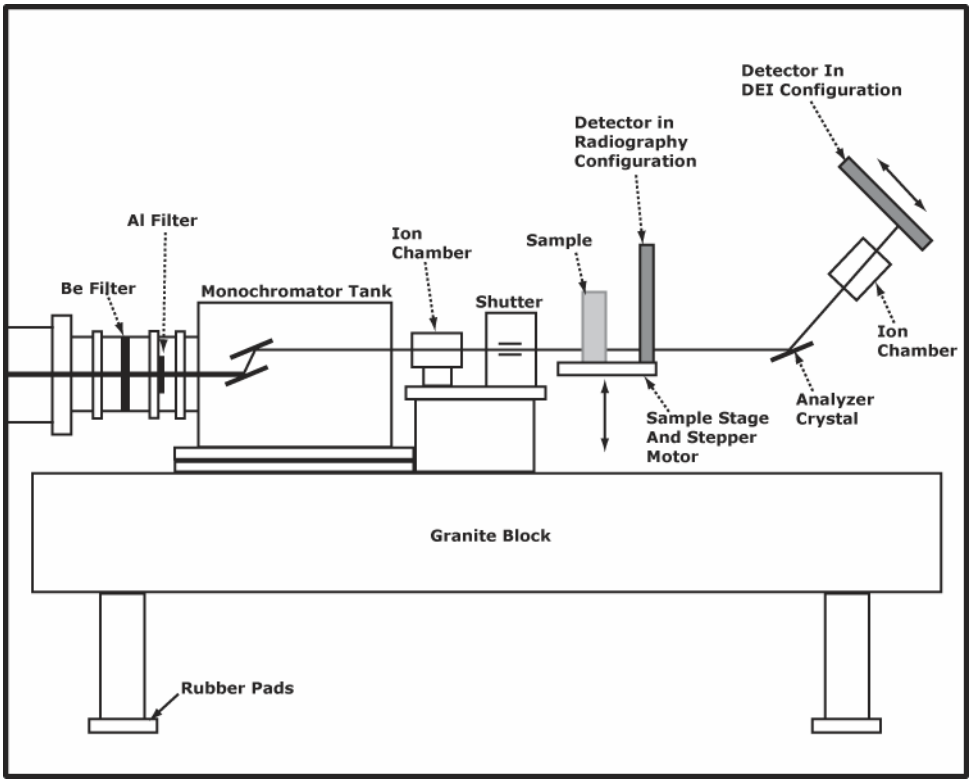

FIGURE 6.5: DEI setup at the NSLS X15A beamline.

Conventional radiographs can be obtained by placing the detector directly behind the sample in the beam path, removing any effects of the analyzer crystal. Images acquired in this configuration are similar to conventional x-ray systems in that absorption is the primary contrast mechanism, but synchrotron radiographs have been shown to have better contrast when compared to images acquired using conventional x-ray systems (Kiss, Sayers and Zhong 2003).

Diffraction Enhanced Images are acquired by placing the detector after the analyzer crystal at an angle twice that of the calculated Bragg angle. A summary of the angles used for imaging in the 18-60 keV range is presented in Figure 8.1. The use of a line source x-ray makes it necessary to move the detector in a direction opposite that of the sample for DEI and in the same direction for obtaining synchrotron radiographs.

All initial DEI images were acquired using a Fuji BAS2500 image plate reader using Fuji HRV image plates (Fuji Medical Systems, Stamford, CT). The plates are approximately 0.5 mm in thickness composed of a flexible plastic plate coated with a photostimulable phosphor ($BaFBR:Eu^{2+}$) combined with an organic binder. Images are scanned using the FUJI BAS2500 at a resolution of 50 microns and 16-bit gray level. Image plates offer several advantages over digital detection systems, including a larger imaging area and a fixed noise level.

A digital detector was added to the system to enable DEI applications that were not practical or possible using image plates, including Diffraction Enhanced Computed Tomography and Multiple Image Radiography. There are two detectors currently available for use at the NSLS X-15A beamline. The first is a Shad-o-Box 2048 (Rad-icon Imaging Corp, Santa Clara, CA) with a 50 x 100 mm active area and 12-bit output. This detector utilizes a photodiode array containing 1024 by 2048 pixels with 48 micron pixel spacing in direct contact with a Gd_2O_2S scintillator screen. The second detector available for use is a Photonic Science VHR-150 x-ray camera (Robersbridge, East Sussex, UK) with a FOV of 120mm x 80mm and a 30 micron pixel size. Both detectors can be mounted in the same manner as the image plate, either in a radiography or DEI configuration.

Chapter 7: Multiple Image Radiography

7.1 Multiple Image Radiography Theory

The use of image pairs to generate apparent absorption and refraction images has become a well known method for separating the contrast components of absorption and refraction, but this method does have limitations. One primary limitation is that this processing method does not directly take into account the effects of ultra-small angle scatter, which can lead to significant errors (Wernick et al. 2003). If ultra-small angle scattering is present, which is common in biological tissues, the width of the rocking curve is increased causing the slope of the curve to be decreased. A decrease in the slope of the rocking curve will decrease the refraction signal, resulting in a loss of structural information in the refraction image (Oltulu et al. 2003). In order to reduce these errors, a method utilizing multiple images acquired across the analyzer crystal rocking curve was proposed to address this problem. This method, known as the extinction-refraction-absorption (ERA) analysis method, produced an image representing an object's absorption, refraction, and extinction (ultra-small angle scatter).

Acquiring images across the analyzer crystal rocking curve without an object in the beam will generate an intrinsic rocking curve, which represents the convolution of the monochromator and analyzer crystal at different levels of analyzer reflectivity. The intrinsic rocking curve will not be altered by absorption, refraction, or ultra-small angle scatter, which makes it an excellent reference point. When an object is placed in the beam, changes in the

rocking curve on a pixel by pixel basis can be use to determine which x-ray interactions are leading to contrast in a given pixel (Oltulu et al. 2003).

The model used in the ERA method models the rocking curve as a Gaussian distribution, which is an approximation, since the rocking curve is a convolution of the monochromator and analyzer, and is triangular. The formula for this model is

$$R(\theta_A) = e^{-\mu_T t} \int_{-\infty}^{\infty} \left\{ e^{-\chi_x t}\delta(\theta) + \frac{1}{\sqrt{2\pi}\omega_s}\left(1 - e^{-\chi_s t}\right) e^{\frac{-\theta^2}{2\omega_s{}^2}} \right\} \times R_{\text{int}}(\theta - (\theta_A - \theta_Z))d\theta$$

where μ_T is the linear absorption coefficient, χ_s is the extinction coefficient, t is the object thickness, θ_z is the refraction angle, and ω_s is the Gaussian with of scatter distribution (Oltulu et al. 2003).

A more refined version of the ERA method was developed and called Multiple Image Radiography (MIR), which addresses many of the problems present in earlier processing methods and allows for a more complete description of the image contrast components. Images processed using the MIR method generate not only an absorption and refraction image, but also generates an ultra-small angle scatter image. MIR has also been shown to correct for substantial errors present in the DEI apparent absorption and refraction images and is more robust to noise.(Wernick et al. 2003)

As with the ERA method, MIR uses the analyzer crystal rocking curve to generate images representing an object's absorption, refraction, and ultra-small angle scatter. If the intrinsic rocking curve is the baseline, then changes that decrease the area under the curve can be interpreted as absorption alone since photon absorption will decrease overall intensity. For a purely refractive event, the centroid of the rocking curve will be shifted, but the width of the rocking curve will remain constant. Interactions that lead to ultra-small angle scattering will

scatter photons across the angular distribution of the rocking curve, which will cause the curve to widen. Assuming that photons are not scattered outside the acceptance window of the rocking curve, scattering effects will not affect the area under the curve, just the shape of the curve. If the rocking curve is assumed to be Gaussian in nature, then the variance of the curve can be used to represent the amount of scattering present.

The rocking curve width decreases as energy increases, which makes it necessary to modify the sampling procedures to account for this change. At 18 keV the rocking curve FWHM is 3.64 microradians, and decreases to 1.11 microradians at 60 keV. As the rocking curve narrows, the angular range over which refraction contrast is significant is reduced. To compensate for this, the angular sampling range and increment must be reduced. The increased slope of a 60 keV rocking curve is beneficial in that it generates a larger change in intensity per microradian. When using flux limiting x-sources such as an x-ray tube, one should maximize these properties to generate the most refraction possible for a given flux.

Chapter 8: Imaging Procedures and Quality Control for using Diffraction Enhanced Imaging and Multiple Image Radiography at the National Synchrotron Light Source

8.1 NSLS DEI acquisition parameters and system tuning

Image acquisition at the NSLS begins with the selection of an appropriate beam energy for a given experiment, which for this system can range from 10 keV to 60 keV. Selection of a particular energy for imaging is accomplished by using Bragg's law to calculate the appropriate angle for the desired wavelength. The first crystal in the monochromator has only one axis of movement which can be tuned to a particular angle, removing all other energies from the incident x-ray beam. Figure 8.1 lists the angles needed to acquire images between 18 keV and 60 keV.

Energy (keV)	θ (degrees)	2θ (degrees)
18	19.23	38.46
19	18.19	36.38
20	17.25	34.50
21	16.41	32.82
22	15.64	31.28
23	14.94	29.88
24	14.30	28.60
25	13.72	27.44
26	13.18	26.36
27	12.69	25.38
28	12.23	24.46
29	11.80	23.60
30	11.40	22.80
31	11.03	22.06
32	10.68	21.36
33	10.35	20.70
34	10.05	20.10
35	9.76	19.52
36	9.48	18.96
37	9.22	18.44
38	8.98	17.96
39	8.75	17.50
40	8.53	17.06
41	8.32	16.64
42	8.12	16.24
43	7.93	15.86
44	7.75	15.50
45	7.57	15.14
46	7.41	14.82
47	7.25	14.50
48	7.10	14.20
49	6.95	13.90
50	6.81	13.62
51	6.68	13.36
52	6.55	13.10
53	6.43	12.86
54	6.31	12.62
55	6.19	12.38
56	6.08	12.16
57	5.97	11.94
58	5.87	11.74
59	5.77	11.54
60	5.67	11.34

FIGURE 8.1: Calculated Bragg angles for energy selection and DEI system tuning

There are three crystals in the system that must be tuned and carefully aligned, two crystals in the monochromator and the analyzer crystal. The first crystal and the analyzer crystal are tuned to the theta angle calculated for each energy. For example, to tune the system to 25 keV one would set the first crystal in the monochromator and the analyzer crystal to 13.72 degrees. The detector assembly is set at an angle twice that of the analyzer crystal, which in this case would be 27.44 degrees.

The second crystal in the monochromator and the analyzer must also be adjusted in the horizontal direction, referred to as the chi angle. If the horizontal alignment is off between these crystals, then there will be an intensity shift from left to right in the image. Two ion chambers are used to measure the flux emitted from both the monochromator and the analyzer, which are both divided into an inboard and outboard region. If viewing the x-ray beam from the source to the detector, the inboard region is on the right and the outboard region is on the left. The inboard and outboard regions are sampled to make sure that the rocking curve peaks are aligned; if not, the chi angle is adjusted.

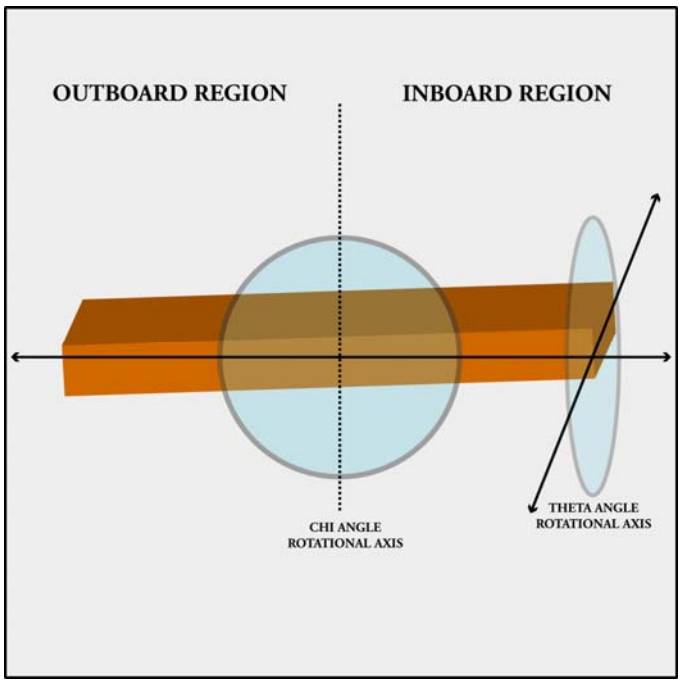

FIGURE 8.2: Crystal theta and chi angles of rotation

The incident flux on the first crystal in the monochromator is determined by the ring current of the synchrotron, which slowly decreases with time as the electrons in the ring lose energy. There are several places where the dose can be adjusted, including the aluminum filter thickness and placing absorbers in the path of the x-ray beam. The dose can be further reduced by detuning the second crystal in the monochromator away from the peak of the rocking curve, dramatically reducing the diffracted intensity if needed.

Sample acquisition time is determined by the incident flux, with the translation rate of the sample stage measured in steps/second. The scan speed can be increased or decreased by adjusting the dose, with a maximum translation speed of approximately 400 steps/second. Scan speed is not a critical factor when using image plates where the amount of noise is fixed, but it must be considered when using integrating digital detectors since the amount of noise is in part determined by acquisition time. When using a digital detector, the system should be tuned so that the scan speed is as close to maximum as possible.

Once the system is tuned for the proper energy and dose, the object to be imaged must be placed on the sample stage and aligned. The maximum width of the x-ray beam is 120mm, which physically limits the width of the resulting image. Use of a digital detector or image plate with a width less than 120mm will further limit the field of view. While there are no physical limits to sample height, the sample stage used at the NSLS has a maximum vertical displacement of 200 mm. For imaging a particular region of an object, one must determine where this region lies within the 200 mm range for the system. The position of the synchrotron x-ray beam is fixed, so the object vertical region of interest can be determined by its relative position to the beam.

The crystals used in a DEI system are considered to be homogenous in their ability to diffract photons over a given area of the crystal, but the structure of the crystal is such that there are minor regions of increased or decreased intensity. Since the object is scanned through a beam of fixed dimension, these "glitches" will be smeared across the vertical dimension of the image. The term "glitch" is often applied to these vertical lines, but these affects are expected and should be considered a known and expected property of the system.

Moving DEI and MIR from an experimental laboratory environment to a clinical environment requires the development of new quality assurance procedures to insure proper image acquisition. As with any imaging system that utilizes a digital detector, the response of the detector must be measured and incorporated into any subsequent processing algorithms.

Chapter 9: DEI/MIR System Stabilization

9.1 Description of Crystal Alignment and Stability at the NSLS X-15A Beamline

Use of the analyzer crystal to convert angular changes to intensity allows for exceptional contrast, but the fundamental assumption in this method is that the analyzer crystal rocking curve position remains constant over time. In practice, this is not the case, and with such a narrow rocking curve width even small changes in the analyzer peak position creates significant errors in the acquired image. The application of processing algorithms, such as DEI apparent absorption and refraction images, MIR, and MIR-CT requires a high degree of system stability. Achieving the goal of determining the absorption, refraction, and scatter parameters in breast tissue required a systematic engineering analysis of the NSLS X-15A beamline to isolate the factors causing instability.

Stability for a DEI system is this case will be defined as the ability to maintain a constant peak position of the analyzer crystal rocking curve over an extended period of time. To review, the polychromatic X-ray beam is incident on the first crystal in the monochromator, which is tuned to a particular angle using Bragg's Law to select a single photon energy. The diffracted monochromatic beam then encounters the second monochromator crystal, the sole function of which is to redirect the beam to a direction parallel to the incident beam and aligned with the analyzer crystal. When tuning the system for a particular energy, the first monochromator crystal is aligned first, and then the second

crystal is tuned to find the position of the beam. The monochromator tank is constantly flushed with helium to reduce the generation of ozone, which can quickly oxidize and damage critical components in the tank.

With the second crystal is aligned, the analyzer is scanned to find the position of the beam on the crystal. Rocking the crystal to find the beam position is analogous to scanning a radio dial to find a particular station, generating a sharp rise in intensity when the angular position of the analyzer is in perfect alignment with the second monochromator crystal. Once the analyzer is aligned, the system is tuned and ready for use.

Stability problems were noticed when the X-15A DEI setup was first initiated in 1998, so much so that it was difficult to obtain a single image with a fixed analyzer crystal position. The movement of the analyzer position with time is referred to as analyzer drift, and it became a primary limitation of the system from January 1998 to January 2004.

9.2 Initial Thoughts Regarding Sources of Analyzer Drift

Factors that can create drift in a DEI system fall into three categories: vibratory, mechanical, and thermal. The optical portion of a DEI system is sensitive to vibrations, since even minor vibrations on the crystals can cause minor changes in angle, resulting in changes in contrast. A large granite slab is used at the NSLS X-15A beamline to dampen vibrations from the external environment, which is an effective solution for a laboratory system. Measurements using an oscilloscope to monitor the post-analyzer x-ray beam indicate that there is approximately a 2-3% variation in intensity, which is attributed to vibrations from external drive fans and pumps at the beamline.

There are a variety of motors used to align the crystals, translate the sample stage and detector assembly. Picomotor drives are used with the first monochromator crystal, second

monochromator crystal, and the analyzer crystal to adjust the theta angle. The second monochromator crystal and the analyzer crystal use a second picomotor to adjust the chi angle. Any instability in these drive motors can create major deviations in the alignment of the system, and mechanical drift was initially thought to be a primary cause of DEI system instability. The motors used to drive the sample stage and detector assembly are important for image quality, but they do not contribute to the stability of the x-ray beam.

A third contributor to system instability is thermal, resulting from both the heat produced from the incident x-ray beam and the system drive motors and amplifiers. While thermal variations in the system were known to have some effect on system stability, it was not considered a primary destabilizing factor. The link between thermal variations and system instability became evident when a critical observation was made, drift in the analyzer was relatively consistent and periodic. There is only one variable in a DEI system that is periodic, and that is the heat generated and lost by opening and closing the main x-ray shutters.

9.3 Theoretical Explanation of Thermal Drift

Experimental tests and observations obtained to isolate sources of instability point to the expansion and compression of the silicon crystal structure as a primary source of drift. A simple explanation of these experimental observations can be found using Bragg's law

$$\lambda = 2d\sin(\theta).$$

Considering one crystal set to a given angle to diffract a desired energy, any change in the *d* spacing of the lattice structure can change the angle of the diffracted beam. The heat generated from the x-ray beam in the monochromator will cause the silicon crystal to expand in accordance with its coefficient of linear expansion, $\Delta d/d = 3\text{x}10^{-6}\ \Delta T\ (°C)$.

Using Bragg's law and solving for *d*, one obtains the following equations:

$$\lambda = 2d\sin\theta$$

$$d = \frac{\lambda}{2\sin\theta}.$$

Taking the derivative of the above equation yields

$$\Delta d = -\left(\frac{\lambda}{2}\right)\left(\frac{1}{\sin^2\theta}\right)(\cos\theta)\Delta\theta.$$

Substituting for *d* and rearranging yields

$$\frac{\Delta d}{d} = -\left(\frac{\cos\theta}{\sin\theta}\right)\Delta\theta = \frac{-\Delta\theta}{\tan\theta},$$

which can be rearranged to

$$\Delta\theta = -\tan\theta\left(\frac{\Delta d}{d}\right).$$

Substituting the silicon linear expansion coefficient for $\frac{\Delta d}{d}$ yields

$$\Delta\theta = -3\times10^{-6}\tan\theta\Delta T.$$

Using the Bragg angles for 18 keV and 40 keV, 19.2 and 8.4 degrees respectively, one would expect to see an angular change of 1.05 microradians per degree Celsius at 18 keV and 0.44 microradians per degree Celsius at 40 keV. Using this calculation as a theoretical explaination of drift, one would expect to see overall beamline stability increase and analyzer drift decrease with increasing beam energies.

9.4 Retrofitting of Aluminum Filter Assembly

Initial analyzer stability tests in January 2004 indicated that the system was highly unstable, with a stability of the peak analyzer position averaging less than 60 seconds. While this may be acceptable for single image scans, it was unacceptable for MIR and any CT applications. Multiple drift assessments measuring the change in analyzer position from a

cold start through 12 hours of continuous operation were between 50 and 100 microradians. With an awareness of the importance of temperature on system stability, a comprehensive assessment of all systems components was performed to determine which heat sources could be moderated or eliminated.

One system component that experiences large variations in temperature is the aluminum filter assembly, whose function is to attenuate unwanted low energy x-rays. These 0.5 millimeter thick aluminum sheets heat up quickly when exposed to the synchrotron white beam, and cool off rapidly when the beam is turned off. The proximity of the aluminum filter assembly to the thermally sensitive crystals in the adjacent monochromator tank made this a primary source of instability. A heat sink was needed to remove heat generated by the filters and thermally isolate the aluminum filter assembly.

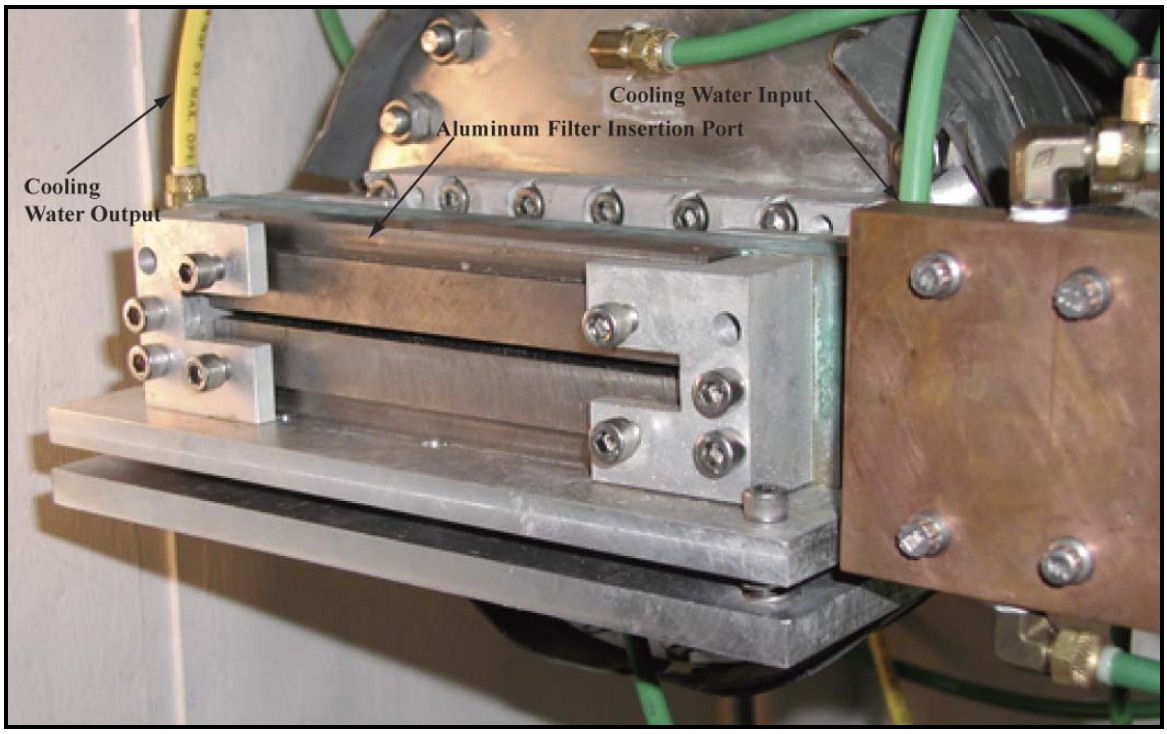

FIGURE 9.1: Aluminum filter heatsink

A new copper filter assembly was designed to thermally isolate the heat generated by the aluminum filters and transfer that heat to circulating, high-flow chilled water conduit. The aluminum filters were also reduced in size to limit the radiating surface area and increase contact with the copper heatsink. Stability tests acquired after instillation of the water cooled filter assembly indicated that the overall system drift was reduced by approximately an order of magnitude, with 12 hour continuous operation drift measurements averaging negative 6 microradians from a cold start.

9.5 Retrofitting of Monochromator Crystal Assembly

The dramatic reduction in overall system drift after the addition of the water cooled filter heatsink made clear the importance of maintaining an isothermal environment for the analyzer and monochromator crystals. However, with the obvious source of heat removed with the filter assembly, isolating other sources would prove to be a challenge. A systematic analysis of each system component and the periodic changes in the external environment was required to isolate the remaining sources of thermal drift.

All amplifiers and control systems that could be removed from the experimental hutch were relocated outside of the hutch, but the drive motors that control the sample stage and detector assembly could not be removed. In addition, the hutch door was closed as much as possible to help maintain a constant ambient air temperature. Twelve hour measurements of the analyzer crystal temperature, ambient air temperature, and gravity cooling water temperature did not indicate any substantial changes in temperature. Continued experiments indicated that there were significant thermal variations in the aluminum base of the second monochromator crystal, which is in direct contact and heated by the second monochromator crystal.

The primary function of the second monochromator crystal is to diffract the monochromatic x-ray beam from the first monochromator crystal and horizontally align the beam with the analyzer crystal. In theory, the interactions of the x-rays with the crystal are elastic, so there should be no heat generation. This is not the case with the first monochromator crystal, since much of the high intensity, polychromatic synchrotron white beam is absorbed in the internal structure of the first crystal. To reduce vibrations, a gravity driven water cooling system was installed when the system was first built to remove excess heat from the first crystal. At the time, it was believed that active cooling was not required for the second monochromator crystal, but temperature measurements acquired over a period of 24 hours indicated that modifications were necessary.

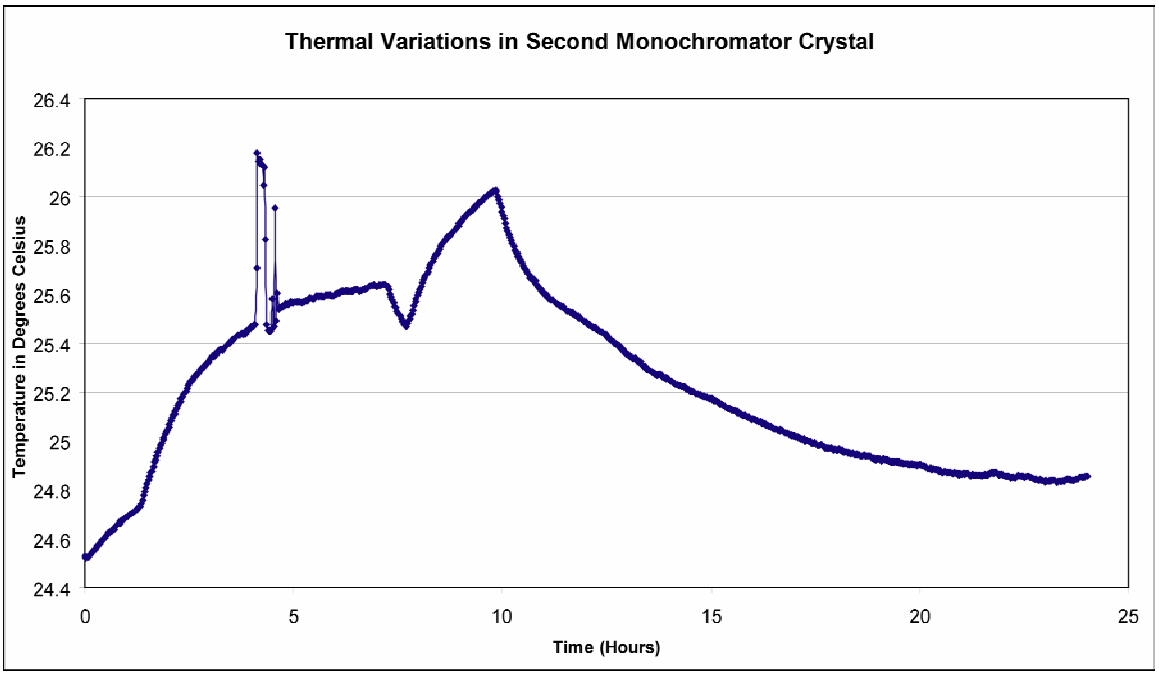

FIGURE 9.2: Thermal loading on the second monochromator crystal

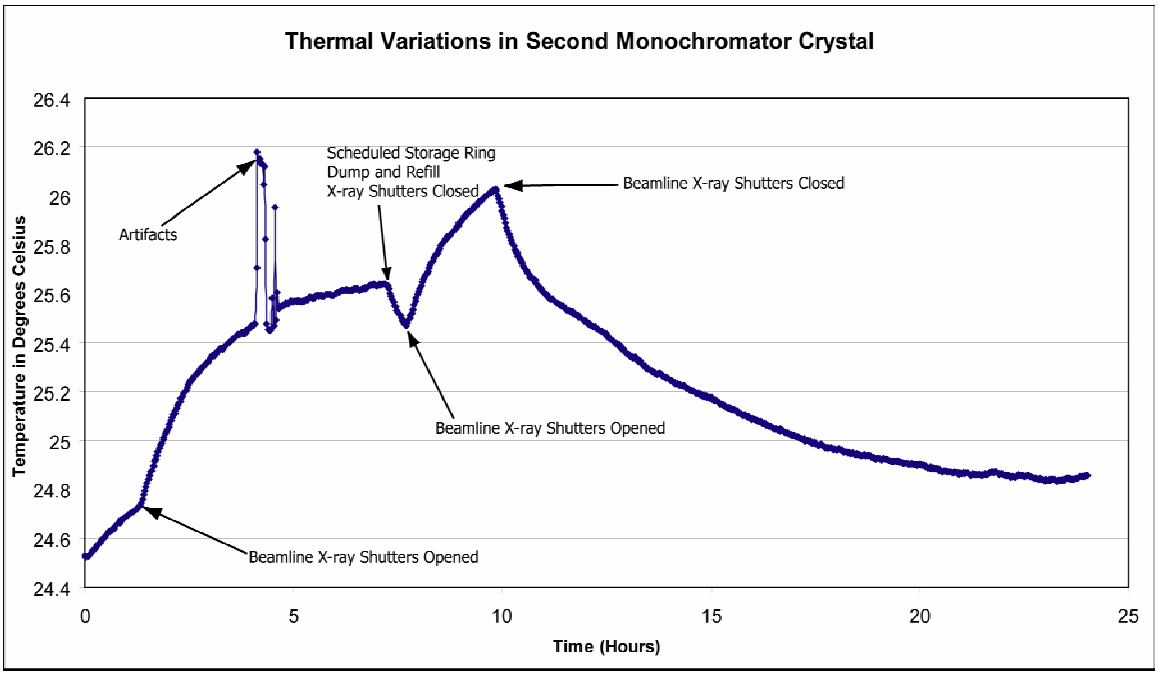

FIGURE 9.3: Annotated graph of thermal loading on the second monochromator crystal in relation to the x-ray beam

A thermistor was placed on the aluminum support plate and the temperature was measured every 5 seconds over a typical operations period of 24 hours, presented in Figure 9.2. The temperature of the support plate increased approximately 1.3 °C from the period where the beam was turned on and off. The current of the synchrotron storage ring falls off slowly with time and has to be dumped and refilled, which is evident in the temperature graphs. After 12 hours of continuous operations, the beamline was shut down to determine how long it takes for the temperature to return to baseline. An analysis of the data indicates that there was enough heating on the second crystal to justify retrofitting the support plate for active water cooling. An annotated analysis of how normal beamline operations influenced crystal temperature is presented in Figure 9.3. With this source of thermal instability identified, a copper support plate was designed with an internal conduit for water flow and heat exchange.

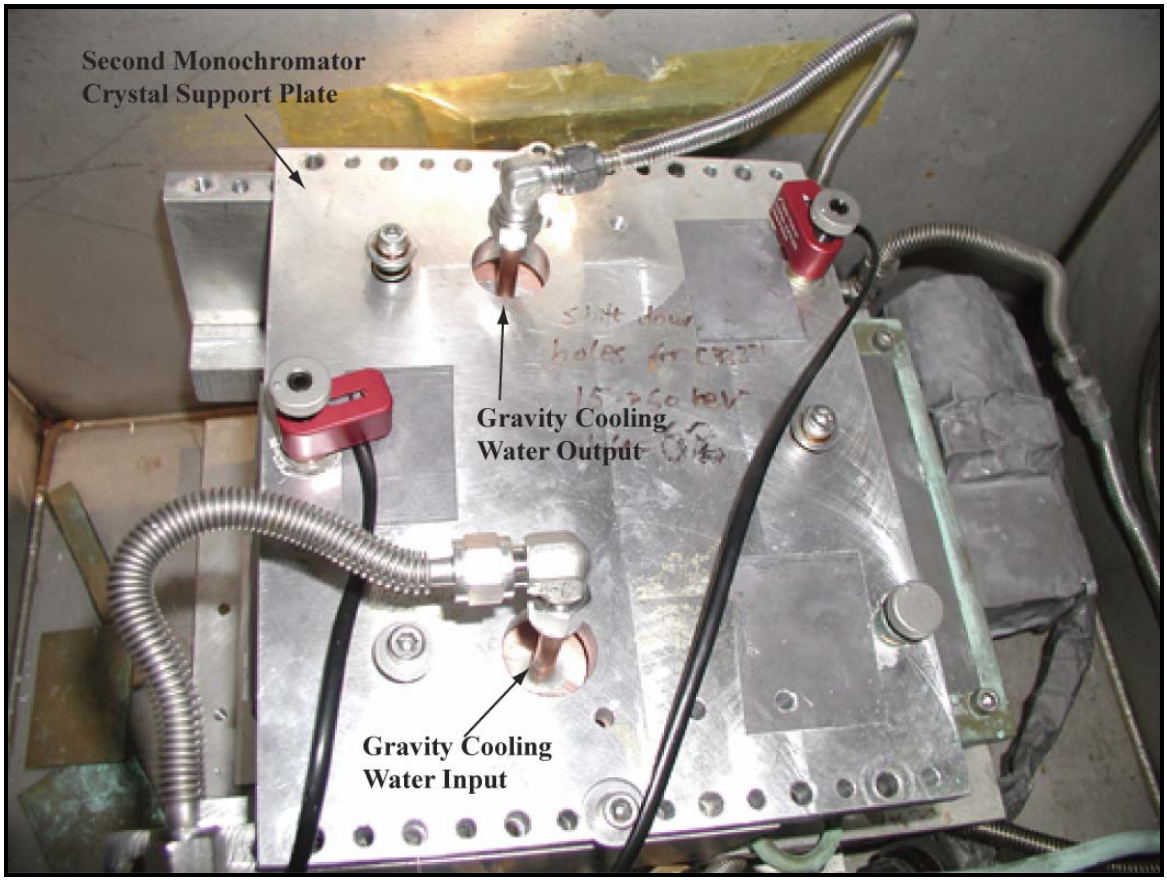

FIGURE 9.4: Overhead view of retrofitted second monochromator base and support plate with water cooling lines

9.6 Post-upgrade Stability

After approximately 2000 hours of beamline operations, 1000 hours with the upgraded monochromator, a predictable trend in the stability of the beamline has been measured and evaluated. As predicted, the overwhelming factor in maintaining stability in the optics is temperature. The absolute value of the temperature is not as important as the changes in temperature over time. If an isothermal environment is maintained, then the system reaches equilibrium and there is little or no drift in both the monochromator and analyzer crystals. Imaging at the NSLS presents a unique problem since the ring current in the storage ring decreases slowly but predictably with time. The intensity of the incident x-rays on the first

monochromator crystal will decrease in proportion with the ring current, causing the temperature of the first crystal to decrease with time. If no active feedback controls are placed on the crystal system, the first analyzer crystal will contract over time, slowly changing the d spacing and diffracted energy. A change in the Bragg angle on the first crystal will change the position of the beam on the second crystal, reducing the diffracted monochromatic photon flux emitted from the second crystal. This will both reduce the intensity of the x-ray beam incident on the analyzer crystal and change the position of the x-ray beam, resulting in analyzer drift.

The effect is most clearly demonstrated during a cold startup of the beamline, where all of the beamline components have been at room temperature for at least 24 hours with the x-ray shutters closed. A series of stability tests were performed to test how the analyzer drifts within the first 100 minutes after startup, with the practical purpose of determining how long it takes the system to reach equilibrium. Short term stability testing of the analyzer was accomplished by aligning the system immediately after enabling the x-ray shutters and resetting the analyzer position to zero. The analyzer was then scanned every 100 seconds over a range of -10 to 10 microradians with a theta increment of 0.2 microradians. Each rocking curve was subsequently analyzed to determine the center of gravity for each rocking curve, which was recorded as the peak position and recorded along with its corresponding analyzer position. Once the system was initially tuned and the experiment initiated, no further tuning or adjustments were made.

Two photon energies were selected for testing, 18 keV and 40 keV, with all other beamline parameters and aluminum filtration set to the levels used under normal imaging conditions. Higher energy x-rays are far more penetrating than lower energy x-rays, and require more

pre-monochromator filters to both reduce the flux to the desired level and attenuate lower energy x-rays that are present in the polychromatic synchrotron white beam. Increasing the amount of filtration increases the amount of absorption that occurs before the x-rays enter the monochromator, thus reducing the heat load on the first monochromator crystal. With the addition of a water cooled heatsink to remove the heat generated from x-ray absorption occurring in the filter assembly, the crystals experience less thermal effects from the synchrotron white beam. The combination of reducing the angular change per degree Celsius at higher energies and the reduction of heat load on the monochromator by increased filtration leads to a proportional increase in stability with increasing beam energy.

Stability experiments conducted from a cold startup of the beamline demonstrate this effect, with the analyzer drift closely following the decrease in ring current. The current theory hypothesizes that the powerful incident synchrotron white beam almost instantly deep heats the first monochromator crystal, quickly reaching a maximum temperature. As the ring current dissipates with time, the temperature slowly decreases, resulting in drift. The system eventually heats up the surrounding ambient air and system components, causing the amount of drift per unit time to stabilize. The increased amount of filtration at 40 keV helps to reduce the effects of thermal load, decreasing the amount of time for the system to reach thermal equilibrium. Once the beamline has been in continuous operation for 5-7 hours, the effects of heat load on each of the crystals are minimized and the beamline becomes ultra-stable with little to no analyzer drift.

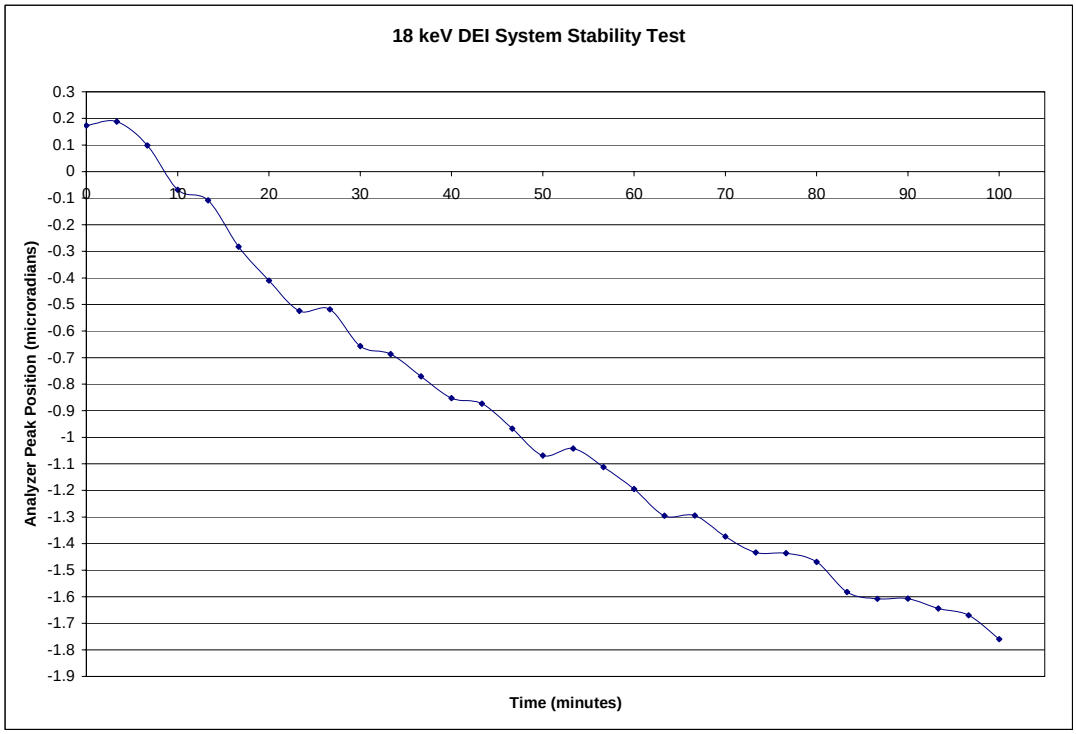

FIGURE 9.5: 18 keV system stability test

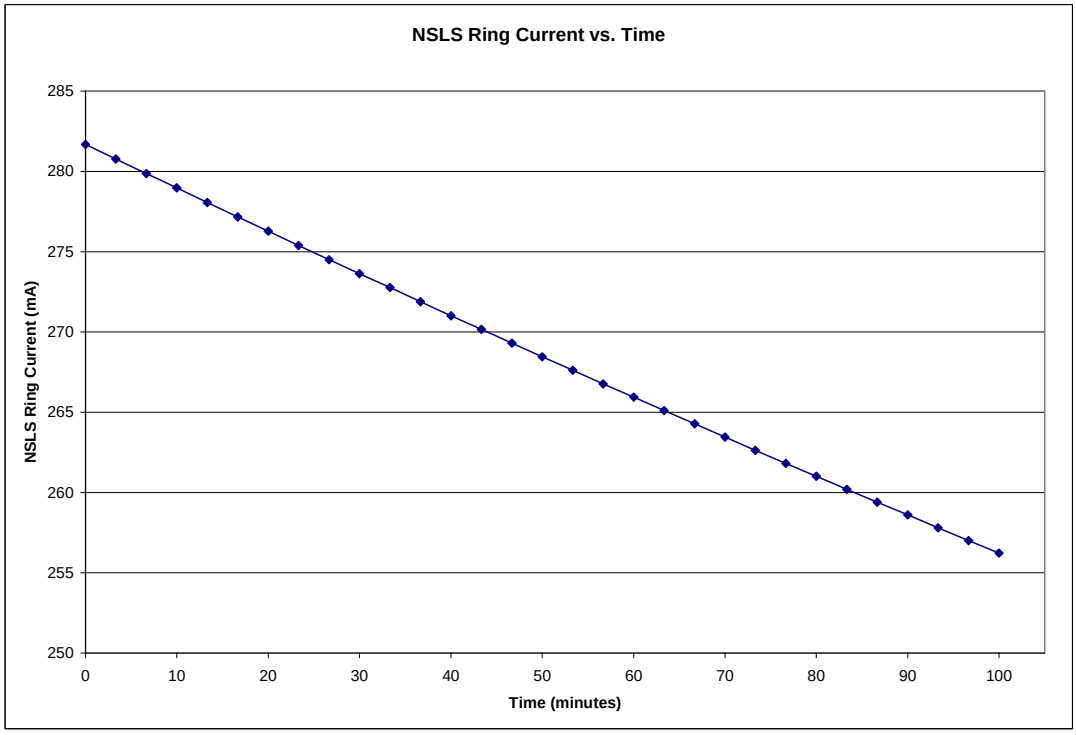

FIGURE 9.6: NSLS x-ray ring current during 18 keV stability tests

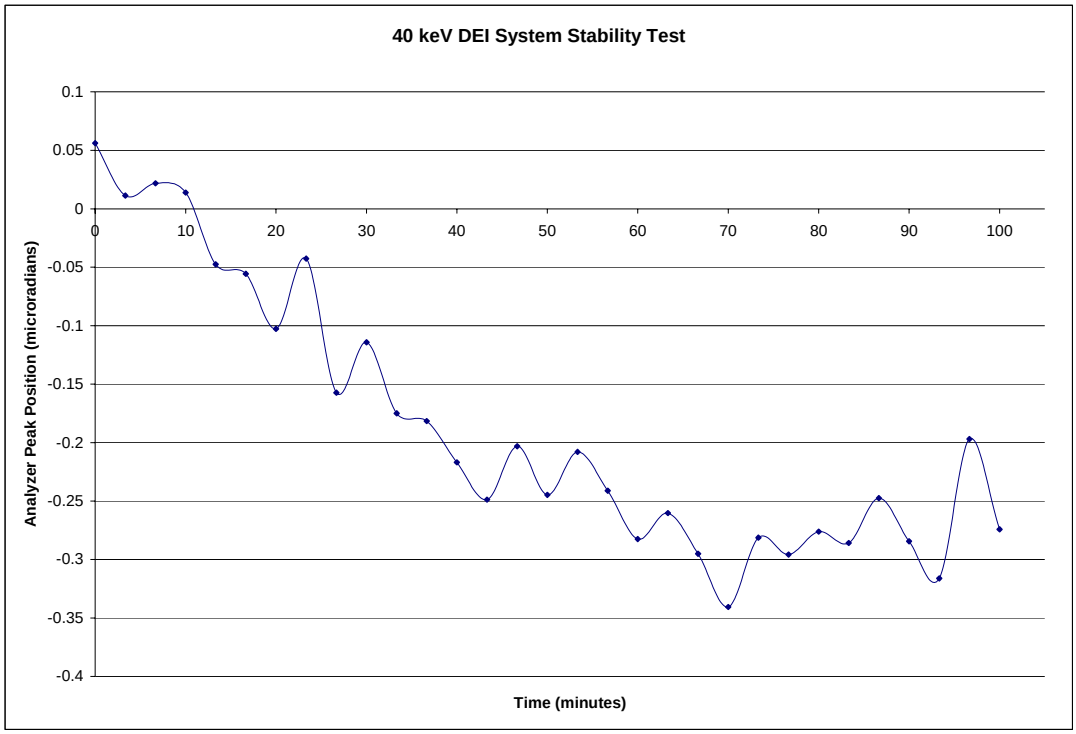

FIGURE 9.7: 40 keV DEI system stability test

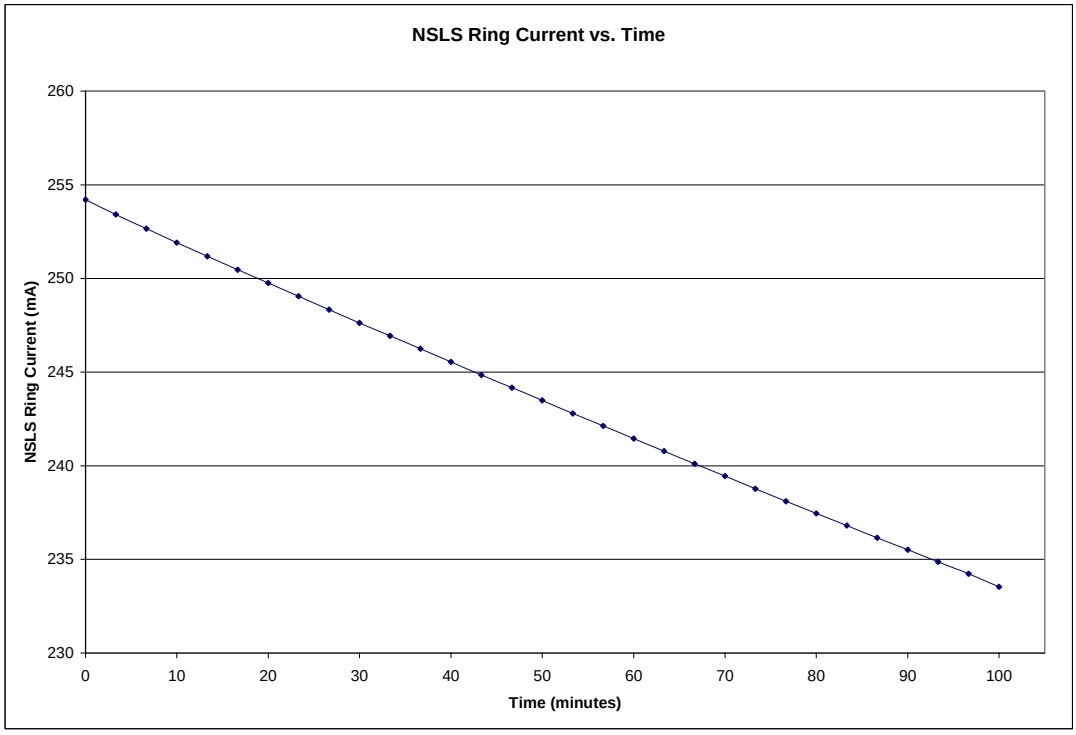

FIGURE 9.8: NSLS x-ray ring current during 40 keV stability tests

The results of this experiment clearly demonstrate that drift in the optics can be controlled by keeping the crystals in the optics isothermal, which can be achieved on both synchrotron and non-synchrotron based DEI systems using a precision heating system to maintain constant temperature. Through a systematic engineering analysis, the problem of analyzer/monochromator instability has been reduced from a fundamental limitation to a minor annoyance. With further refinement, the problem can be removed entirely, allowing for the full utilization of all computed tomography based DEI and MIR methods.

Chapter 10: Reader Study Analysis of Mammography Phantoms to Determine Optimal Imaging Parameters for Diffraction Enhanced Imaging

10.1 Introduction

Diffraction Enhanced Imaging (DEI) is a radiographic method that obtains contrast from x-ray absorption, refraction, and ultra-small angle scattering (extinction contrast) (Chapman et al. 1997). Conventional radiography systems, both planar and computed tomography (CT), produce images based on the attenuation of x-rays as they pass through matter. Since x-ray absorption is based on electron density and mean atomic number, contrast is obtained based on attenuation differences in an object or patient. Interactions of x-ray photons with matter can provide for more structural information than just the number of photons removed from the incident beam. DEI incorporates a silicon analyzer crystal in the path of the x-ray beam that acts as an exquisitely sensitive angular filter, facilitating the measurement of x-ray refraction and ultra-small angle scatter. Objects possessing nominal absorption contrast, either due to the properties of the object or its local environment, may have high refraction and ultra-small angle scatter contrast.

DEI might have tremendous potential in breast imaging given that the structures of interest in breast tissue typically have low absorption contrast, especially in the early stages of disease (Chapman et al. 1998). Previous DEI studies of malignant breast tissues have indicated a substantial increase in visualization of spiculations in breast tumors when

compared with conventional mammography (Fiedler et al. 2004; Hasnah et al. 2002; Pisano et al. 2000; Chapman et al. 1998). Primary diagnostic structures of interest in the breast include calcifications, masses, and fibrils, all of which may have significant refraction and scatter signatures when compared to the surrounding adipose and glandular tissue. In order to properly investigate the utilization of DEI for mammography, the unique system parameters and configurations must be optimized to detect the features diagnostically important for breast imaging. An integral component of this research is to determine the potential decrease in radiation dose that can be achieved using absorption, refraction, and ultra-small angle scatter. The primary DEI imaging components that must be specified in order to design and construct a clinically useful mammography system are beam energy, analyzer crystal reflection, and position on the analyzer crystal rocking curve.

10.2 Experimental DEI Setup at the National Synchrotron Light Source

Experiments were carried out at the X-15A beamline at the National Synchrotron Light Source (NSLS), Brookhaven National Laboratory, Upton, New York. A complete description of the DEI system at the NSLS has been previously described by Zhong et al (Zhong et al. 2000). In order to understand the parameters being analyzed, a brief description of the system is in order. The x-ray ring at the NSLS is a 2.8 GeV synchrotron, capable of producing high flux x-rays from 10 to 60 keV. A double crystal silicon monochromator is used to select a particular energy from the incident x-ray beam. DEI images are obtained by placing a silicon analyzer crystal behind the object which is tuned to select a particular angle. The analyzer is an angular filter with a resolution on the order of tenths of microradians, which facilitates the measurement of x-ray refraction and ultra-small angle scatter. Tuning the analyzer to

different positions on its reflectivity curve selects discrete angles in the x-ray distribution, and some positions may provide useful information for object and lesion detection.

There are multiple crystal reflections that can be used in DEI, with the most promising being the Bragg [111] and Bragg [333] reflections (Zhong et al. 2000). DEI refraction contrast increases with the slope of the analyzer crystal rocking curve, with the Bragg [333] reflection having a much steeper slope than the Bragg [111] reflection. The Bragg [333] reflection provides superior contrast, but the number of x-ray photons that can be selected from the incident polychromatic x-ray beam by the crystal in the Bragg [333] reflection is roughly an order of magnitude less than the Bragg [111] reflection. Determining the relative difference in visualization between these reflections is an important factor in the design on a clinically based DEI system.

10.3 Application of Research to Non-Synchrotron Based Imaging

Conventional x-ray tubes use a cathode/anode configuration to produce x-rays, with the output spectrum and amplitude a function of the anode material, voltage, and amperage. Most mammography systems use an x-ray tube with a molybdenum target at voltages ranging from 28 to 32 kVp. This configuration produces a polychromatic, diverging x-ray beam with an energy spectrum centered around the K_α of molybdenum, 18 keV. Absorption based x-ray systems require these relatively low energy x-rays for imaging soft tissue. While 18 keV x-rays provide great contrast in soft tissues, one obvious drawback is the increased patient absorbed dose associated with lower energy x-rays. Early DEI breast imaging studies were based on an x-ray energy comparable to conventional mammography systems (Chapman et al. 1998). While this methodology may have potential utility in measuring x-ray absorption,

it does not adequately address the advantages of the additional DEI contrast mechanisms of refraction and ultra-small angle scatter.

There are several image processing methods that can be applied to DEI, including the creation of apparent absorption and refraction images (Chapman et al. 1997). Another evolving DEI based image processing method is Multiple Image Radiography (MIR), which is a more accurate and detailed separation of the contrast components. Preliminary studies using MIR have demonstrated that this method is capable of operating at low photon count levels, and has potential use with conventional x-ray sources (Wernick et al. 2003). Several groups working with DEI are in the process of applying the DEI method to CT, which combines the additional contrast mechanisms of DEI with spatial resolving capability of CT (Dilmanian et al. 2000; Fiedler et al. 2004). While this study focuses on planar imaging, the system parameters for planar imaging can also be applied to both synchrotron and non-synchrotron-based CT applications.

The experiments that will be described in this paper involve the careful variation of the acquisition parameters during the imaging of standard mammography phantoms. Images acquired for the study represent the raw image data acquired at each system configuration, without any secondary image processing. Expert readers scored the visibility of the known phantom features under all experimental conditions in order to assist in the specifications of an ideal DEI mammography unit.

10.4 Methods

From both an engineering and medical perspective, one of the most important system parameters is beam energy. In order to gain an understanding of how structural visualization changes as a function of energy in DEI the following energies were chosen for the study: 18

keV, 25 keV, 30 keV, and 40 keV. Selection of the desired energy from the incident synchrotron beam was accomplished by tuning the monochromator to the appropriate Bragg angle for the desired wavelength.

While there may be diagnostically valuable information across the entire analyzer crystal rocking curve, three representative points were chosen for analysis. The –1/2 Darwin Width (DW), peak, and +1/2 DW positions were selected for each beam energy/crystal reflection combination. A corresponding synchrotron radiograph was obtained for comparison.

Standardized breast imaging phantoms were used in this study to simulate the structural characteristics of breast tissue and breast cancer. Initial efforts involved actual breast tissue specimens, but the variation present in biological tissues and subjective evaluation of malignant features made the use of phantoms more appropriate for the current study. Since DEI is capable of obtaining contrast from multiple mechanisms, phantoms were selected with features amenable to each. A Contrast-Detail (CD) phantom (Sunnybrook and Women's Research Institute, Toronto, Ontario, Canada) made of Lucite with a series of circular indentions of varying diameter and depth machined into the surface was selected. The variation in diameter and depth creates a gradient useful in assessing contrast and spatial resolution. Deeper indentations result in an increased difference in attenuation, and therefore increased contrast. The circular edges of the indentions provide an interface conducive to the refraction of x-rays. With a known radius and height, the volume of each cylinder was calculated to determine the total visible volume. Examples of the CD phantom at 18 keV are presented in Figure 10.1, and at 30 keV in Figure 10.2.

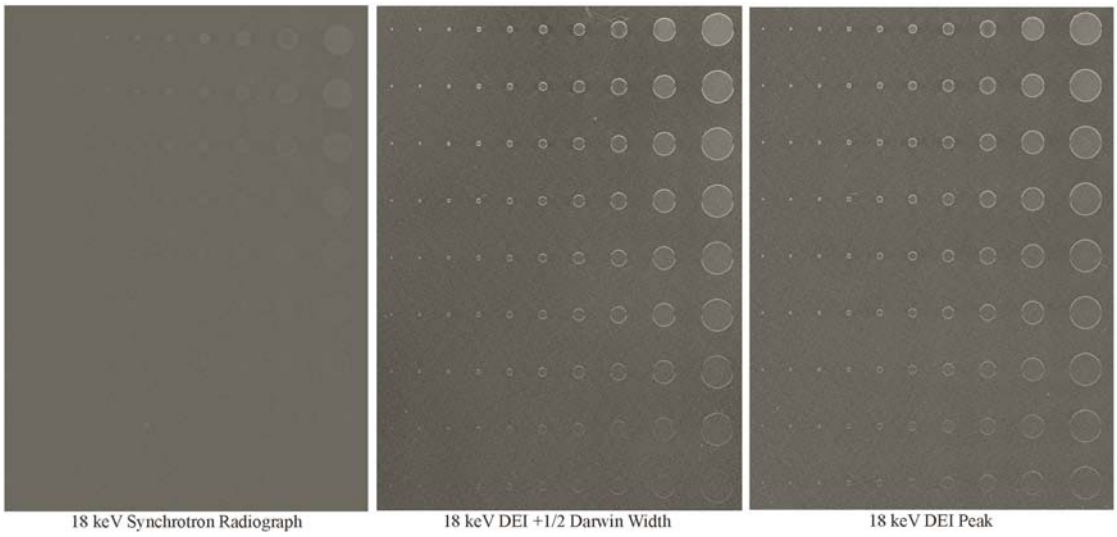

FIGURE 10.1: Examples of the Contrast-Detail (CD) phantom acquired at 18 keV. From left to right, the Figure illustrates an 18 keV synchrotron radiograph, 18 keV DEI image acquired in the +1/2 Darwin Width (DW) analyzer crystal position, and an 18 keV DEI image acquired at the peak analyzer crystal position. The crystal reflection used in the DEI examples is the Bragg [333] reflection.

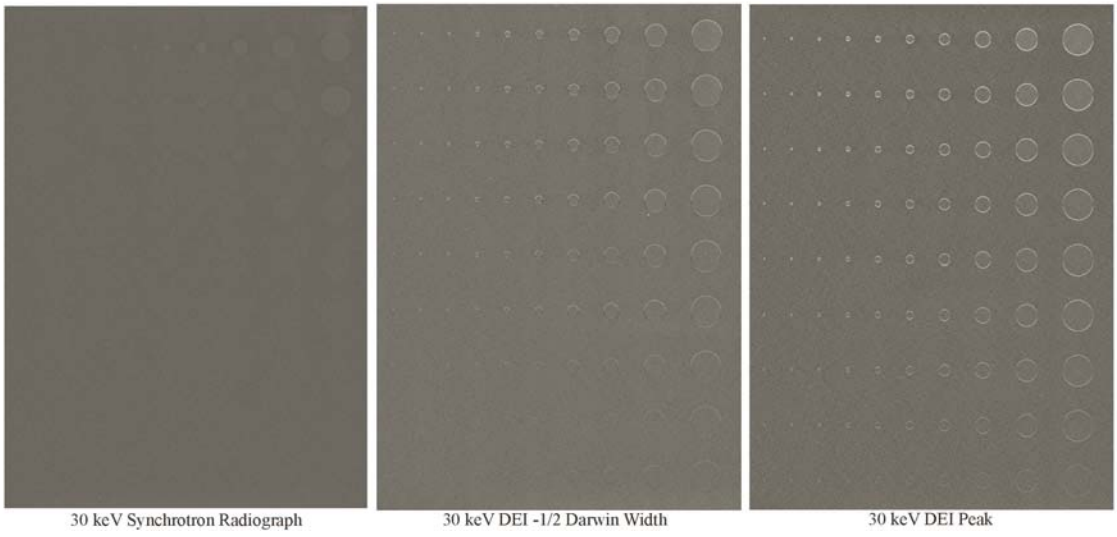

FIGURE 10.2: Examples of the Contrast-Detail (CD) phantom acquired at 30 keV. The Figure illustrates a 30 keV synchrotron radiograph, 30 keV DEI image acquired in the -1/2 Darwin Width (DW) analyzer crystal position, and a 30 keV DEI image acquired at the peak analyzer crystal position. The crystal reflection used in the DEI examples is the Bragg [333] reflection. Note the reduction in contrast in the 30 keV synchrotron radiograph when compared to the 18 keV synchrotron radiograph.

The second phantom was designed for the International Digital Mammography Development Group (IDMDG) to test digital mammography systems. Specifically this phantom was developed for the Digital Mammography Imaging Screening Trial (DMIST) and is known as MISTY (Sunnybrook and Women's Research Institute, Toronto, Ontario, Canada). The MISTY phantom contains a variety of regions that can be used to quantify mammographic image quality. Structurally the phantom is composed of polymethylmethacrylate (PMMA) with a mercury-intensified overlay containing several high resolution details that can be used to quantify system contrast and resolution. Three regions from this phantom were selected for use in the reader study and are presented in Figure 10.3.

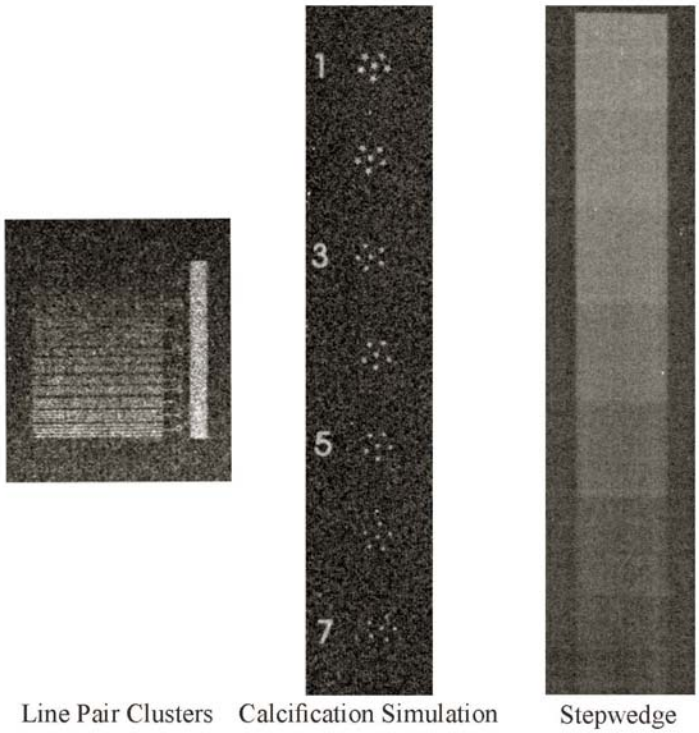

FIGURE 10.3: MISTY phantom regions of interest acquired at 30 keV, Bragg [333], in the peak analyzer crystal position. The images from left to right illustrate the line pair clusters, calcification simulation, and stepwedge. The calcification simulation was inverted for use in the reader study.

The first region is a series of line pairs clusters, each cluster containing 4 lines, with the distance between the lines decreasing until they can no longer be resolved. The second region is a series of star clusters, which simulate calcifications in breast tissue. A column of seven clusters, each containing six stars, was used with each cluster of stars having one star with a missing point. As resolution and contrast decreases, the stars can no longer be visualized and appear only as specks. Absorption contrast is measured using the third region, a stepwedge with 6 well defined interfaces.

All DEI images were acquired using a Fuji BAS2500 Image Plate Reader and Fuji HR V image plates (Fuji Medical Systems, Stamford, CT). The image plates are flexible plastic sheets, approximately 0.5 mm thick, coated with a photostimulable phosphor combined with an organic binder. All images were scanned using a 50 μm pixel size and a 16-bit gray level. The surface dose used for image acquisition varied based on energy, but the same surface dose was used for both the radiograph and DEI images at each energy setting. A surface dose of 3.0 mGy was used for image acquired at 30 keV, 1.5 mGy for images acquired at 25 keV, and 0.2 mGy for images acquired at 40 keV.

The use of standardized phantoms combined with the dramatic differences between most of the DEI configurations indicated that two readers would be sufficient to achieve an appropriate level of statistical power. One expert breast imager and one medical physicist participated in the study (E.D.P, R.E.J). In order to optimize the viewing environment, the reader study was performed in a specially designed darkroom using a 5 megapixel CRT monitor with a peak luminance of 500 cd/m^2 (Clinton Electronics, Rockford, IL). Readers were allowed to adjust the gray scale of each image and were provided a magnifying glass for maximum visualization.

The ability to visualize the entire circumference of a lesion has diagnostic significance in mammography, an example being the difference between a benign fibroadenoma with well circumscribed borders and a potentially malignant mass with less well-defined borders with or without spiculations. Additionally, visualization of calcifications and their morphology can provide insight into underlying pathology. Questions reflecting the diagnostic application to clinical mammography were integral to the reader study design, separating the task into distinct confidence levels where appropriate.

In determining which factors give the highest performance, eight performance measurements were established:

1. The volume of the circles for which the entire circumference can be seen in the CD phantom;
2. The volume of the circles for which at least half of the circumference is visible in the CD phantom;
3. The volume of the circles for which any part of the circumference is visible in the CD phantom;
4. The number of line pair groups observed in the MISTY phantom;
5. The number of stars that are visible in the calcification simulation of the MISTY phantom;
6. The last cluster number with all points seen in the calcification simulation of the MISTY phantom;
7. The number of specs seen in the calcification simulation of the MISTY phantom;
8. The number of clearly defined sections in the stepwedge of the MISTY phantom.

In order to facilitate the codification of the data in the images, a graphical depiction of each phantom with the corresponding performance task was provided to each reader to score the images. For the CD phantom, the reader was asked to indicate which circles were visible in each row and column of the image. To assess the MISTY phantom line pair region, the reader was asked to determine the highest cluster where all four lines could be clearly visualized. Scoring of the calcification simulation involved first counting the total number of stars that could be visualized, then counting the number of star points seen in each cluster out of a possible 29 points. In addition, the reader was asked to count the total number of specks that could be visualized. For the stepwedge region of interest, the reader was asked to mark which of the 6 interfaces could be clearly visualized. The order of image presentation was randomized for each reader for scoring.

A multi-way analysis of variance was used to fit all eight outcomes. Included in the analysis were all interactions among beam energy, crystal reflection, curve position, and reader. Box-Cox transformations were applied to some of the outcomes to ensure the validity of normality assumption. Since multiple outcomes were considered when comparing all the factors, a Bonferroni test was used to adjust the overall Type I error by setting 0.05/8 (0.00625) as the significance level. At this significance level, we used the Tukey test to compare the difference in performance among the combinations of all the factors.

10.5 Results

CD Phantom

For volume of the circles with any part of the circumference visible, there is no significant difference between the two readers (p-value=0.0185) and among different energy levels (p-

value=0.0176). However, both crystal reflection and rocking curve position, as well as their interactions, are significant (all three p-values<0.001). Tukey test analysis indicates that more volume could be seen with the Bragg [333] reflection. The radiograph has the least visible volume, and there is little difference among the -1/2 DW, +1/2 DW, and peak analyzer crystal positions.

When the outcome is the volume of the circles with at least half of the circumference visible, the main effects of all the factors are significant with p-values less than 0.001. Tukey test analysis indicates that 25 keV performed best, and that both 25 kev and 30 keV produce more visible volume than 18 keV and 40 keV. The data indicates that there is a significant interaction between crystal reflection and analyzer position (p-value<0.001). The combination of the Bragg [333] reflection and peak analyzer position produces the most visible volume, although there is not enough evidence to support that it performs better than the combinations Bragg [333], +1/2 DW and Bragg [333], –1/2 DW positions. The synchrotron radiograph produced the least visible volume.

For the volume of the circles with the entire circumference visible, only the main effects of reader, beam energy and rocking curve position are significant with p-values being less than 0.001, equal to 0.0027, and less than 0.001 respectively. Tukey test analysis did not find a difference among all the levels in beam energy, but trends in the data indicate that 25 keV performs better than 30 keV, and the latter performed better than both 40kev and 18kev. As with the other performance measurements, the synchrotron radiograph produced the least visible volume.

MISTY Phantom

Analysis of the line pair groups indicate that the main effects of beam energy, crystal reflection and analyzer rocking curve position are significant with all p-values less than 0.001. Moreover, there appears to be significant interactions between the crystal reflection and rocking curve position (p-value<0.001). The data indicates that the combinations of 18 keV, Bragg [333], in the peak analyzer position or 25 keV, Bragg [333], in the peak or +1/2 DW analyzer position performed well. The best performance for the line pair region is 30 keV, Bragg [333], at a rocking curve position of +1/2 DW.

Artifacts were present in many of the star cluster images generated by using a phantom designed for diverging x-rays in a system with a highly collimated x-ray beam. The data is presented for completeness and to demonstrate how the overall structural design of conventional phantoms can affect visualization. Analysis of the number of stars visualized indicates that only beam energy is significant, with a p-value of 0.0026. Test results indicate that 25 keV is the best choice, but not significantly different from 30 keV. None of the factors were significant for the last cluster number with all points seen. Data from the number of specks seen indicate that the best combinations are 18 keV and Bragg [111], 18 keV and Bragg[333], as well as 30 keV with either the Bragg [111] or [333] reflection.

For the stepwedge region, there appears to be a significant difference among the difference levels in beam energy and the different rocking curve positions. The data indicates that the beam energies of 18 keV, 25 keV, and 30 keV are roughly equivalent, but all perform better than images acquired at 40 keV. The performance results for the rocking curve position indicate that the positions of -1/2 DW, peak, and +1/2 DW are equivalent and equal to the performance of the synchrotron radiograph.

Analysis of all performance measurements indicate that the optimal DEI system configuration is 25 or 30 keV, using the Bragg [333] reflection in either the -1/2 DW or peak analyzer crystal position. A summary of the reader study data is presented in Tables 10.1-10.3.

	CD Phantom Entire Circumference	CD Phantom Half Circumference	CD Phantom Visualization Only	Misty Phantom Line Pairs	IDMDG Phantom Stars	IDMDG Phantom Star Points	IDMDG Phantom Specks	IDMDG Stepwedge
18	127.96 ± 9.58	210.49 ± 68.98	241.43 ± 19.76	1.625 ± 1.147	2 ± 3.347	0.125 ± 0.341	38.562 ± 5.215	4.562 ± 0.964
25	185.63 ± 73.62	232.04 ± 39.16	247.96 ± 9.66	1.937 ± 1.181	5.187 ± 6.295	0.375 ± 0.719	41.875 ± 0.341	4.312 ± 1.014
30	169.36 ± 96.80	227.56 ± 48.73	245.16 ± 13.87	1.812 ± 1.223	3 ± 3.483	2.687 ± 10.486	39.400 ± 4.702	4.687 ± 1.250
40	134.24 ± 107.30	198.31 ± 67.93	237.85 ± 23.65	0.375 ± 0.619	0.375 ± 0.885	0 ± 0	14.937 ± 12.615	0.562 ± 1.093

TABLE 10.1: Summary of reader study data with respect to x-ray beam energy

	CD Phantom Entire Circumference	CD Phantom Half Circumference	CD Phantom Visualization Only	Misty Phantom Line Pairs	IDMDG Phantom Stars	IDMDG Phantom Star Points	IDMDG Phantom Specks	IDMDG Stepwedge
111	150.96 ± 95.99	214.98 ± 46.73	242.89 ± 10.74	0.969 ± 0.897	2.031 ± 3.605	1.437 ± 7.414	33.935 ± 13.394	3.687 ± 2.086
333	157.64 ± 102.42	219.22 ± 67.90	243.31 ± 22.64	1.906 ± 1.328	3.250 ± 4.833	0.156 ± 0.448	33.281 ± 13.056	3.375 ± 1.996

TABLE 10.2: Summary of reader study data with respect to crystal reflection

	CD Phantom Entire Circumference	CD Phantom Half Circumference	CD Phantom Visualization Only	IDMDG Phantom Line Pairs	IDMDG Phantom Stars	IDMDG Phantom Star Points	IDMDG Phantom Specks	IDMDG Stepwedge
Radiograph	110.61 ± 85.90	147.10 ± 72.48	218.21 ± 18.46	0.5 ± 0.632	0.375 ± 0.806	0 ± 0	29.375 ± 13.490	2.875 ± 1.668
Negative 1/2 DW	162.24 ± 104.75	241.13 ± 21.21	251.24 ± 5.32	1.687 ± 1.078	2.812 ± 4.037	2.750 ± 10.478	35.667 ± 9.155	3.937 ± 1.948
Positive 1/2 DW	165.51 ± 102.42	238.35 ± 32.28	252.28 ± 3.80	1.687 ± 1.250	3.187 ± 5.128	0.250 ± 0.577	31.187 ± 18.605	3.375 ± 2.094
Peak	178.83 ± 95.13	241.82 ± 18.43	250.67 ± 5.60	1.875 ± 1.360	4.187 ± 5.009	0.187 ± 0.403	38.312 ± 7.208	3.937 ± 2.351

TABLE 10.3: Summary of reader study data grouped according to rocking curve position

10.6 Discussion

With respect to beam energy, a clear trend is evident in the reader study data for both phantoms indicating that energies greater than 18 keV are optimal for DEI. Since absorption contrast decreases as $1/E^3$, soft tissue absorption contrast decreases rapidly with increased energy for conventional x-ray systems. The reader study results indicate that for higher beam energies the loss of information from absorption is compensated for by information from DEI-specific contrasts. For structures that are primarily refractive, DEI sensitivity is proportional to 1/E, with the potential for image acquisition in soft tissue at energies at or above 40 keV (Chapman et al. 1998). The rejection of scattered photons that contributes to extinction is energy independent, but the scattering intensity will decrease as energy

increases (Chapman et al. 1998). Since most key diagnostic structures in breast tissue are believed to have significant refractive and scatter properties, imaging at higher energies may be facilitated by moving away from absorption and focusing on refraction and ultra-small angle scatter contrast.

Increases in visualization for the Bragg [333] reflection are evident in the CD phantom, especially at higher performance levels. The Bragg [333] reflection was superior in the majority of performance measurements, but the difference between this reflection and the Bragg [111] is less than expected. While this may indicate that the Bragg [111] reflection is acceptable given the engineering considerations of flux, the more likely explanation is that the design of the phantoms was inappropriate for measuring contrast mechanisms that are based on x-ray refraction and extinction.

The same reasoning can be applied to the analyzer crystal position, in which the peak analyzer position was superior in the majority of performance measurements. Absorption contrast and resolution is going to be highest when the intensity of undeviated photons is greatest, which is at the peak of the analyzer rocking curve. Extinction effects also play a role at the peak position in that structures that scatter photons to the tails of the rocking curve will be eliminated, resulting in extra contrast. Since these phantoms were designed to test x-ray absorption based imaging systems, it is logical that the peak position would perform best in this type of study. Refraction contrast is not present at the peak of the rocking curve, and the generally equivalent or decreased performance of the -1/2 DW and +1/2 DW indicates the absence of structures in the phantom that are highly refractive.

This study was designed to gain insight into the effect each system component has on image quality, not on the image processing method that is most useful. As a first step in

narrowing the total imaging parameter space, an analysis of the raw data at each configuration is thus more appropriate than processing DEI image pairs to create apparent absorption and refraction images.

One of the most encouraging outcomes is the ability to use higher energy x-rays, potentially as high as 40 keV. The rapid decrease in the photoelectric effect at higher energies corresponds to a reduced number of photons absorbed in the patient, resulting in a dramatically reduced radiation dose. For the same number of photons reaching the detector (10^7 ph/cm^2), surface absorbed dose through 5 cm of water at 18 keV is 3.3 mGy, 0.045 mGy at 30 keV, and 0.016 mGy at 40 keV. This represents a 73 fold reduction in dose at 30 keV compared to 18 keV, and a 206 fold reduction at 40 keV. Since absorption increases with tissue thickness, this reduction in dose is even greater for thicker specimens.

10.7 Conclusion

As an initial step, this study has narrowed the potential parameter space and indicated that the optimal DEI configuration is different than what was initially proposed based on conventional mammography. Multiple studies demonstrating an improvement of soft tissue visualization in biological specimens when compared to conventional radiography have intensified efforts to develop the hardware necessary for a non-synchrotron based DEI system. There are numerous physics and engineering hurdles that must be overcome before a clinical system can be built. Changing parameters, such as beam energy, are easily accomplished at the NSLS, but making these changes with a more conventional high flux x-ray source would require fundamental changes in design.

With the general parameters defined, the development of a breast imaging phantom that better represents the additional contrast mechanisms of refraction and extinction will be necessary in the ongoing development of a DEI clinical prototype system.

Chapter 11: Multi-Parameter, Multi-Energy Measurements Of Breast Tissue Using Multiple Image Radiography

11.1 Introduction

Previous breast imaging studies using the Diffraction Enhanced Imaging method have demonstrated improvements in visualization when compared to conventional mammography, but none have addressed the possibility of extending the usable energy range and decreasing or eliminating the need for x-ray absorption. The underlying x-ray contrast mechanisms in breast tissue become critical when designing a non-synchrotron based DEI system, since absorption contrast in soft tissue decreases rapidly with increasing photon energy. Utilizing higher energy x-rays increases the efficiency of a DEI system by increasing the number of incident photons reaching the detector, and a reduction in x-ray absorption reduces both the surface and absorbed radiation dose. However, if absorption is a key contrast mechanisms for breast tissue visualization, then any DEI system must use lower energy x-rays in a range similar to conventional x-ray systems. This study seeks to determine if the features observed at 18 keV are conserved at higher energies, with the target energy being 60 keV.

In order to assess the energy dependence absorption, refraction, and scatter in breast tissue, four breast tissue specimens with characteristic features were imaged at multiple x-ray energies and processed using MIR to separate the individual contrast components. The energy range used in the study was determined based on the energies used in conventional molybdenum and tungsten x-ray tubes, 18 keV and 60 keV respectively. Beam energies of 25

keV, 30 keV, 40 keV, and 50 keV were also selected to closely follow the decrease in contrast for each MIR contrast mechanism

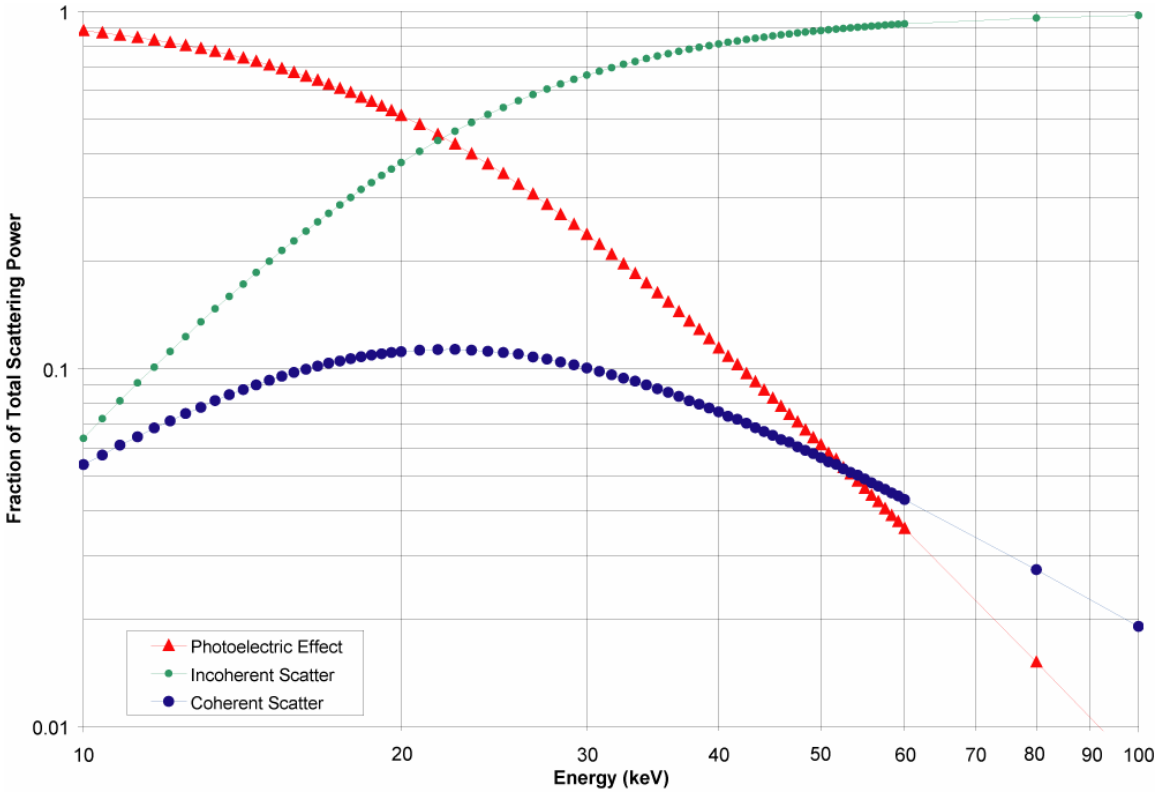

FIGURE 11.1: Contributions of absorption, incoherent scatter, and coherent scatter in breast tissue vs. energy

11.2 Materials and Methods

All MIR image sets and synchrotron radiographs were acquired using the X-15A beamline at the National Synchrotron Light Source, Brookhaven National Laboratory (Upton, NY). A Photonic Science VHR-150 x-ray camera (Robersbridge, East Sussex, UK) was used for image acquisition, with a FOV of 120mm x 80mm and a 30 micron pixel size.

The rapid decrease in the photoelectric effect in relation to x-ray refraction and scatter makes maintaining a constant surface dose challenging. For example, an image acquired using a surface dose optimized for x-ray absorption at 18 keV would be severely

overexposed at higher beam energies, such as 60 keV, due to a decrease in photon absorption. A balance was found by tuning the monochromator to the middle of the energy range to be used for MIR imaging, 40 keV, and selecting a surface dose to make the average exposure was approximately half the dynamic range of the detector. A surface dose of 350 mrad was selected for MIR and radiograph imaging at 18 keV, 25 keV, 30 keV, and 40 keV. The surface dose used at 50 keV and 60 keV was reduced due a sharp decrease in photon flux at those energies from a bending magnet x-ray source, with a surface dose of 20 mrad at 50 keV and 4 mrad at 60 keV. The full width at half maximum (FWHM) of the analyzer crystal rocking curve decreases as the energy increases. Refraction contrast is dominant in the shoulders of the rocking curve, requiring minor modifications in the sampling parameters for each energy. Twenty one images were acquired for each MIR set regardless of rocking curve width, and the angular range and theta increment were reduced at higher energies to adjust for a reduction in the FWHM.

Four breast specimens were selected for imaging at the National Synchrotron Light Source. MIR images acquired at 18 keV and 25 keV were acquired over a range of -5 to 5 microradians from the peak, sampled every 0.5 microradians. The sampling range was decreased for MIR imaging at 30 keV and 40 keV to ± 4 microradians, with a theta increment of 0.4 microradians. An angular range of ± 3 microradians was used at 50 keV with a theta increment of 0.3 microradians, and an angular range of ± 2 microradians with a theta increment of 0.2 microradians for MIR imaging at 60 keV. Corresponding synchrotron radiographs were acquired at each energy and dose. In addition, breast specimens were imaged using a General Electric Senographe 2000D (General Electric, Fairfield, CT).

The dose used for a single image at each energy was measured using thermolumiscent detectors to determine the mean glandular dose, distribution through the sample, and the flux required to generate the image.

11.3 Results

An example of a breast specimen imaged on a conventional radiography system is presented in Figure 11.2. This specimen was imaged in air using a GE Senographe 2000D with a 100 micron pixel resolution.

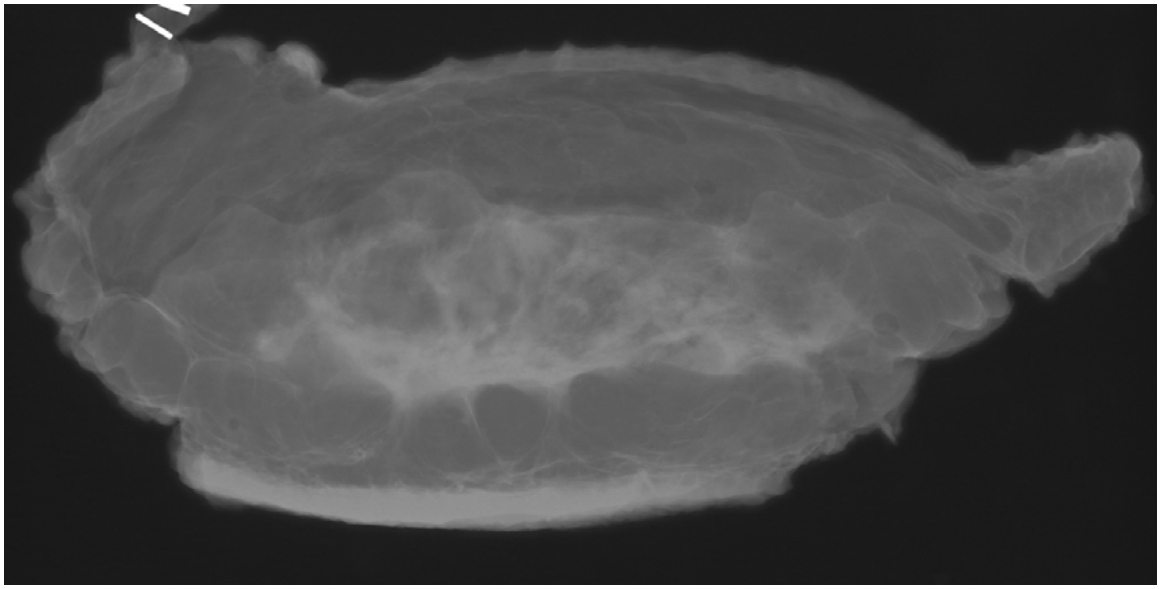

FIGURE 11.2: Digital Radiograph of a breast specimen

These images were acquired in air with a level of compression comparable to that used for imaging at the National Synchrotron Light Source. Synchrotron radiographs of the same sample at beam energies of 18 keV, 25 keV, 30 keV, 40 keV, 50 keV, and 60 keV are presented in Figure 11.3.

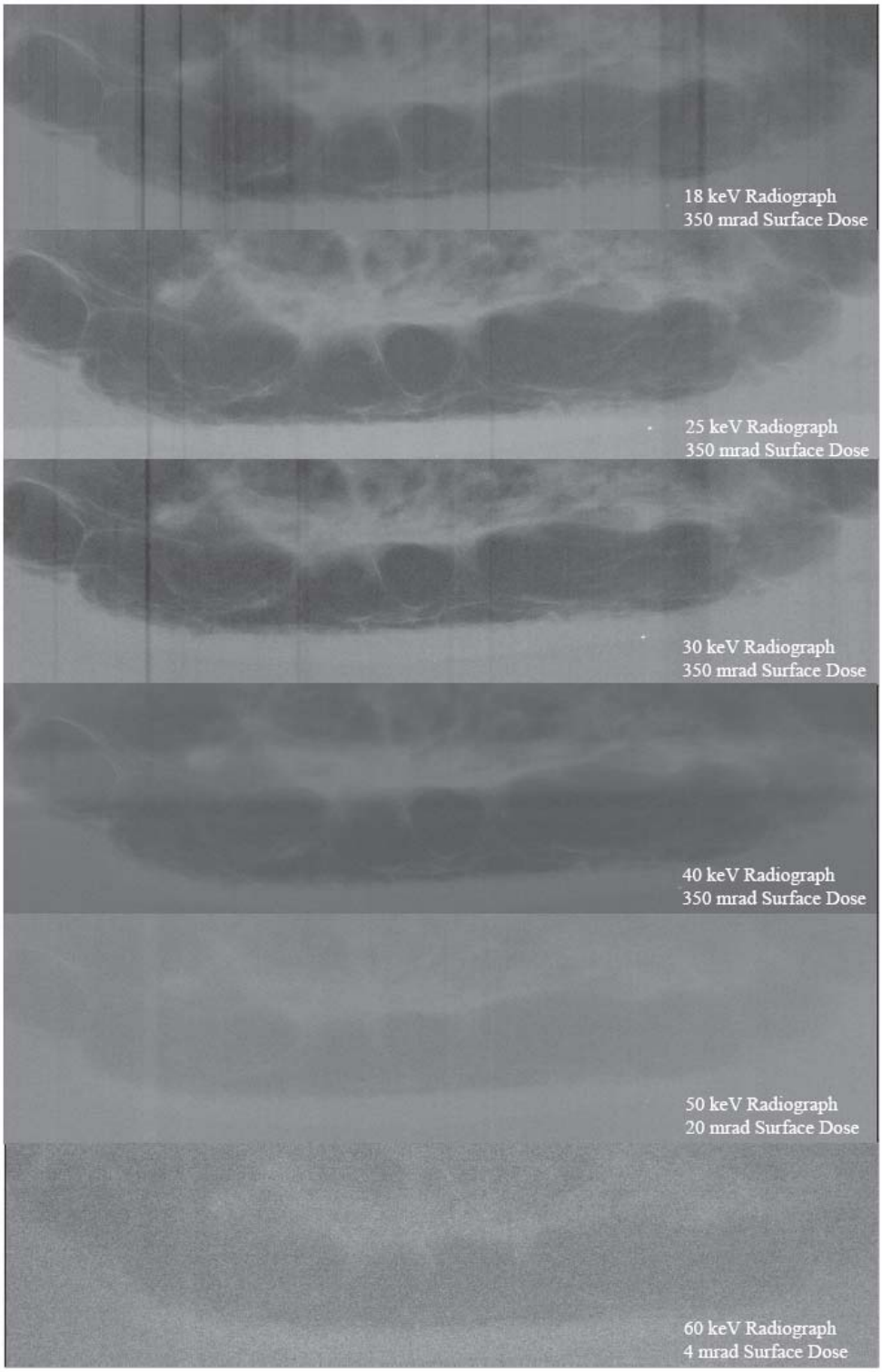

FIGURE 11.3: Synchrotron radiographs acquired at 18, 25, 30, 40, 50,and 60 keV

An example MIR set at each corresponding energy are presented in Figures 11.4-11.9.

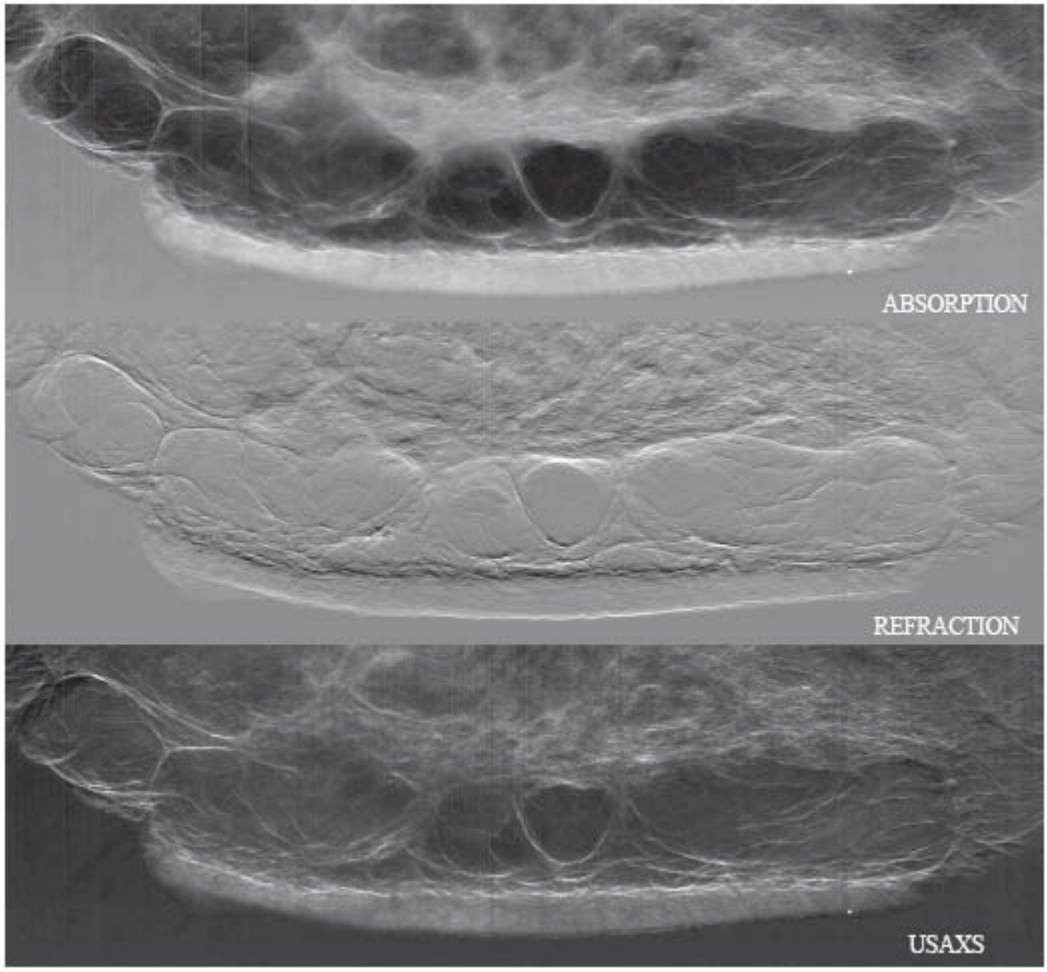

FIGURE 11.4 Breast specimen image using MIR at 18 keV with sampling parameters of ± 5 microradians with a theta increment of 0.5 microradians

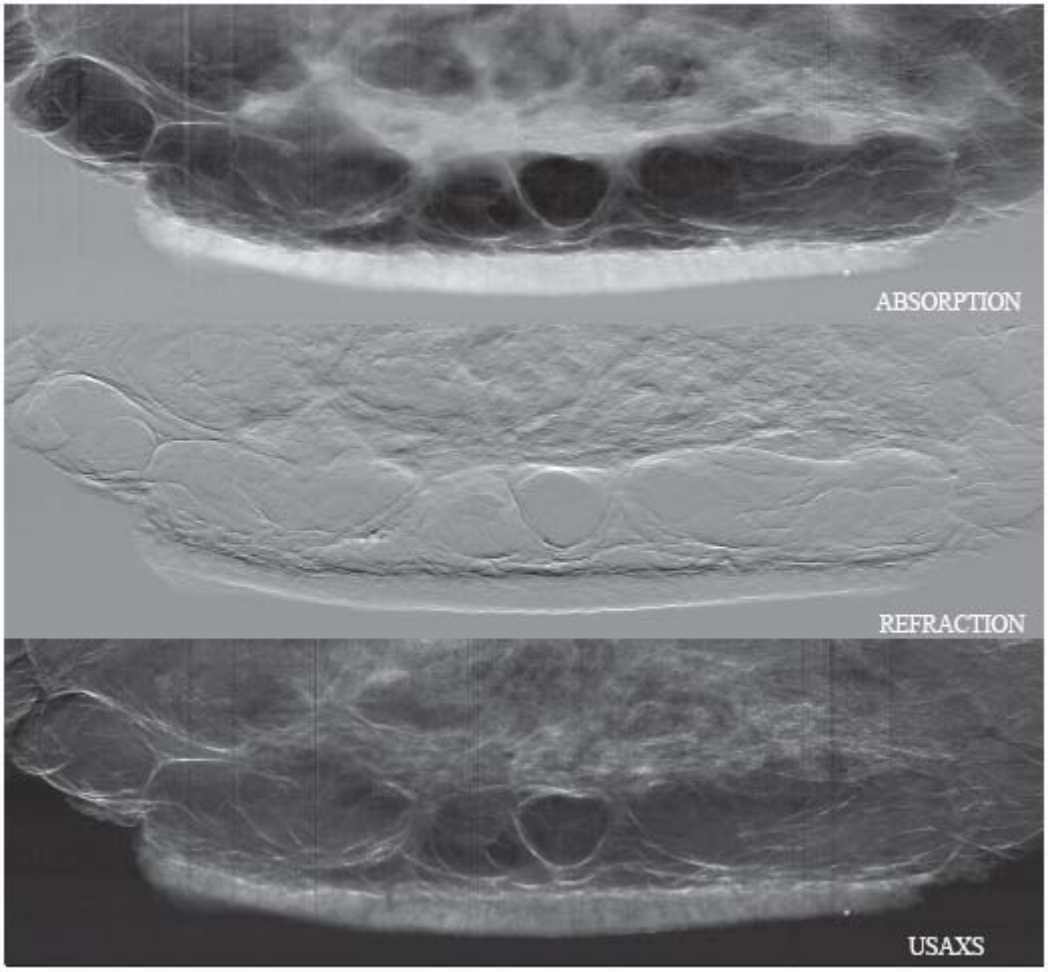

FIGURE 11.5 Breast specimen image using MIR at 25 keV with sampling parameters of ± 5 microradians with a theta increment of 0.5 microradians

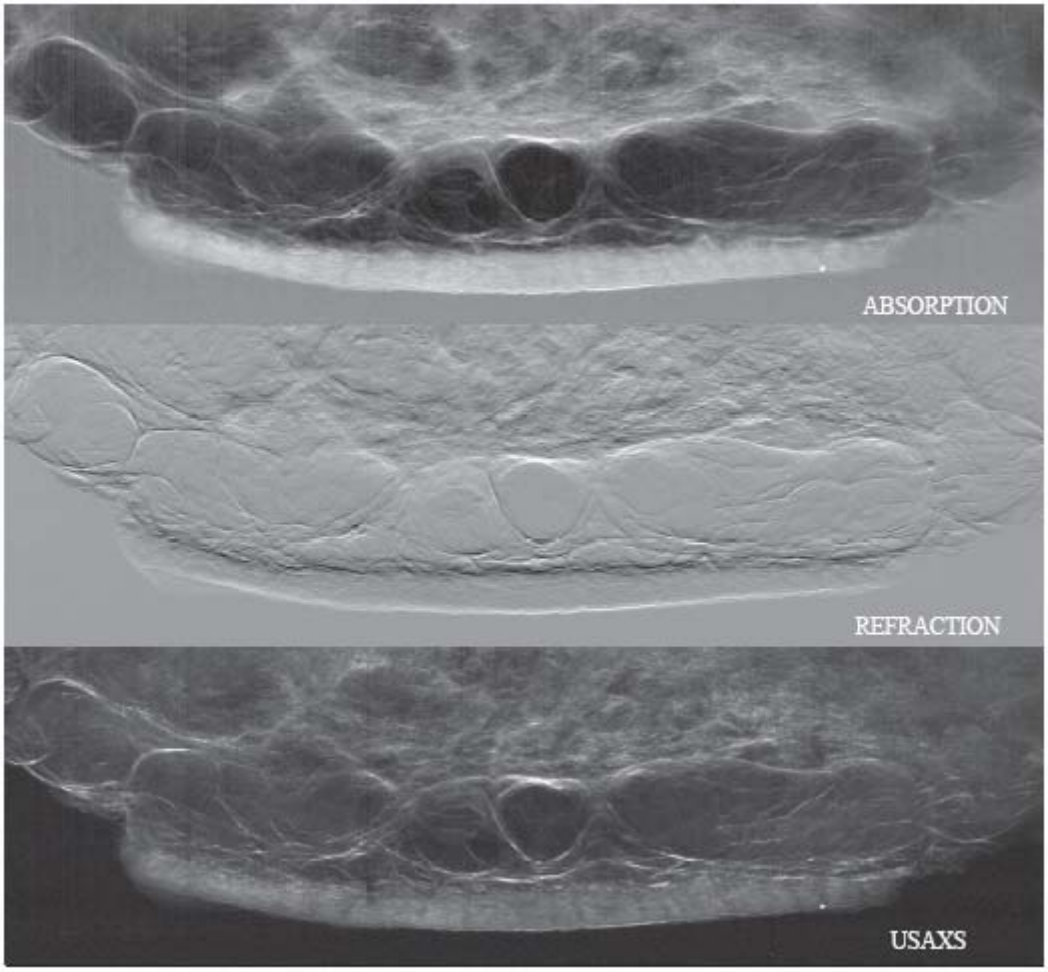

FIGURE 11.6 Breast specimen image using MIR at 30 keV with sampling parameters of ± 4 microradians with a theta increment of 0.4 microradians

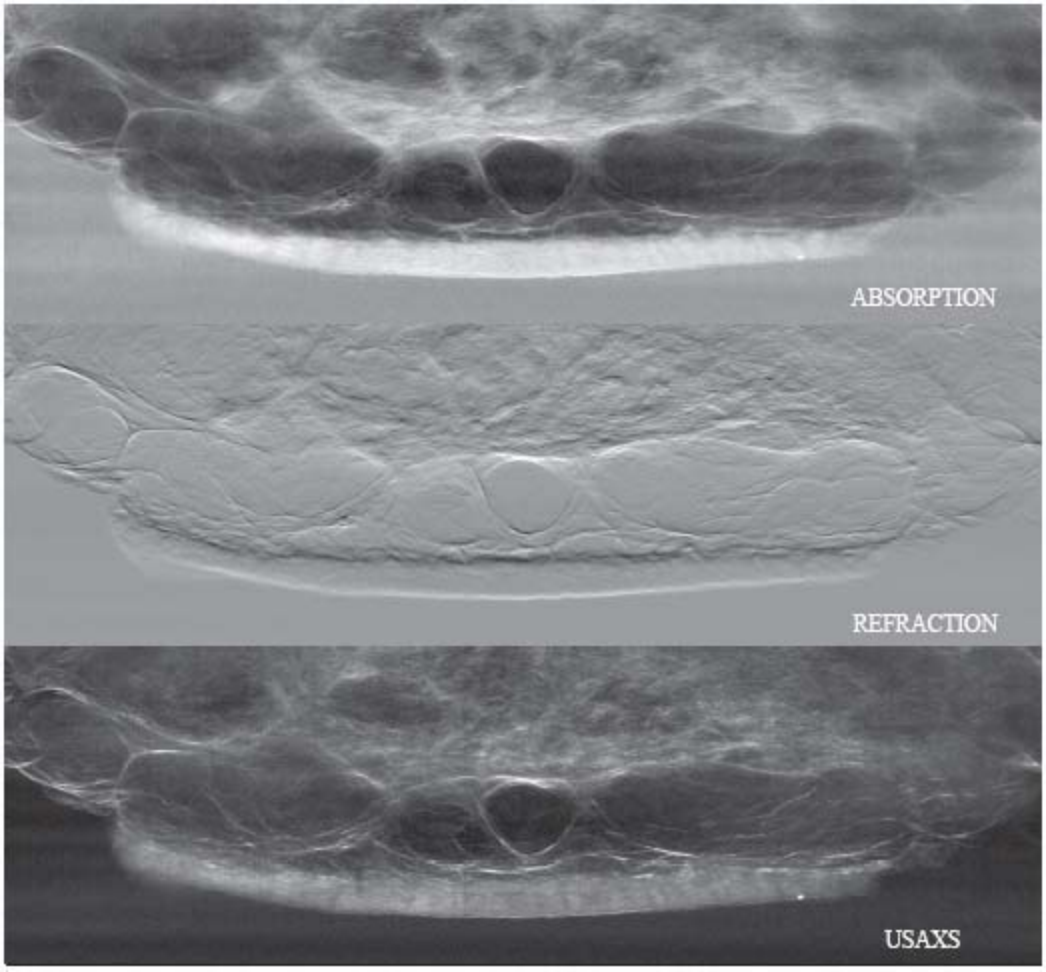

FIGURE 11.7 Breast specimen image using MIR at 40 keV with sampling parameters of ± 4 microradians with a theta increment of 0.4 microradians

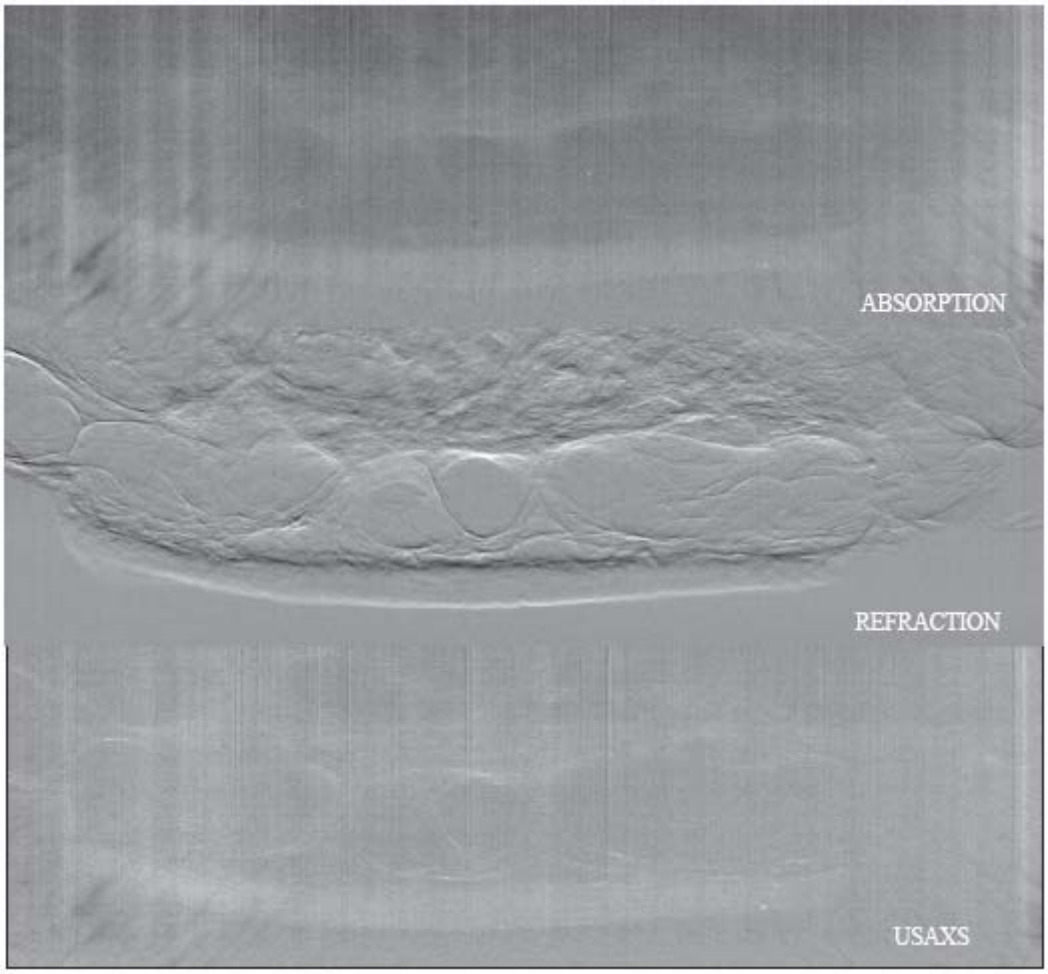

FIGURE 11.8 Breast specimen image using MIR at 50 keV with sampling parameters of ± 3 microradians with a theta increment of 0.3 microradians

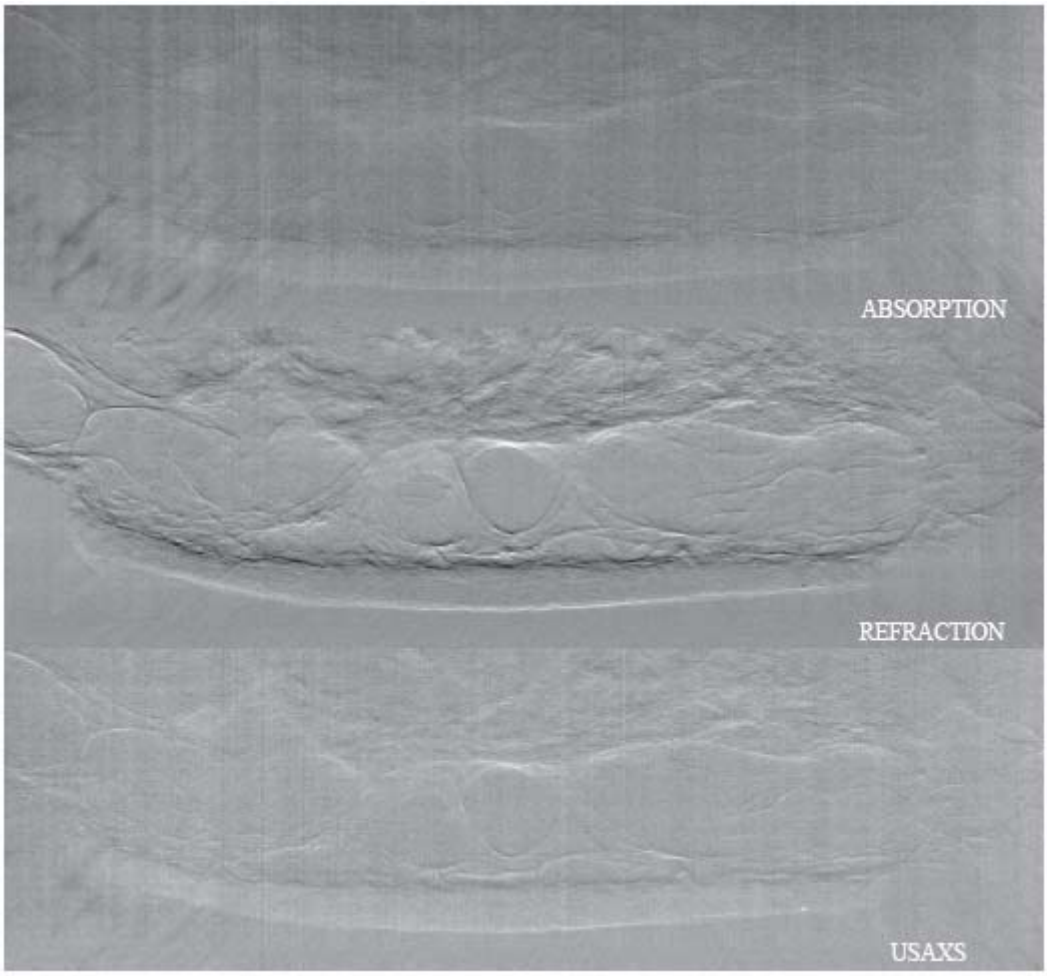

FIGURE 11.9 Breast specimen image using MIR at 60 keV with sampling parameters of ± 2 microradians with a theta increment of 0.2 microradians

The mean glandular dose and distribution was measured using thermoluminescent detectors and is presented for each corresponding energy in Figures 11.10-11.15.

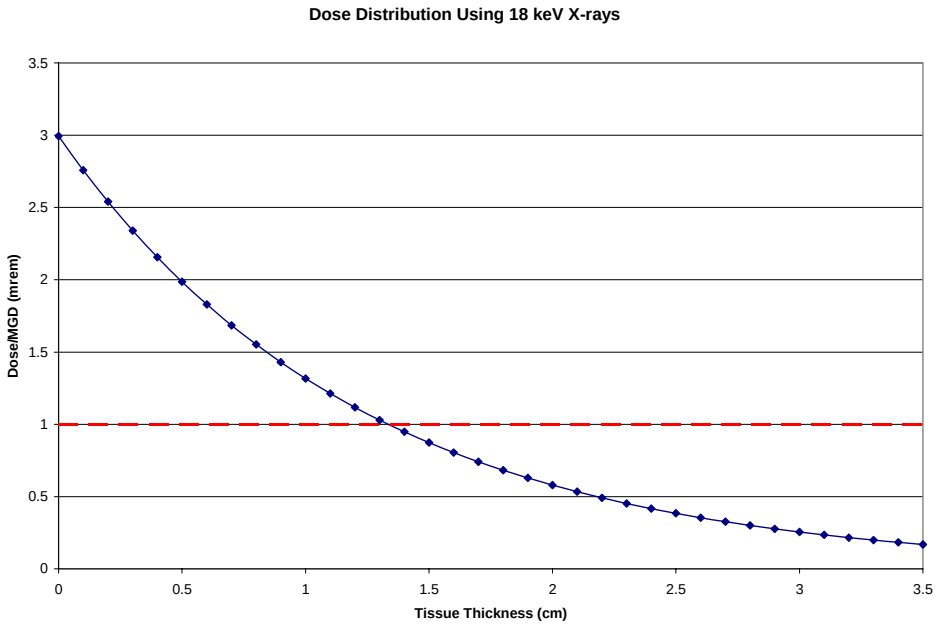

FIGURE 11.10: 18 keV dose distribution

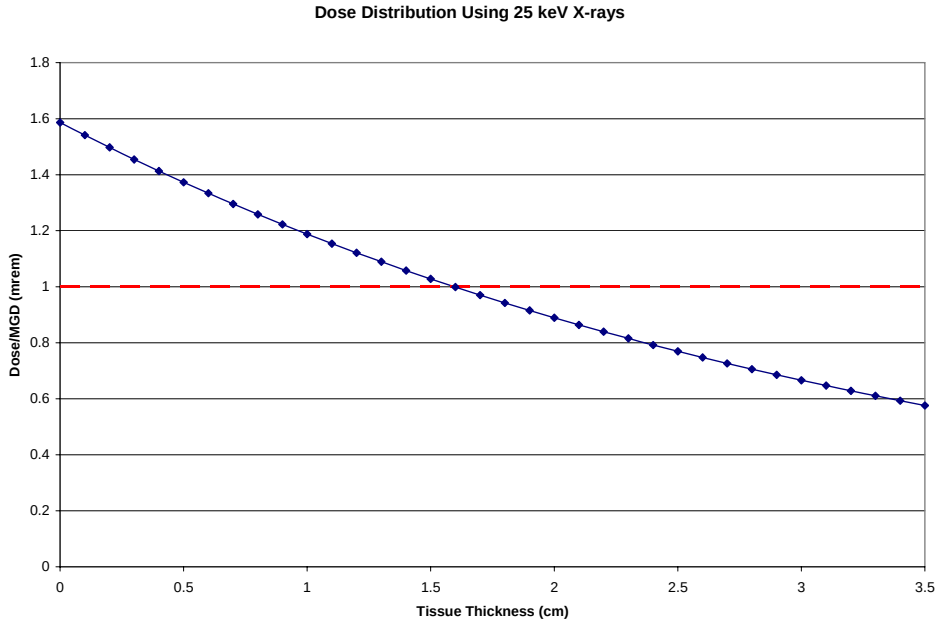

FIGURE 11.11 25 keV dose distribution

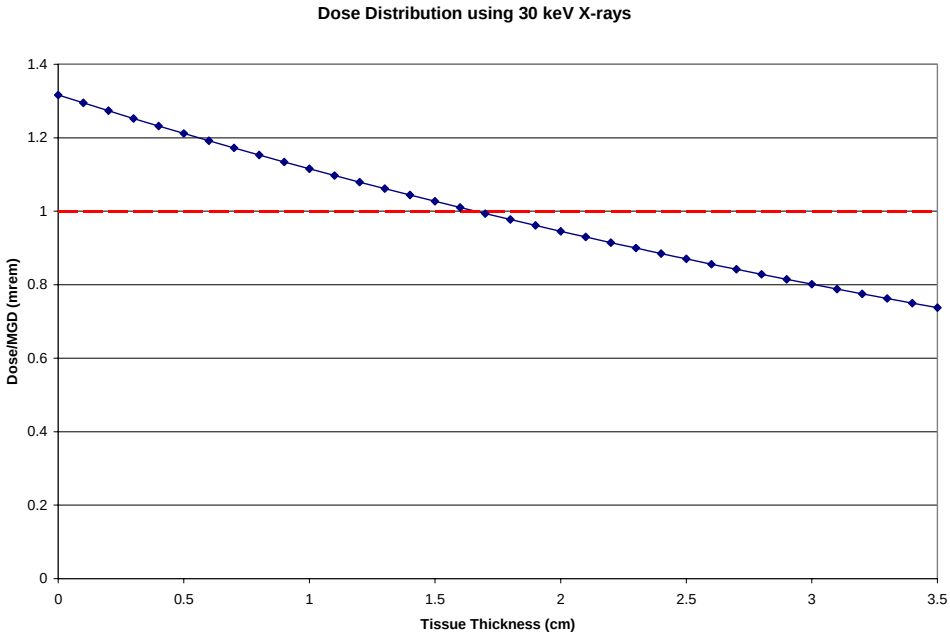

FIGURE 11.12 30 keV dose distribution

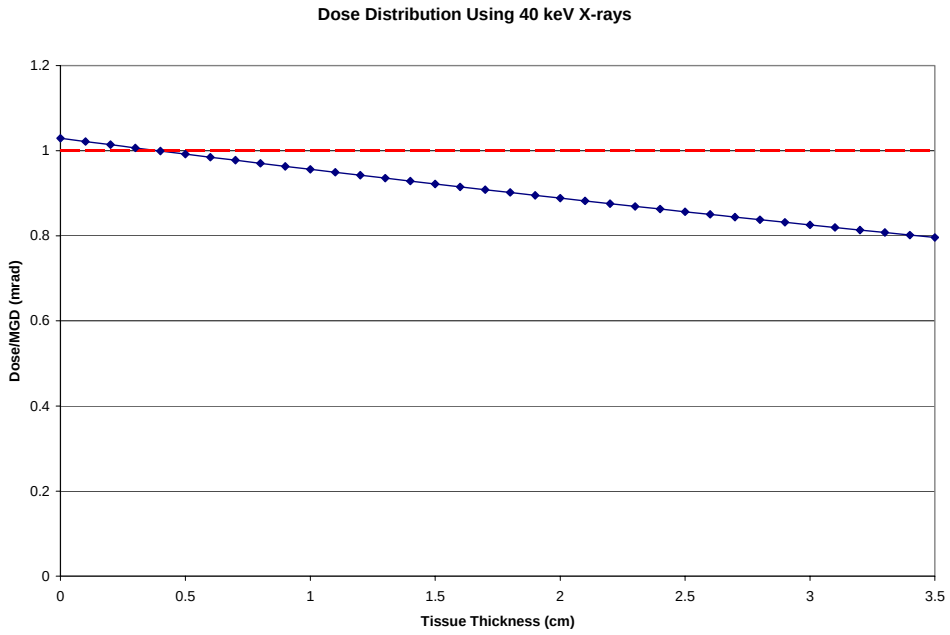

FIGURE 11.13 40 keV dose distribution

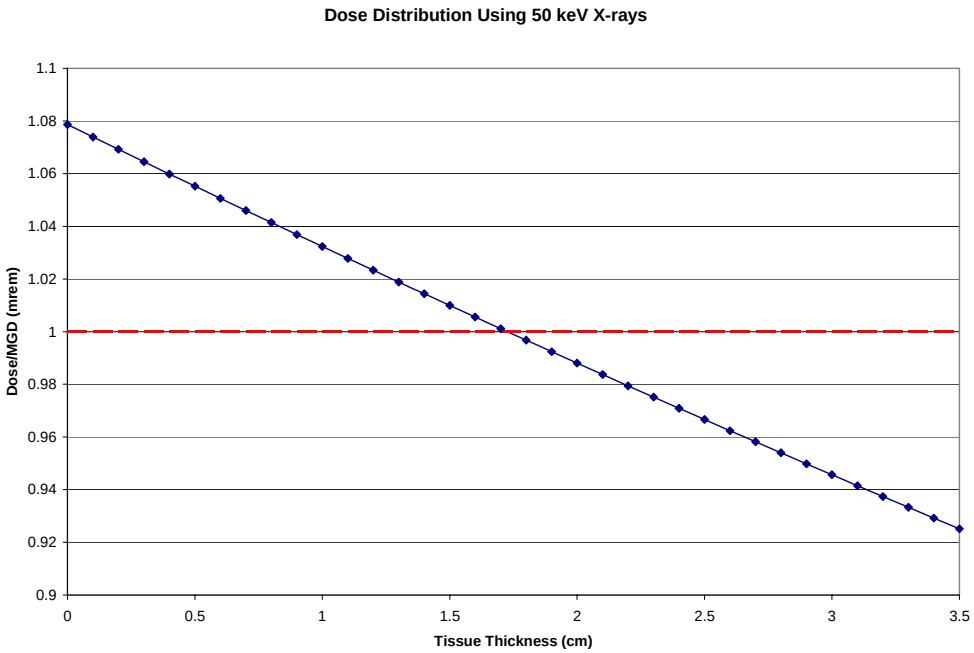

FIGURE 11.14: 50 keV dose distribution

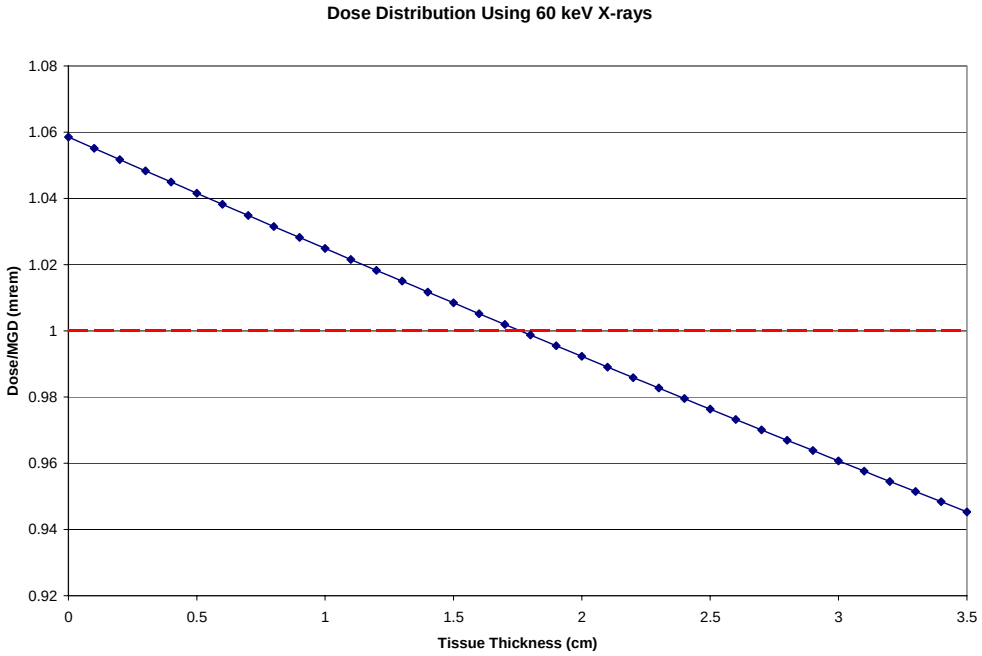

FIGURE 11.15: 60 keV dose distribution

Using the dosimetry data obtained at each energy, the flux used for acquiring each radiograph and component of an MIR sets was calculated and is presented in Figure 11.16.

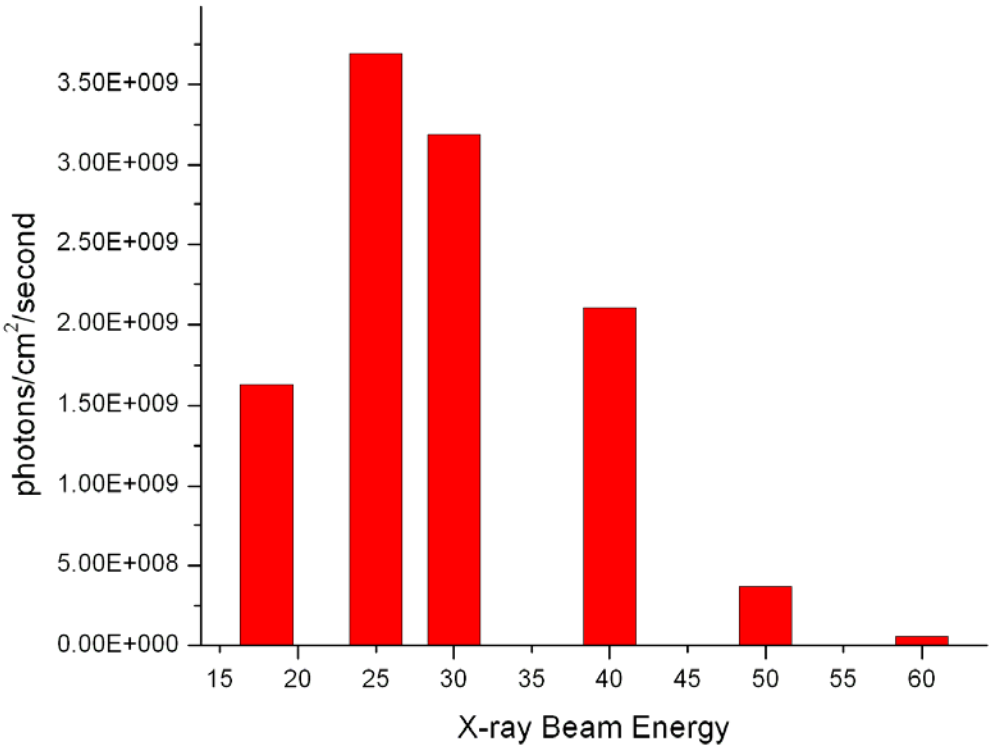

FIGURE 11.16: Photon flux vs. energy used for MIR

11.4 Discussion

The primary purpose of the study is to demonstrate the how breast imaging using MIR performs across a wide range of energies. MIR is a relatively new imaging method, and the physics associated with using MIR for soft tissue imaging can be confusing for those not familiar with analyzer based imaging. If considering absorption alone, one would expect contrast in soft tissue to fall off dramatically with an increase in energy, with little absorption contrast at energies at or above 40 keV. The synchrotron radiographs at each energy illustrate the reduction in contrast, especially at 60 keV where there is essentially zero absorption contrast in soft tissue.

Translating MIR from a synchrotron to even a non-synchrotron based laboratory system is a challenging endeavor, given the demands of flux, stability, and beam geometry. Image acquisition times based conventional x-ray tubes using molybdenum sources can be as high as 10,000 seconds, well beyond the time window needed for clinical imaging (Pisano et al. 2000) Molybdenum x-ray tubes have a stationary anode that limits heat dissipation and places significant engineering limitations on the flux that can be generated per unit time. Tungsten x-ray tubes have large, rotating anodes and can tolerate much higher voltages and amperages. While tungsten x-ray tubes offer many advantages in flux and heat dissipation, the characteristic x-rays generated by tungsten are too high to generate absorption contrast in soft tissue. However, this study has demonstrated that the MIR specific contrast mechanisms of refraction and scatter can generate excellent soft tissue contrast without the need for x-ray absorption.

The reduction of photons at higher energies is evident in the dose distribution curves, where there is marked difference between the distributions at 18 keV and 60 keV. At 18 keV, there is a large drop in flux due to absorption in the tissue. This drop in flux is reduced with increasing energy, with the highest transmission of photons occurring at 50 keV and 60 keV. A decrease in absorption translates to an increase in efficiency, which is evident in the flux measurements presented in Figure 11.16.

11.5 Conclusion

The results of the study indicate breast imaging using MIR is considerably different than conventional mammography and should be assessed accordingly. The ability to use refraction and scatter in addition to absorption extends the range of energies that can be utilized for MIR. Use of low energy x-rays has been an unavoidable requirement for generating x-ray

contrast in conventional mammography, but this may not be the case for MIR. The ability to visualize diagnostically useful features in breast tissue at higher beam energies dramatically reduces the absorbed dose to the patient and improves the overall efficiency of both synchrotron and potential non-synchrotron based MIR.

A major discovery in this study is the ability to use 60 keV x-rays for soft tissue imaging with an ultra-low surface dose. The combination of higher x-ray energies and lower required photon flux makes the development of a non-synchrotron based, and eventually clinical, DEI system far more realistic.

Chapter 12: Analysis of Breast Cancer Contrast Mechanisms using Multiple Image Radiography

12.1 Introduction

Application of the Diffraction Enhanced Imaging (DEI) technique to breast imaging has been shown to generate considerable gains in contrast when compared to conventional mammography. DEI is an imaging technique that can generate image contrast from an object's x-ray absorption, as with conventional radiography, and also from the refraction of x-rays through an object. A new image processing method called Multiple Image Radiography (MIR) has been developed to address many of the errors inherent to the initial DEI processing method and adds an additional method of image contrast, ultra-small angle scatter. Currently both DEI and MIR images can only be obtained using a synchrotron as an x-ray source, but efforts are underway to develop a non-synchrotron based DEI/MIR laboratory system that would be the next step towards a clinical prototype. An area where MIR could make a dramatic impact is in breast imaging, where x-rays are currently used to image weakly absorbing structures such as small masses and spiculations.

Previous studies using the DEI method to analyze the underlying contrast mechanisms in breast cancer fibrils demonstrated that x-ray extinction plays a large role in image contrast. Extinction is term used to describe scattering events that occur within an object that deflect the path of an x-ray enough to cause it to be rejected by the analyzer crystal. Studies of breast cancer spiculations by Hasnah et al. have demonstrated an 8 to 33 fold increase in the DEI peak image when compared to a corresponding radiograph.

The advent of MIR allows for a more complete and rigorous assessment of these properties through the addition of an image representing an object's ultra-small angle scatter.

12.2 Materials and Methods

Three breast cancer specimens were selected for imaging at the X-15A beamline, National Synchrotron Light Source, Brookhaven National Laboratory (Upton, NY) after receiving Institutional Review Board approval. All MIR image sets and synchrotron radiographs were acquired using the X-15A beamline at the National Synchrotron Light Source, Brookhaven National Laboratory (Upton, NY). A Photonic Science VHR-150 x-ray camera (Robersbridge, East Sussex, UK) was used for image acquisition, with a FOV of 120mm x 80mm and a 30 micron pixel size.

In order to calibrate the fitting algorithm, multiple nylon monofilament fibers and Lucite rods of known diameter and index of refraction were selected for analysis. The smaller nylon fibers were selected to approximate the diameter and geometry of the breast cancer spiculations. Each specimen and corresponding synchrotron radiograph were acquired using a 40 keV x-ray beam energy and a 350 mrad surface dose. For MIR an angular distribution of ± 4 microradians was selected with a theta increment of 0.4 microradians, producing 21 images. These images were processed using the MIR method to generate images representing the contrast generated from x-ray absorption, refraction, and scatter.

Extracting three dimensional information from a two dimensional image presents a significant challenge, especially for non-uniform objects. Breast cancer speculations are cylindrical in nature, which allows for approximations to be made regarding their material properties. In order to extract information about breast cancer speculations, it is first necessary to design and calibrate an analysis method. An MIR based analysis method

developed in collaboration with Jovan Brankov, Ph.D., Illinois Institute of Technology, Chicago, IL, was used to determine the diameter and index of refraction of both nylon and Lucite fibers and breast cancer spiculations. With these two critical properties, many other aspects of the fibers and spiculations can be analyzed and modeled. While there are three contrast components present in an MIR image, the refraction image will most likely be the most important for a clinical imaging system. If higher energy x-rays are utilized for imaging, then the absorption image will be poor when compared to the refraction image. With a major reduction in flux at the tails of the rocking curve, the scatter image will also lay a secondary role to the refraction image. Calculating and comparing the index of refraction across multiple breast cancer specimens will provide some level of assurance that the material properties generating refraction contrast is consistent and not an anomaly.

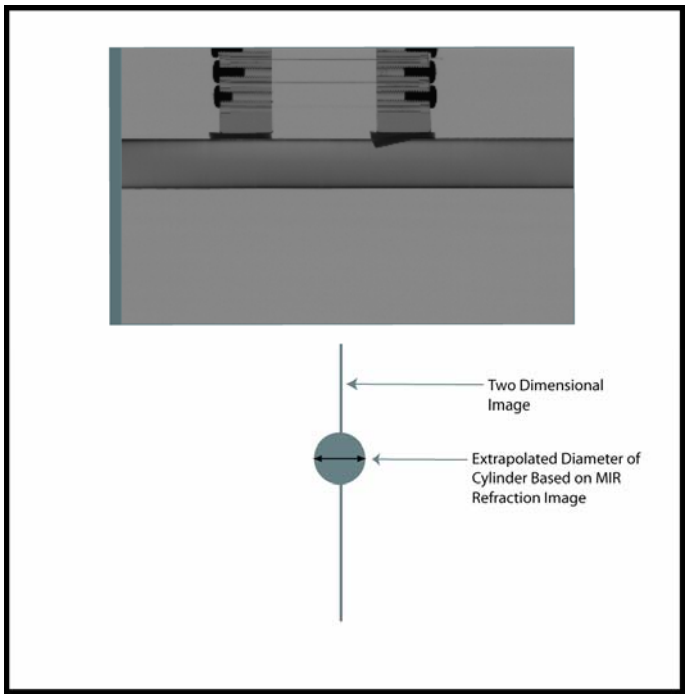

FIGURE 12.1 Estimation of fiber diameter using MIR

Calibration of the method was performed using nylon and Lucite fibers of varying diameter. Nylon fibers with diameters of 200 microns, 360 microns, and 560 microns were

imaged using MIR at 40 keV with a sampling range of -4 to 4 microradians and theta increment of 0.4 microradians. These fibrils were selected to approximate the geometry and diameter of clinically significant speculations. Larger Lucite rods with diameters of 13,000 microns and 19,000 microns were selected to assess the algorithm for larger diameter objects. Figure 12.2 and 12.3 demonstrate the identification and selection of each fiber or fibril.

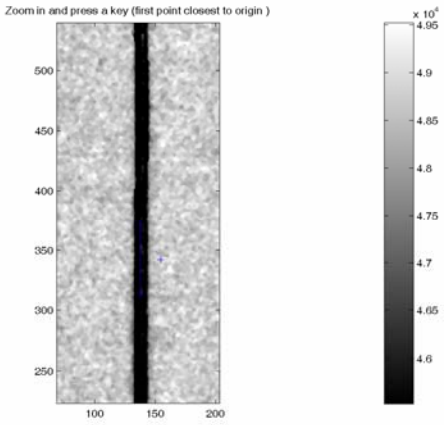

FIGURE 12.2: Selection of fiber with relation to background

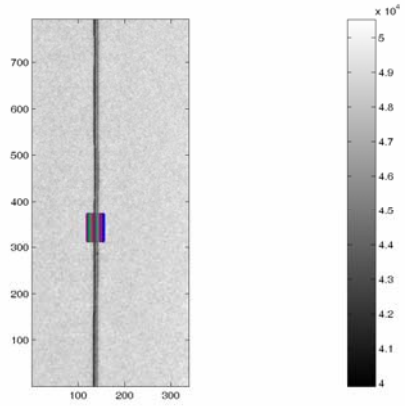

FIGURE 12.3: Selection of fiber and background region

Cylindrical objects such as nylon fibers and breast cancer speculations exhibit a characteristic refraction profile as illustrated in Figure 12.4. Refraction will be the highest at

the edges of the rod, and zero in the middle. If the object is assumed to be cylindrical, then one can use the refraction signature from an MIR or DEI refraction image to extrapolate the diameter. With a cylinder of known diameter, the index of refraction of the fiber or fibril can be extrapolated.

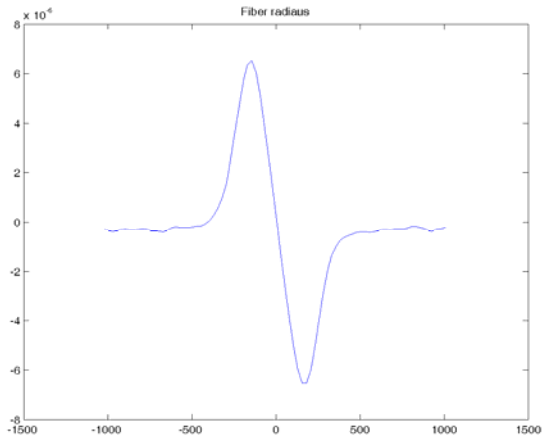

FIGURE 12.4: Nylon fiber refraction profile

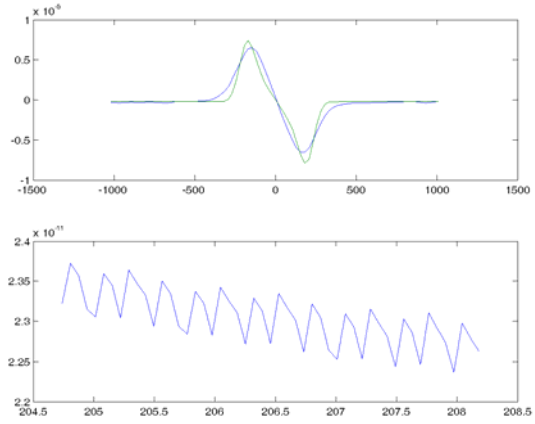

FIGURE 12.5: Fitting of simulated cylinder to nylon fiber

12.3 Results

The nylon and Lucite diameter and index of refraction information is presented in Table 12.1 and 12.2.

Material	Energy	Measured Diameter (microns)	Calculated Diameter (microns)	Percent Error
Nylon	40	200	208.96	4.48%
Nylon	40	360	387.36	7.60%
Nylon	40	560	617.90	10.30%
Lucite	40	13000	14210	9.31%
Lucite	40	19000	20938	10.20%

TABLE 12.1: MIR diameter calibration

Material	Energy (keV)	Diameter (microns)	Density (g/cm^3)	Refractive Index	Calculated Refractive Index	Percent Error
Nylon	40	200	1.14	$1.49x10^{-7}$	$2.16x10^{-7}$	37.3%
Nylon	40	360	1.14	$1.49x10^{-7}$	$1.89x10^{-7}$	26.8%
Nylon	40	560	1.14	$1.49x10^{-7}$	1.77x10-7	18.9%
Lucite	40	13000	1.19	$1.42x10^{-7}$	$2.01x10^{-7}$	41.5%
Lucite	40	19000	1.19	$1.42x10^{-7}$	$2.00x10^{-7}$	39.9%

TABLE 12.2: MIR index of refraction calibration

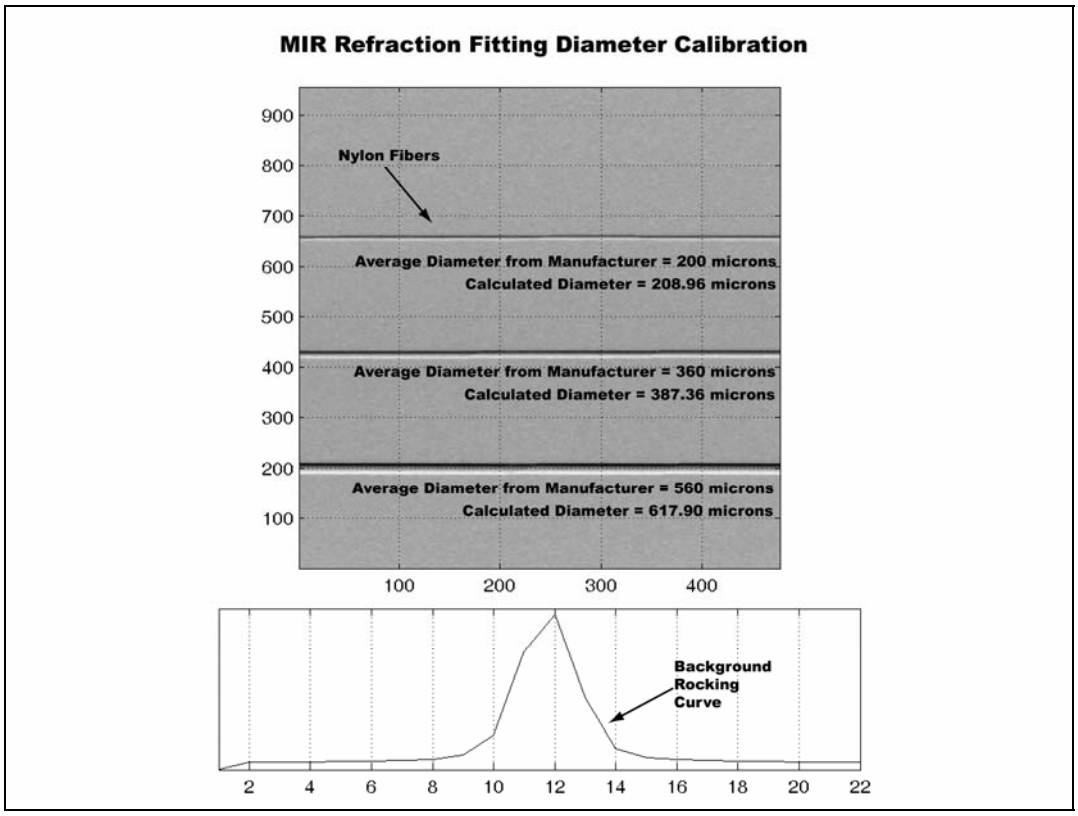

FIGURE 12.6: Nylon fiber fitting calibration values

The same method used for extracting the diameter and index of refraction for the nylon and Lucite fibers was applied to 5 regions of interest in three separate breast cancer specimens. MIR refraction images of the breast cancer specimens used are presented in Figures 12.7-12.9, and the calculated spiculation diameter and index of refraction presented in Table 12.3.

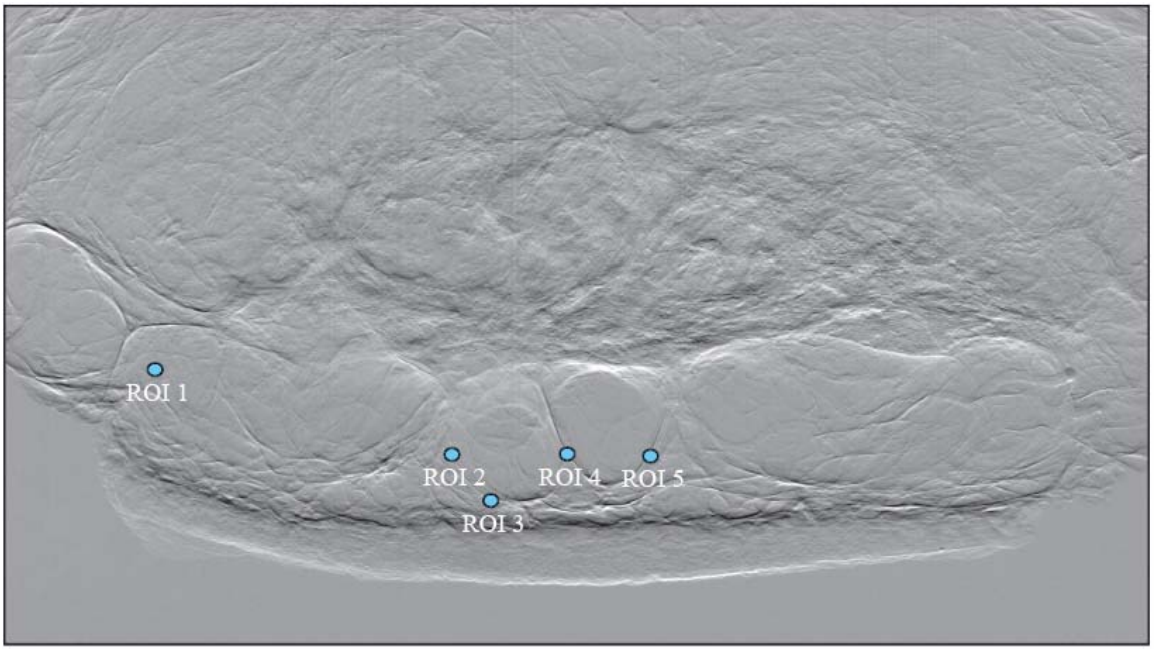

FIGURE 12.7: Breast cancer specimen with spiculations 1-5

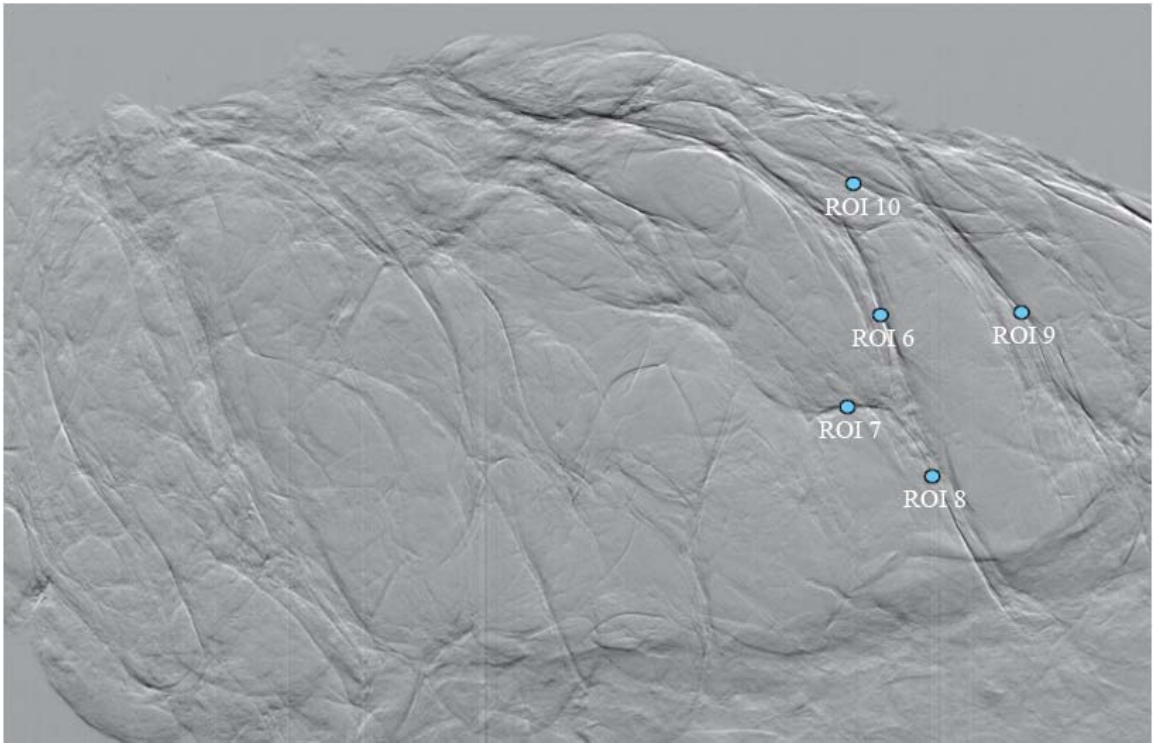

FIGURE 12.8: Breast cancer specimen with spiculations 6-10

FIBRIL 12.9: Breast cancer specimen with spiculations 11-15

ROI	Fibril Diameter (micrometers)	Index of Refraction
1	125.14	1.91×10^{-7}
2	152.1	1.16×10^{-7}
3	112.24	2.23×10^{-7}
4	106.32	1.72×10^{-7}
5	121.84	3.64×10^{-7}
6	253.44	1.75×10^{-7}
7	212.1	2.19×10^{-7}
8	95.96	1.48×10^{-7}
9	178.02	2.71×10^{-7}
10	148.9	2.50×10^{-7}
11	111.5	1.84×10^{-7}
12	91.18	2.00×10^{-7}
13	104.78	2.14×10^{-7}
14	205.82	5.22×10^{-8}
15	126.8	1.05×10^{-7}
		Average Index of Refraction = 1.92×10^{-7}
		Standard Deviation= 7.40×10^{-8}

TABLE 12.3: Fibril index of refraction

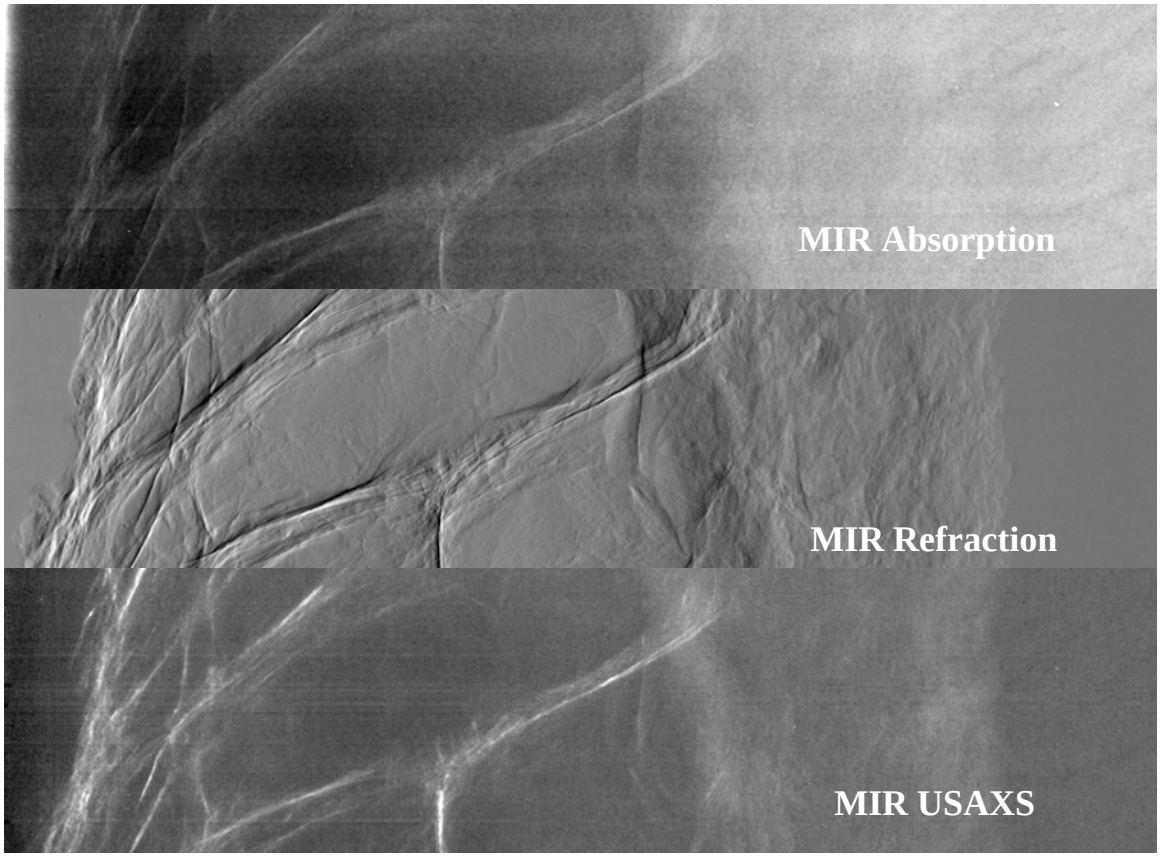

FIGURE 12.10: Fibril contrast components at 40 keV

An MIR set of a localized breast cancer mass and spiculation is presented in Figure 12.10.

12.4 Discussion

The underlying physics of x-ray refraction and scatter imaging is still in an early stage of investigation, especially when compared to the 100 plus year history of absorption based x-ray imaging. Given the inherent inhomogeneity of biological tissues, an analysis of the roughly cylindrical breast cancer spiculations provides a diagnostically useful feature than can be reliably compared with multiple tissue specimens.

The use of multiple standardized homogenous cylinders imaged in air allows for an accurate calibration of the refraction based fitting algorithm. Use of this algorithm for

analyzing biological tissues will introduce errors into the calculation due the non-homogenous nature of biological tissues, but the properties of breast tissue and the diagnostic application reduce the importance of these errors in the absolute calculation.

The fundamental problem with conventional mammography is the difficulty in visualizing low contrast objects immersed in highly absorbing background of adipose tissue. Neoplastic lesions increase in size and density with time, eventually becoming large and dense enough to rise above the background and become visible using conventional methods. Since breast cancer mortality is directly related to the size and progression of a lesion, reducing the time between the generation of a malignant lesion and detection is a goal of all new breast imaging modalities.

Multiple Image Radiography improves upon conventional radiography by utilizing the differences in multiple x-ray contrast mechanisms to help differentiate between benign and malignant structures. Adipose tissue may have an x-ray attenuation similar to a small malignant lesion, but they do not have the same refraction signatures. Adipose tissue has very little refraction and scatter contrast, but the small cylindrical speculations of a breast cancer lesion has a large refraction and scatter signatures. At 40 keV, absorption contrast in soft tissue is minimal, further increasing the overall contrast gradient between the lesion of interest and the background tissue.

Further gains in refraction contrast for spiculations come from their geometry, which is ideal for the refraction of x-rays. For a collimated x-ray beam incident on a cylindrical object, refraction contrast will be the greatest at the top and bottom of the cylinder, with minimal refraction contrast at the center. As the diameter of a cylinder decreases, refraction contrast will remain due to the geometry of the object even after the level of

absorption contrast fades into the background. The index of refraction values obtained across multiple breast cancer specimens indicates that the materials properties are similar, and the increase in contrast should be observed in most similar cancer specimens.

12.5 Conclusion

Determining the underlying contrast mechanisms providing enhanced visualization in breast tissue is a paramount step in designing a non-synchrotron based DEI/MIR system. This study demonstrates that the MIR specific contrast mechanisms of refraction and scatter play a major role in structural visualization, further reducing the dependence on x-ray absorption for lesion visualization. A reduction in x-ray absorption translates to a reduction in patient absorbed dose, which is of tremendous benefit when considering the relatively high dose required for conventional mammography.

The use of nylon in these experiments has indicated a potential use for future modeling and simulation experiments. With a similar geometry, diameter, and index of refraction, nylon monofilament provides insight into why these diagnostically important structures generate high contrast.

Chapter 13: Application of Data to the Development of a Clinical Diffraction Enhanced Imaging/Multiple Image Radiography System

13.1 Introduction

The information presented in this dissertation seeks to define the system parameters and performance specifications for both synchrotron based DEI and MIR breast imaging as well as define potential solutions for a non-synchrotron based prototype system. Primary engineering and physics considerations for system development have been dose, x-ray beam energy, and contrast components in breast tissue. These aspects are interdependent and must be elucidated to determine how the system will perform for the desired application of breast imaging. While there are many novel ways to generate x-rays, the most common and commercially available are x-ray tubes. Use of an x-ray tube for a DEI system is preferable given these considerations, but the heat generated by x-ray tubes and the angular divergence of the resulting x-ray beam place considerable restrictions on their use for DEI. Clinically useful breast images from 18 keV to 60 keV have been generated using a x-ray source, and these bounds represent the two primary commercially available x-ray targets, molybdenum and tungsten.

13.2 Estimated Flux Requirements

For medical imaging, acquisition time is key factor since any movement by the patient can degrade image quality. Imaging times based on 18 keV molybdenum based x-ray sources have been on the order of 10,000 seconds, which is far outside the time

window needed for mammography (Pisano et al. 2000). The photon efficiency increases with higher beam energies, requiring fewer incident photons on the sample or patient as demonstrated in Chapter 11. As an initial demonstration, imaging times and flux requirements using 18 keV and 59 keV x-rays will be calculated, simulating molybdenum and tungsten based x-ray sources. Several assumptions must be made in regards to the system configuration, such as the pixel size and the number of photons per pixel. Since these values can be scaled as needed, a pixel size of 100 microns with 1000 photons per pixel traversing 5 cm of tissue (water) will be used for this example.

The number of photons needed per 100 micron square pixel can be calculated by dividing the number of photons per pixel desired by the attenuation of the photons through the object, which in this case is 5 cm of water.

$$N_{18keV}^{Surface} = \frac{1000\,photons/\,pixel}{e^{-\mu_{tot}t}} = \frac{1000\,photons/\,pixel}{6.4\times10^{-3}} = 1.6\times10^{5}\ photons/100\,\mu msq\,pixel$$

$$N_{59keV}^{Surface} = \frac{1000\,photons/\,pixel}{e^{-\mu_{tot}t}} = \frac{1000\,photons/\,pixel}{0.35} = 2.9\times10^{3}\ photons/100\,\mu msq\,pixel$$

For an 18 keV x-ray source, approximately 1.6×10^{5} incident photons would be required for each 100 micron square pixel. The attenuation of 59 keV x-rays is much less than at 18 keV, which results in a reduced incident photon demand of 2.9×10^{3} photons per 100 micron square pixel.

13.3 Incident X-ray Flux into Solid Angle Using an Emission Line Source

The crystal optics used in a DEI system act as a highly selective angular filter, which will eliminate from the beam photons that do not have the proper wavelength or angular divergence. For an x-ray tube based source, photons will radiate more-or-less into all

solid angles. In order to determine the flux requirement, one must calculate the flux based on the solid angle subtended by the detector and the x-ray crystal optics. Any x-ray tube is going to have a polychromatic energy distribution, and the crystal system will select one of the emission lines as defined by Bragg's law.

With a perfect crystal, the peak reflectivity for a given reflection will be very close to unity, making the integrated reflectivity close to the intrinsic reflection width in the Bragg-normal direction, or Darwin width. Assuming a silicon crystal with a Bragg [333] reflection, the Darwin width of 18 keV and 59 keV are:

$$18keV\ Si(333)DarwinWidth=2.9\times10^{-6}\,radians$$
$$59.3keV\ Si(333)DarwinWidth=0.83\times10^{-6}\,radians.$$

X-rays traveling in a direction parallel to the crystal lattice planes are known as Bragg-parallel, and the angular acceptance in the Bragg-parallel direction is not set by the crystal, but rather the detector resolution. If the object to be imaged is 1 meter from the x-ray source and a 100 micron spatial resolution is required, then the Bragg-parallel acceptance angle is 100 microradians. For a 100 microradian Bragg-parallel acceptance angle, the number of photons required per steradian at 18 keV and 59 keV are:

$$N_{18keV}^{\text{Required}}=\frac{1.6\times10^{5}\ photons/pixel}{2.9\times10^{-6}\,radians\times100\times10^{-6}\,radians/pixel}=0.55\times10^{15}\ photons/steradian$$
$$N_{59keV}^{\text{Required}}=\frac{2.9\times10^{3}\ photons/pixel}{0.83\times10^{-6}\,radians\times100\times10^{-6}\,radians/pixel}=3.5\times10^{13}\ photons/steradian.$$

13.4 X-ray Tube Flux

X-ray tube based sources have two components to their x-ray spectrum, characteristic emission lines and bremsstrahlung. The crystal optics of a DEI system allow for the

selection of only one energy, which makes the emission lines a logical choice for selection. In this case, the $K_{\alpha 1}$ of molybdenum (17.478 keV) and the $K_{\alpha 1}$ of tungsten (59.319 keV) will be used to determine the flux of these emission lines from each source.

Monte Carlo simulations of molybdenum and tungsten x-ray tubes at multiple voltage and current settings were generated to determined the flux that could be generated under realistic imaging conditions (Hableb et al. 1991). For a molybdenum target using a 75 kV accelerating voltage with 10 kW of power, the flux emitted into the $K_{\alpha 1}$ is:

$$n_{MoK_{\alpha 1}}^{Source} = 1.7 \times 10^{14}\ photons / steradian / \sec.$$

The $K_{\alpha 1}$ emission using tungsten target with a 150 kV accelerating voltage and 50 kW of power is:

$$n_{WK_{\alpha 1}}^{Source} = 1.56 \times 10^{14}\ photons / steradian / \sec.$$

The accelerating voltages were selected to maximize flux at a power setting that allowed for continuous operation. Higher accelerating voltages and power settings may be possible, but use of these higher settings for an extended period of time could melt the anode and destroy the tube. These tube settings represent a realistic flux output given current x-ray tube technology.

13.5 Estimated Image Acquisition Time

The optimal sampling procedures for clinical DEI and MIR have not yet been elucidated, which makes an exact estimation of the imaging time difficult to estimate. Both DEI and MIR could potentially be utilized with less dose and fewer images than used in this document. Based on experience, a single image on the analyzer crystal

rocking curve is sufficient to generate a useful image. If the analyzer is detuned to a value (80%) from the peak position, one can acquire one exposure containing refraction contrast and some extinction contrast. These calculations assume that there is a single monochromator crystal and analyzer system. The geometry of this simulation of consistent with that used at the National Synchrotron Light Source, using a line source x-ray in which the object is scanned through the beam. For an object 10 cm in height and a 100 micron pixel size (0.1 mm), 1000 scan lines will be required.

$$T(\sec) = \frac{N_{Energy}^{\text{Required}}(photons/steradian)}{n_{Energy}^{Source}(photons/steradian/\sec)} / 0.8(\text{detune losses}) \times 1(\text{DEI images}) \times 1000(\text{scan lines})$$

For the 75kV, 10kW, molybdenum target case (approximately 18keV):

$$T = \frac{0.55 \times 10^{15}\ photons/steradian}{1.7 \times 10^{14}\ photons/steradian/\sec} \times 1250 = 0.8 \times 10^{4}\ \sec = 2.2hr$$

For the 150kV, 50kW, tungsten target case (approximately 59.3 keV):

$$T = \frac{3.5 \times 10^{13}\ photons/steradian}{1.56 \times 10^{14}\ photons/steradian/\sec} \times 1250 = 0.28 \times 10^{3}\ \sec = 4.6\min$$

For a single image at a point on the rocking curve with 80% of maximum reflectivity, the time required using a molybdenum target using the above parameters is 2.2 hours. The time required using the same reflectivity for a tungsten tube is approximately 4.6 minutes. While this time is still greater than what would be expected for a clinical prototype, it is much closer to the desired goal. Using the same configuration, the imaging time could be further decreased by imaging variables such as the photons needed per pixel.

13.6 Application of Research to a Non-Synchrotron Based Prototype DEI System

The optics required for a non-synchrotron based system are the same as those required for a synchrotron based system. Advancements made in the thermal stabilization of the crystals to minimize or eliminate analyzer drift will be critical for any DEI system. The heat generated by a polychromatic x-ray source on the first crystal on the monochromator will mostly likely be less using a conventional x-ray source than a synchrotron given the reduced overall flux and energy range, but one should expect similar trends to those observed at the NSLS.

There are multiple methods currently employed to generate image sets that are considered to be DEI or DEI based. The simplest method of generating a DEI image is to simply acquire a single image at a given rocking curve position, which is demonstrated in the parameter study described in Chapter 10. Image pairs can be acquired to generate apparent absorption and refraction images, or multiple images across the rocking curve can be obtained to generate MIR absorption, refraction, and scatter images. The clinical utility and benefit of each method is still under investigation, but experience has shown that images acquired on the slope of the rocking curve generate images similar to those obtained using other processing methods. Given the current flux limitations and concern about overall imaging time, single image DEI is a logical method at this stage of development.

Chapter 11 demonstrates that higher energies can be utilized for soft tissue imaging, which increases photon efficiency and decreases the flux needed for imaging. If x-ray refraction and ultra-small angle scatter is shown to provide clinically useful information,

then one can expect clinically useful images to be generated using a conventional x-ray tube with a tungsten target.

The generation of 60 keV MIR refraction images with a 4 mrad surface dose was a discovery that demonstrated experimentally that the flux from a commercially available tungsten x-ray tube could be used for a mammography based system. Imaging times based on a 100 micron pixel size,1000 photons delivered to each pixel, using 80% crystal reflectivity yields imaging times of approximately 4 minutes. This is higher than what one would desire for a clinical system, but this time can be reduced dramatically if the number of photons per pixel can be decreased. Novel high flux x-ray systems are currently under development for potential applications for DEI and applications currently performed at synchrotrons, many of which could serve as a source for a DEI clinical prototype. Flux and divergence will always be critical factors for DEI since they are inherent to the optics and detection systems, and the calculations made in Chapter 13 can be used in the initial consideration of other x-ray sources.

With the technology currently available, this dissertation provides a realistic system design for a clinical prototype DEI mammography system.

BIBLIOGRAPHY

Arpino, G, Bardou, V, Clark, G, and Elledge, R. "Infiltrating lobular carcinoma of the breast: tumor characteristics and clinical outcome." *Breast Cancer Research* 6.3 (2004): 149-56.

Astley, S.M, and Gilbert, F.J. "Computer-aided detection in mammography." *Clinical Radiology* 59 (2004): 390-99.

Bartow, S. "The Breast." Pathology. Eds. Emanual Rubin and John Farber. 3rd ed. Philadelphia: Lippincott-Raven, 1999. 1029-47.

Beckman, C. Obstetrics and Gynecology. 3rd ed. Philadelphia: Lippincott, Williams, and Wilkins, 1998.

Breast Imaging-Reporting and Data System 2006. American College of Radiology. Available: http://www.acr.org/s_acr/bin.asp?CID=883&DID=14553&DOC=FILE.PDF. 3/16 2006.

Brem, R, Schoonjans, J, and Hoffmeister, J. "Evaluations of breast cancer with a computer-aided detection system by mammographic appearance, histology, and lesion size." *Radiology* 217 (2000): 400.

Burhenne, L, Wood, S, and D'Orsi, C. "The potential contribution of computer-aided detection to the sensitivity of screening mammography." *Radiology* 215 (2000): 554-62.

Burstein, H, Polyak, K, Wong, J, Lester, S, and Kaelin, C. "Ductal Carcinoma in Situ of the Breast." *New England Journal of Medicine* 350 (2004): 1430-41.

Bushberg, J, Seibert, A, Leidholdt, M, and Boone, J. The Essential Physics of Medical Imaging. 2nd ed. Philadelphia: Lippincott Williams and Wilkins, 2002.

Castellino, R. "Computer-Aided Detection in Oncologic Imaging: Screening Mammography as a Case Study." *The Cancer Journal* 8.2 (2002): 93-99.

Chapman, D, Pisano, E, Thomlinson, W, Zhong, Z, Johnson, R, Washburn, D, Sayers, D, and Malinowska, K. "Medical Applications of Diffraction Enhanced Imaging." *Breast Disease* 10.3,4 (1998): 197-207.

Chapman, D, Thomlinson, W, Johnson, R, Washburn, D, Pisano, E, Gmur, N, Zhong, Z, Menk, R , Arfelli, F, and Sayers, D. "Diffraction enhanced x-ray imaging." *Physics in Medicine and Biology* 42 (1997): 2015-25.

Chevarley, F, and White, E. "Recent trends in breast cancer mortality among white and black US women." *American Journal of Public Health* 87 (1997): 775.

Christian, P. "Fundamentals of Molecular Imaging with PET." Nuclear Medicine and PET. Eds. Paul E Christian, Donald R Bernier and James K Langan. 5th ed. St. Louis: Mosby, 2004. 618.

Damiana, S, and Eusebi, V. "Gross and Microscopic Pathology." Cancer of the Breast. Eds. William Donnegan and John Spratt. 5th ed. Philadelphia: Saunders, 2002. 347-70.

de Koning, H. "Mammographic screening: evidence from randomized controlled trials." *Annals of Oncology* 14 (2003): 1185-89.

Dilmanian, F, Zhong, Z, Ren, B, Wu, X, Chapman, D, Orion, I, and Thomlinson, W. "Computed tomography of x-ray index of refraction using the diffraction enhanced imaging method." *Physics in Medicine and Biology* 45 (2000): 933-46.

Doi, K, Giger, M, MacMahon, H, Hoffmann, K, Nishikawa, R, Schmidt, R, Chua, K, and Katsuragawa, S. "Computer-Aided Diagnosis: Development of Automated Schemes for Quantitative Analysis of Radiographic Images." *Seminars in Ultrasound, CT, and MRI* 13.2 (1992): 140-52.

Donegan, W. "Gross and Microscopic Pathology." Cancer of the Breast. Eds. William Donegan and John Spratt. 5th ed. Philadelphia: Saunders, 2002. 358-70.

Feig, S, and Yaffe, M. "Current Status of Digital Mammography." *Seminars in Ultrasound, CT, and MRI* 17.5 (1996): 424-43.

Fiedler, S, Bravin, A, Keyrilainen, J, Fernandez, M, Suortti, P, Thomlinson, W, Tenhunen, M, Virkkunen, P, and Karjalainen-Lindsberg, M. "Imaging lobular breast carcinoma: comparison of synchrotron radiation DEI-CT technique with clinical CT, mammography and histology." *Physics in Medicine and Biology* 49.2 (2004): 175-88.

Freedman, D, Petitti, D, and Robins, J. "On the efficacy of screening for breast cancer." *International Journal of Epidemiology* 33 (2004): 43-55.

Galt, J, and Faber, T. "Principles of Single Photon Emission Computed Tomography (SPECT) Imaging." Nuclear Medicine and PET. Eds. Paul E Christian, Donald R Bernier and James K Langan. 5th ed. St. Louis: Mosby, 2004. 618.

Gold, R. "The Evolution of Mammography." *Radiologic Clinics of North America* 30.1 (1992): 1-19.

Green, B, and Taplin, S. "Breast Cancer Screening Controversies." *JABFP* 16.3 (2003).

Grosch, D, and Hopwood, L. Biological Effects of Radiations. 2nd ed. New York: Academic Press, 1979.

Hableb, J, Kensek, P, Mehlhorn, T, Valdez, G, Seltzer, S, and Berger, M. ITS Version 3.0: The integrated TIGER Series of Coupled Electron/Photon Monte Carlo Transport Codes. Computer software. Sandia National Laboratories, 1991.

Hall, E. Radiobiology for the Radiologist. 2nd ed. Hagerstown: Harper and Row, 1978.

Hasnah, M., Zhong, Z, Oltulu, O, Pisano, E, Johnson, R, Sayers, D, Thomlinson, W, and Chapman, D. "Diffraction enhanced imaging contrast mechanisms in breast cancer specimens." *Medical Physics* 29.10 (2002): 2216-21.

Haus, A. "Technologic Improvements in Screen-Film Mammography." *Radiology* 174.3 (1990): 628-37.

Hendee, W. "History and Status of X-ray Mammography." *Health Physics* 69.5 (1995).

Hendee, W, and Ritenour, R. Medical Imaging Physics. 4th ed. New York: Wiley-Liss, 2002.

Hwang, E, Nyante, S, Chen, Y, Moore, D, DeVries, S, Korkola, James, Esserman, L, and Waldman, F. "Clonality of Lobular Carcinoma in Situ and Synchronous Invasive Lobular Carcinoma." *CANCER* 100.12 (2004): 2562-72.

Jamal, A, Murray, T, Samuels, A, Ghafoor, A, Ward, E, and Thun, M. "Cancer Statistics, 2003." *CA: A Cancer Journal for Clinicians* 53 (2003): 5-26.

Kelsey, J, Fischer, D, and Holford, T. "Exogenous estrogens and other factors in the epidemiology of breast cancer." *Journal of the National Cancer Institute* 67 (1981): 327.

Kerlikowske, K, Smith-Bindman, R, Ljung, B, and Grady, D. "Evaluation of Abnormal Mammography Results and Palpable Breast Abnormalities." *Annals of Internal Medicine* 139.4 (2003): 274-85.

Keryiläinen, J, Fernández, M, Fiedler, S, Bravin, A, Karjalainen-Lindsberg, M, Virkkunen, P, Elo, E, Tenhunen, M, Suortti, P, and Thomlinson, W. "Visualization of calcifications and thin collagen strands in human breast tumour specimens by the diffraction-enhanced imaging technique: a comparison with conventional mammography and histology." *European Journal of Radiology* 53 (2005): 226-37.

Kiss, M, Sayers, D, and Zhong, Z. "Measurement of image contrast using diffraction enhanced imaging." *Physics in Medicine and Biology* 48 (2003): 325-40.

Lacquement, M, Mitchell, D, and Hollingsworth, A. "Positive Predictive Value of the Breast Imaging Reporting and Data System." *Journal of the American College of Surgeons* 189.1 (1999): 34-40.

Li, J, Zhong, Z, Lidtke, R, Kuettner, K, Peterfy, C, Aliyeva, E, and Muehleman, C. "Radiography of soft tissue of the foot and ankle with diffraction enhanced imaging." *Journal of the American Podiatric Medical Association* 94.3 (2004): 315-22.

Mandelblatt, J, Schechter, C, Yabroff, R, Lawrence, W, Dignam, J, Muennig, P, Chavez, Y, Cullen, J, and Fahs, M. "Benefits and Costs of Interventions to Improve Breast Cancer Outcomes in African American Women." *Journal of Clinical Oncology* 22.13 (2004): 2554-64.

Moore, K. Clinically Oriented Anatomy. 3rd ed. Baltimore: Williams and Wilkins, 1992.

Muehleman, C, Majumdar, S, Issever, A, Arfelli, F, Menk, R, Rigon, L, Heitner, G, Reimes, B, Metge, J, Wagner, A, Kuettner, K, and Mollenhauer, J. "X-ray detection of structural orientation in human articular cartilage." *Osteoarthritis and Cartilage* 12 (2004): 97-105.

Oltulu, O, Zhong, Z, Moumen, H, Wernick, M, and Chapman, D. "Extraction of extinction, refraction, and absorption properties in diffraction enhanced imaging." *Journal of Physics D: Applied Physics* 36 (2003): 2152-56.

Pike, M, Spicer, D, Dahmoush, L, and Press, M. "Estrogens, progestins, normal breast cell proliferation and breast cancer risk." *Epidemiological Review* 15 (1993): 17.

Pisano, E, Johnson, R, Chapman, D, Geradts, J, Iacocca, M, Livasy, C, Washburn, D, Sayers, D, Zhong, Z, Kiss, M, and Thomlinson, W. "Human Breast Cancer Specimens: Diffraction Enhanced Imaging with Histologic Correlation-Improved Conspicuity of Lesion Detail Compared to Digital Radiography." *Radiology* 214 (2000): 895-901.

Qian, W, Li, L, Clarke, L, Clark, R, and Thomas, J. "Digital Mammography: Comparison of Adaptive and Noadaptive CAD Methods for Mass Detection." *Academic Radiology* 6 (1999): 471-80.

Sanger, J, and Kramer, E. "Practical Clinical SPECT- A Personal View." Clinical SPECT Imaging. Eds. Elissa A Kramer and Joseph J Sanger. New York: Raven Press, 1995. 259.

Tabar, L, Smith, R, Vitak, B, Yen, M, Chen, T, Warwick, J, Myles, J, and Duffy, S. "Mammographic Screening: A Key Factor in the Control of Breast Cancer." *The Cancer Journal* 9.1 (2003): 15-27.

Wernick, M, Wirjadi, O, Chapman, D, Zhong, Z, Galatsanos, N, Yang, Y, Brankov, J, Oltulu, O, Anastasio, M, and Muehleman, C. "Multiple-image radiography." *Physics in Medicine and Biology* 48 (2003): 3875-95.

Whalen, J, and Balter, S. Radiation Risks in Medical Imaging. Chicago: Year Book Medical, 1984.

Wild, L, and Neil, D. "The use of high frequency ultrasonic waves for detecting changes of texture in the living tissue." *Lancet* 1 (1951): 655-57.

Zhong, Z, Thomlinson, W, Chapman, D, and Sayers, D. "Implementation of diffraction-enhanced imaging experiments: at the NSLS and APS." *Nucl. Instrum. Methods Phys. Res. A* 450 (2000): 556-67.

Zwiebel, W, and Sohaey, R. Introduction to Ultrasound. Philadelphia: W.B. Saunders Company, 1998.